

NASA Technical Memorandum 78137

(NASA-TM-78137) SPACE PROCESSING
APPLICATIONS ROCKET PROJECT SPAR III Final
Report (NASA) 167 p HC A03/MF A01 CSCL 22

N78-21189

Unclass

63/15

12422

**Space Processing
Applications Rocket Project
SPAR III - Final Report**

JANUARY 1978

NASA



NASA Technical Memorandum 78137

**Space Processing
Applications Rocket Project
SPAR III - Final Report**

**George C. Marshall Space Flight Center
Marshall Space Flight Center, Alabama**



**National Aeronautics
and Space Administration**

**Scientific and Technical
Information Office**

1978

**SPACE
PROCESSING
APPLICATIONS
ROCKET**



TABLE OF CONTENTS

Chapter	Page
INTRODUCTION	iii
I. SPAR III ENGINEERING REPORT	I-1
II. SCIENCE PAYLOAD III TEST REPORT	II-1
III. LIQUID MIXING (Experiment 74-18)	III-1
IV. INTERACTION OF BUBBLES WITH SOLIDIFICATION INTERFACES (Experiment 74-36)	IV-1
V. EPITAXIAL GROWTH OF SINGLE CRYSTAL FILM (Experiment 74-45)	V-1
VI. CONTAINERLESS PROCESSING OF BERYLLIUM (Experiment 74-48)	VI-1
VII. CONTACT AND COALESCENCE OF VISCOUS BODIES (Experiment 74-53)	VII-1

SPACE PROCESSING APPLICATIONS ROCKET PROJECT

SPAR III

FINAL REPORT

INTRODUCTION

Space processing has been defined as "using the unique aspects of space environment to process materials." As such, it is an area of technology endemic in origin and function to the Space Age. Historically, it is a direct descendent of the experiments and science demonstrations of Skylabs III and IV, as well as the experiments performed during the Apollo-Soyuz Test Project (ASTP) mission. Space processing, in a generic sense, is an effort designed to take advantage of the above-mentioned "unique aspects of space environment." Specifically, these aspects stem from the presence of a low-g environment during space flight and result in a reduction in detrimental effects such as thermal convection, sedimentation of heavy particles, and the buoyancy of bubbles and lower density particles in a fluid. The ultimate goal in taking advantage of these low-g characteristics is to provide products and processes which are beneficial to mankind.

The Space Processing Applications Rocket (SPAR) project consists of a series of research rocket flights designed to provide opportunity for materials processing experiments in a short-term low-g environment. The project currently uses a Black Brant VC (BBVC) sounding rocket as its vehicle, although a Nike-boosted configuration will be available in the event of heavier payloads. The BBVC rocket provides 15 min of flight, including approximately 5 min of low-g environment time usable for the most critical portions of materials processing experiments. The functions of the SPAR flights are to expand on the space processing-relevant data yielded by Skylab and ASTP, and to provide an experiment expertise and information base which will allow for greater sophistication of Shuttle/Spacelab materials processing activity.

Specifically, this report contains post-flight reports on the results of the experiments flown onboard SPAR III on December 14, 1976. These five experiments were devised by three industrial firms, one university, and one government agency, and coordinated by the Marshall Space Flight Center. Each experiment has been reported on by the respective Principal Investigator (PI), and

these reports are included in separate sections of this SPAR III report. Editing has been kept to the minimum necessary for uniformity in format. It is expected that this report will serve as a public record of SPAR activities, and it is hoped that it will provide information of significant interest to the materials processing community.

CHAPTER I

SPAR III ENGINEERING REPORT

By

J. H. Golmon

Marshall Space Flight Center

CONFIGURATION

The total rocket configuration is shown in Figure 1 and the SPAR III science payload is shown in Figure 2. Figure 3 shows the science payload with the location of temperature sensors.

PERFORMANCE

Trajectory parameters for the flight are shown in Figure 4. The low-g (10^{-4} or less) duration was approximately 255 s starting at 90 s and ending at 345 s. The science payload was shutoff at 660 s, but the telemetry stayed on for 967 s to attempt to record impact. However, loss of signal at 722 s precluded getting the shock loads and the TM shutdown signal.

The science payload battery specification is 28^{+15}_{-2} V. The battery voltage started at 37 V and dropped to 35 V at $t = 88$ s. Recovery back to 37 V occurred at 298 s.

INSTRUMENTATION — TELEMETRY

Temperatures

The temperatures inside the science payload are given in Figures 5 and 6. Use these two figures in conjunction with Figure 3 to locate these temperature sensors inside the payload. The temperature throughout most of payload III ranged between 20 to 25°C higher than on payload II. The two exceptions to this were in the aft end and the top end of the payload. The temperature in the aft end of payload III (on top of Experiment 74-45) ranged from 20 to 55°C higher than the temperatures in the aft end of payload II. The temperature in the top of the payload III was 25 to 30°C higher than it was in the top of payload II.

The reasons for these higher temperatures are:

1. The internal heat generation was greater on payload III than on payload II (for example Experiment 74-45).
2. Higher reentry heating was experienced on flight III (possibly due to a greater angle-of-attack).

The final conclusion is, however, that all critical components operated within their temperature limits.¹

Pressure

Pressure in the forward end of the science payload dropped from 13.26 psia at liftoff to 0.19 psia at $t = 87$ s. Payload III carried a 6-range pressure transducer in the lower part of the science payload. This transducer reading dropped to 0.4 psia at $t = 160$ s and stabilized until $t = 257$ s. This pressure increased to 0.4 psia at $t = 261$ s. It increased to 0.5 psia at $t = 286$ s and remained there through $t = 373$ s. At this point it began to increase sharply due to reentry into the Earth atmosphere.

EXPERIMENTS

Experiment 74-45, Epitaxial Growth of Single-Crystal Film

The furnace and its control system worked properly until the slider mechanism with the substrates was moved into contact with the growth solution. The temperature readings became erratic at that time, making it difficult to determine what the temperature was near the growth solution. Post-flight inspection showed that the slider mechanism was broken, either before or during the time the substrate was in contact with the solution. When the slider mechanism was withdrawn, it failed to remove the substrate from the growth solution.

Experiment 74-53, Contact and Coalescence of Viscous Bodies

This experiment did not form drops as planned. However, all the timer functions were performed satisfactorily and all subassemblies (camera operation, drop injector operation, acoustic field, etc.) operated within the experiment timeline. The failure of this experiment appears to be either the improper viscosity fluid or the improper needle size or possibly both. (It is difficult to correctly set these two parameters, since test results may not be reliable in a gravity environment.)

1. NASA/MSFC Memorandum EP44 (77-21).

Experiment 74-18/2 and 74-18/3, Liquid Mixing

This experiment performed as expected from an engineering standpoint.

Experiment 74-36/2, Interaction of Bubbles with Solidification Interfaces

The apparatus functioned well from an engineering standpoint.

Experiment 74-48, Containerless Processing of Beryllium

This experiment functioned properly for almost 3 min of low-g time. The required processing temperatures were attained, the sample was melted and resolidified while suspended in the electromagnetic field, the camera functioned properly, and the processed sample was returned intact. There was a broken water line in this experiment which was noted at the time of recovery. It is not clear when the water line broke. All of the 74-48 measurements became erratic at $t = 261.5$ s. The first irregularity preceding this time was a disturbance in the damping servo signal at $t = 249.2$ s. The servo oscillation damped out in the next 9 s. At this time, $t = 258.6$ s, there was a disturbance in all 74-48 measurements. Then 3 s later, $t = 261.5$, all measurements for this experiment became erratic for the rest of the flight, however, postflight analysis indicated that the experiment worked perfectly according to objectives. It levitated, melted, and solidified the sample as planned.

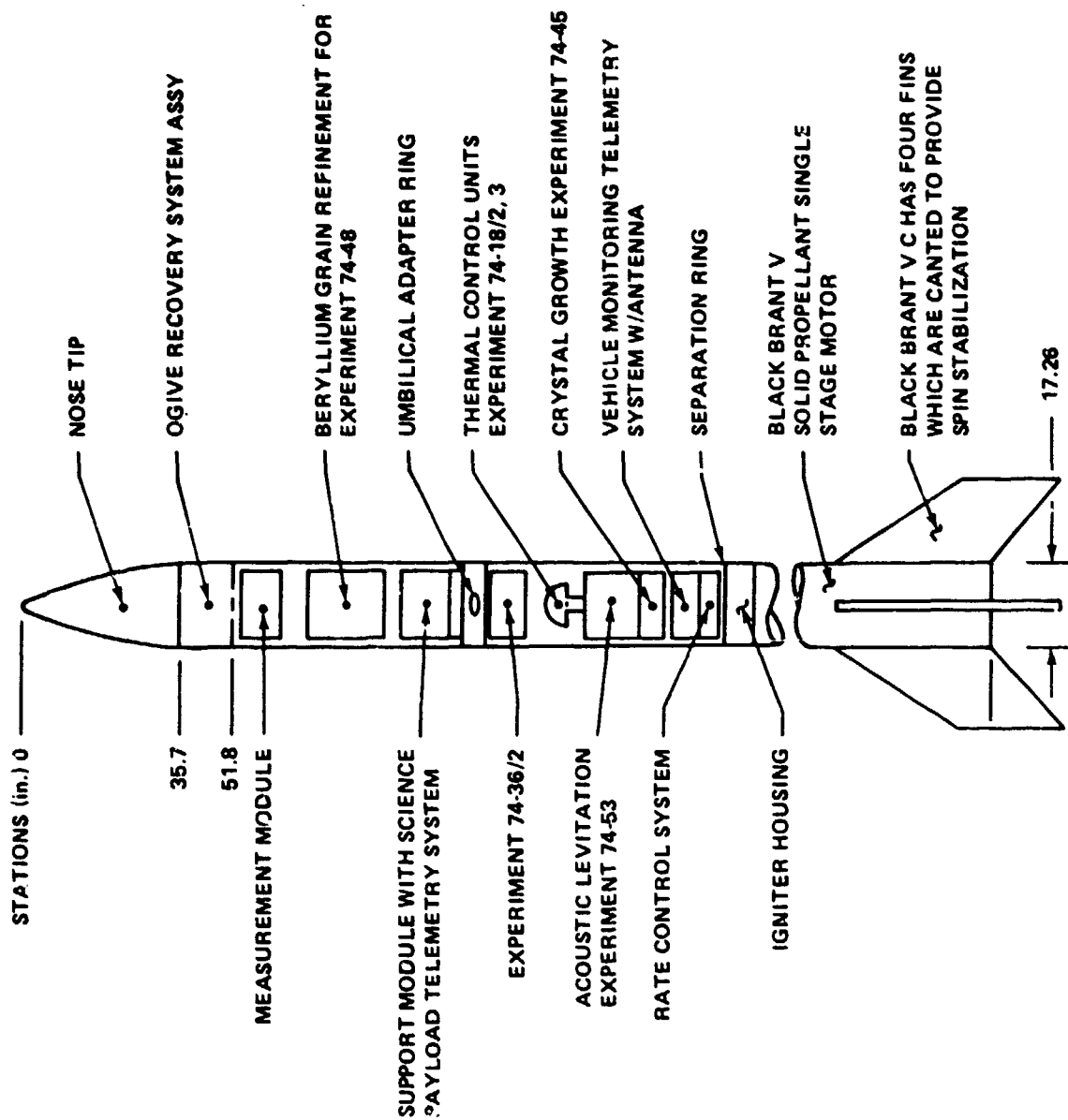
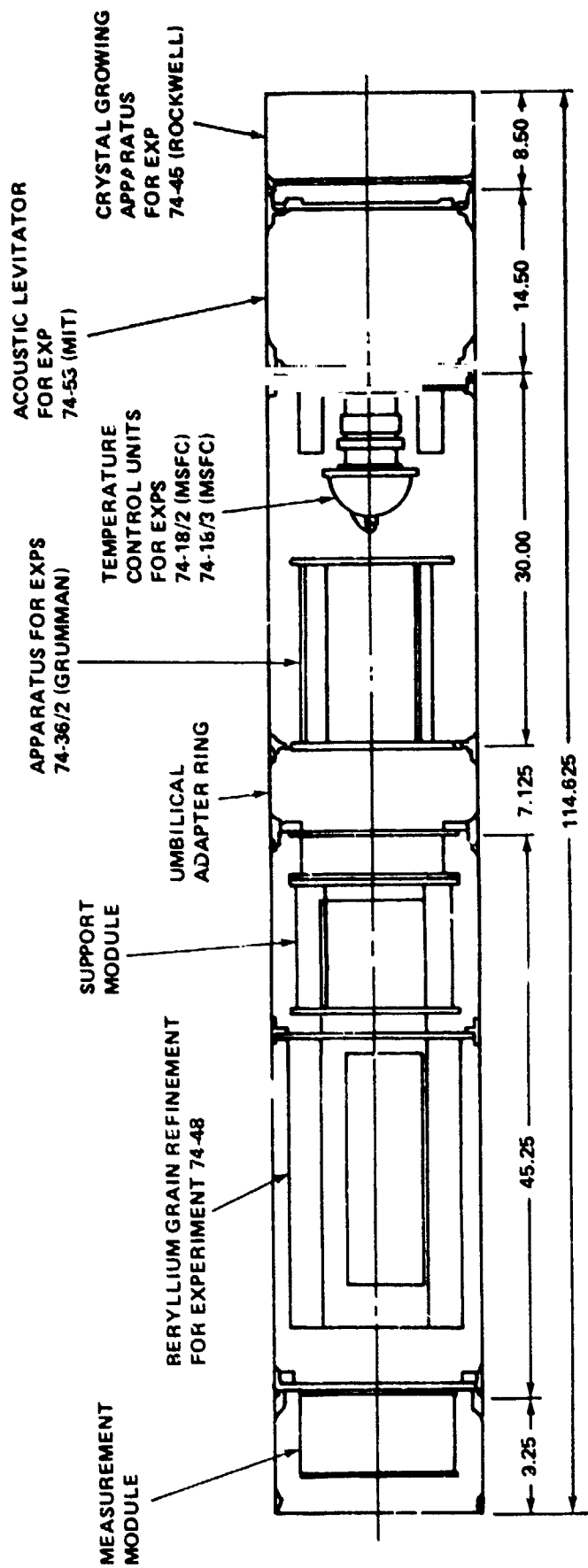


Figure 1. SPAR III rocket configuration.



← FLIGHT

Figure 2. SPAR III project payload.

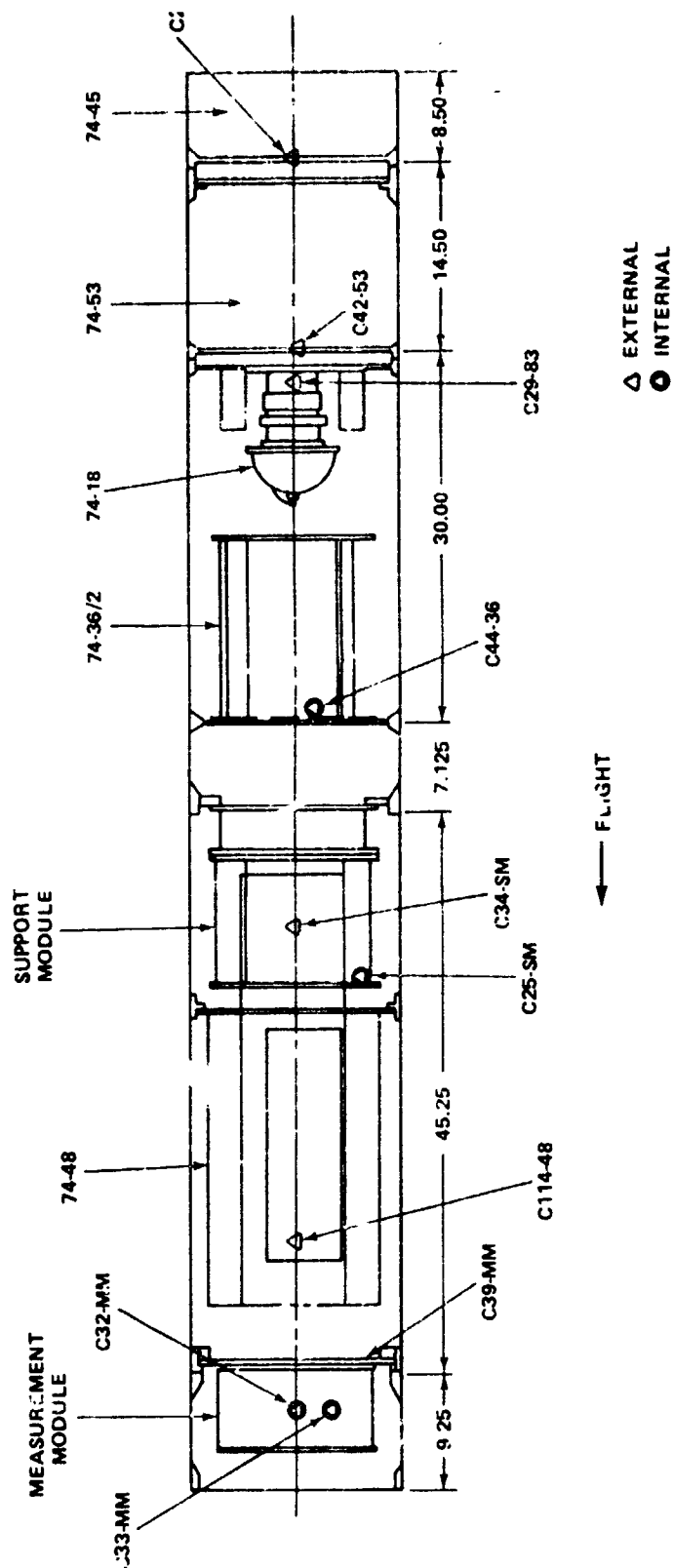


Figure 3. SPAR payload III engineering temperature measurements locations.

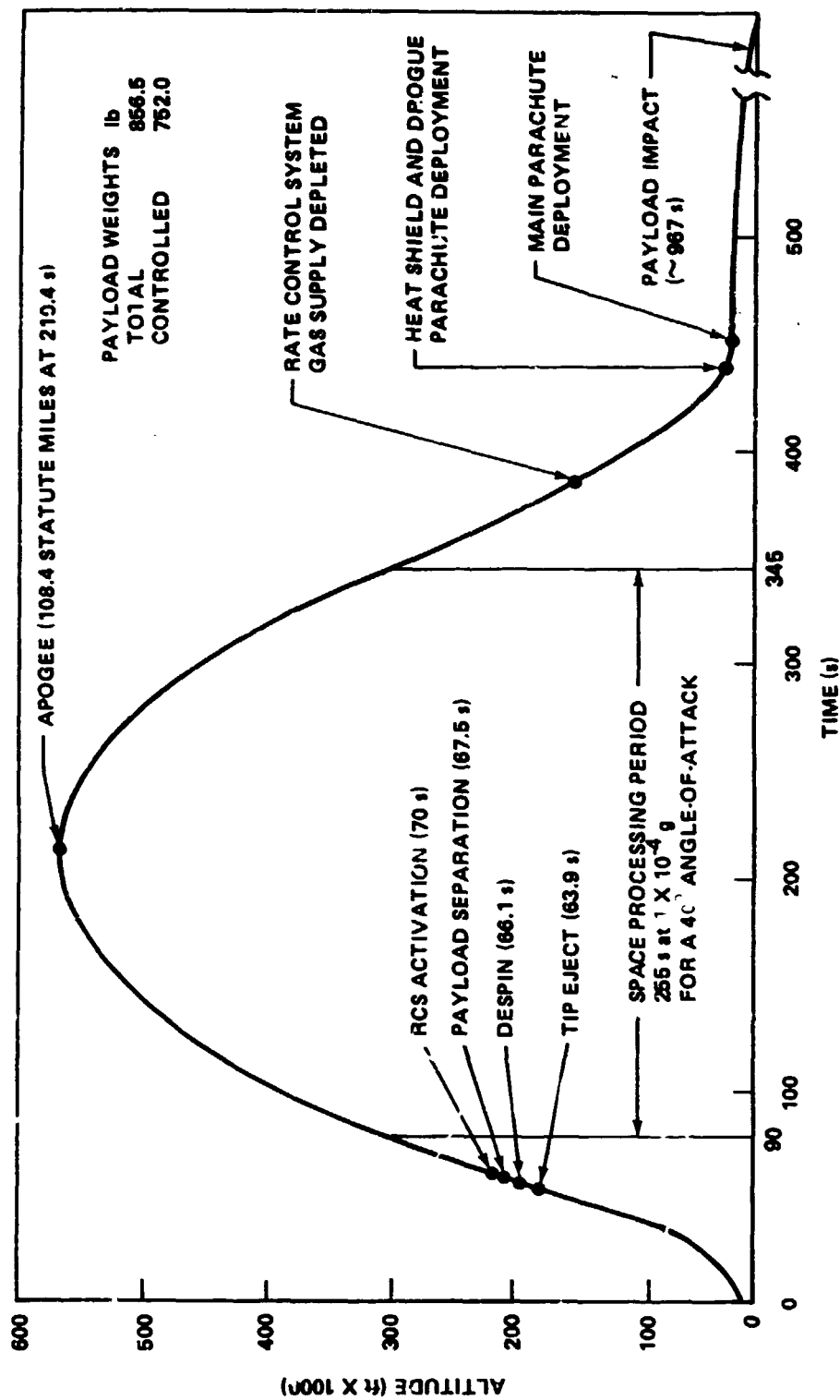


Figure 4. SPAR project payload III, Black Brant VC sounding rocket, NAS 21.034.NP
actual flight profile and events/conditions.

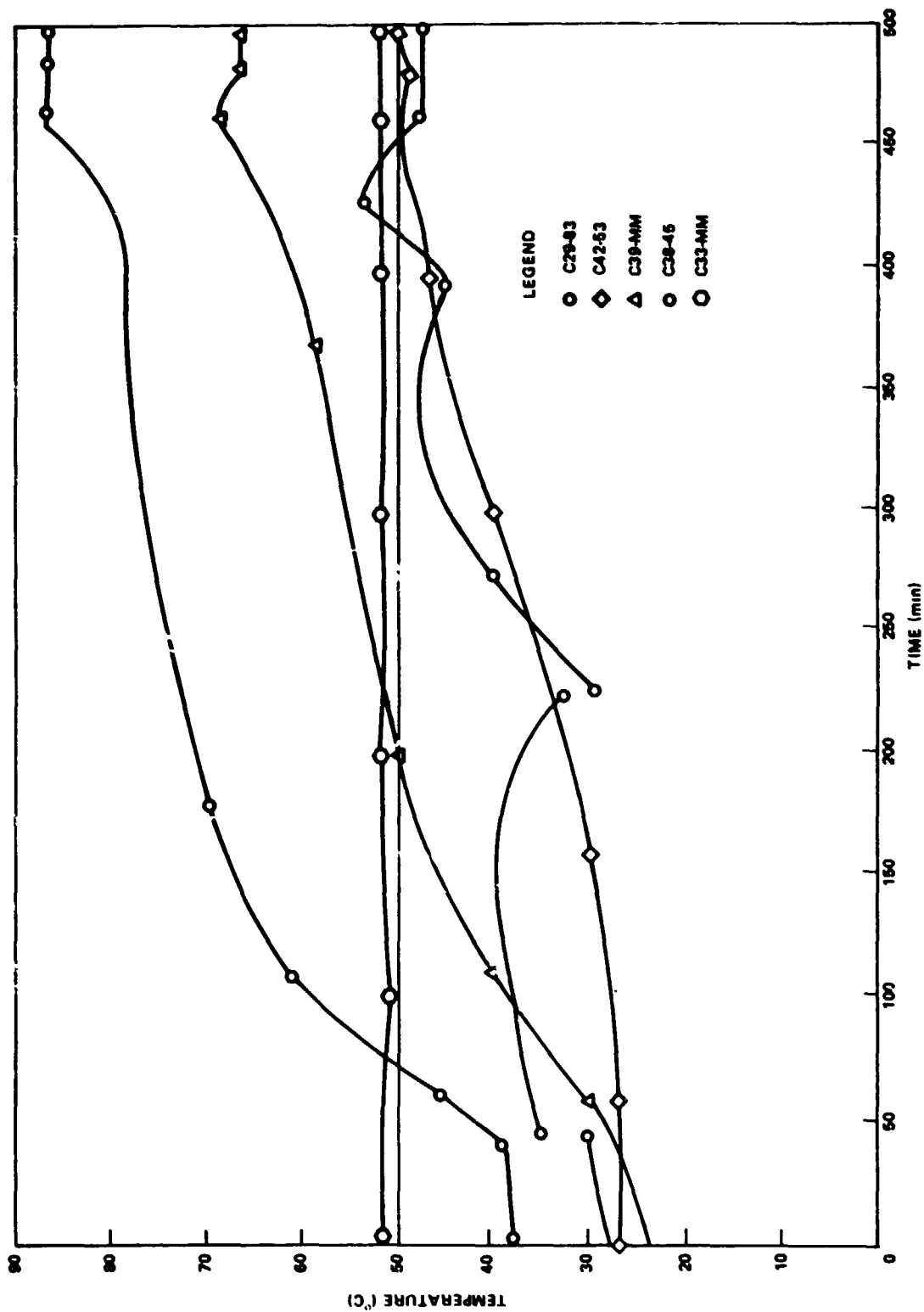


Figure 5. SPAR payload III temperature versus flight time.

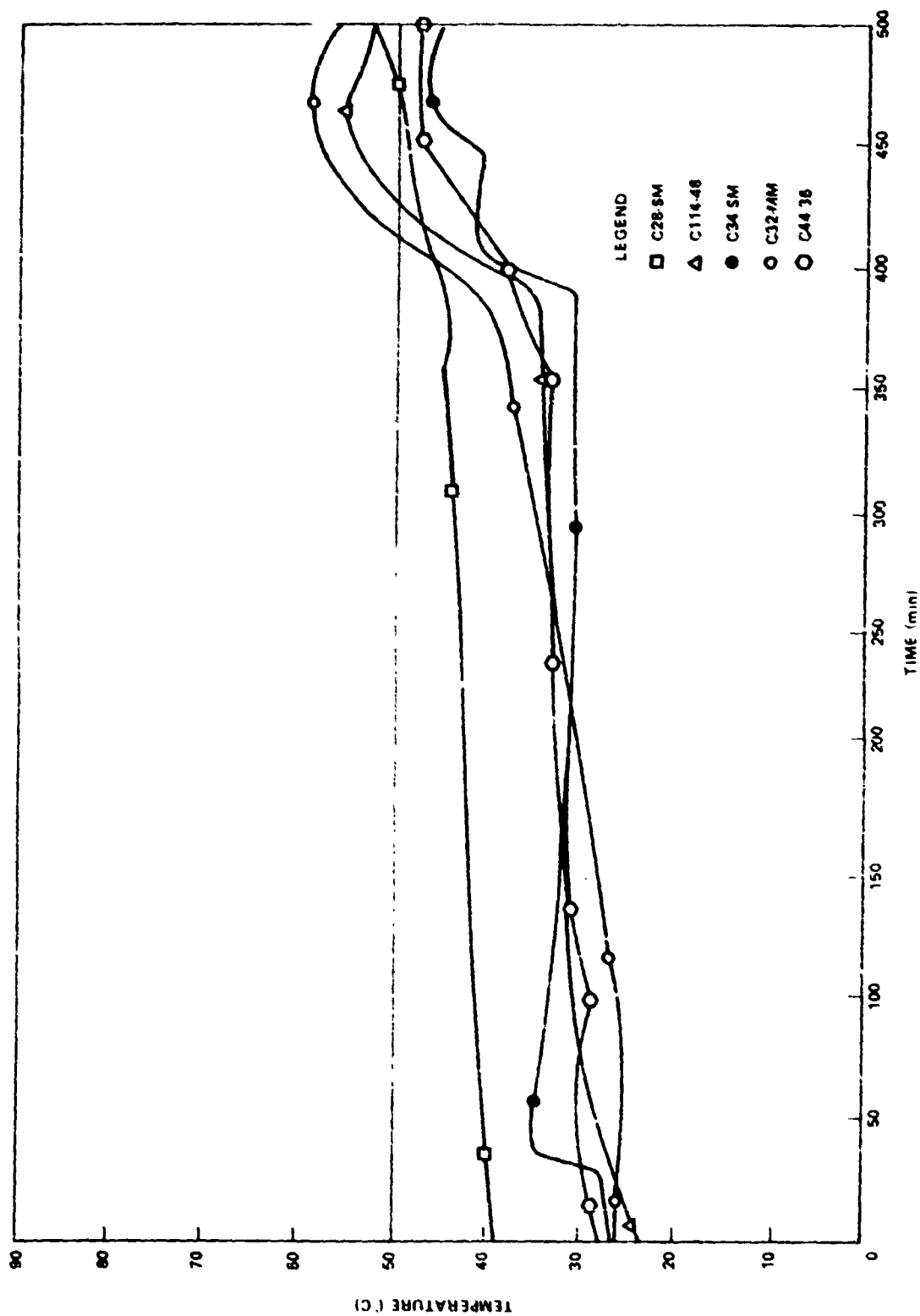


Figure 6. SPAR payload III temperature versus flight time.

CHAPTER II

SCIENCE PAYLOAD III TEST REPORT

By

T. F. Rowell

Marshall Space Flight Center

INTRODUCTION

Purpose

This report documents the testing and related activities during post-manufacturing checkout, integration, prelaunch, and launch of SPAR project payload III.

Scope

All significant testing and operations are presented from the arrival of SPAR project science payload III at MSFC, Building 4619 for post-manufacturing checkout, through launch operations at the White Sands Missile Range (WSMR). Tests are listed individually in sequence of performance and include procedure number, test title, objective(s), and test performance. A summary of discrepancy reports (DR's) and test discrepancy reports (TDR's) written during integration testing at Goddard Space Flight Center (GSFC) and during prelaunch and launch activities at WSMR are listed in Appendix B. The payload III actual test schedule is shown in Figure 1.

PRINTING PAGE BLANK NOT FILLED

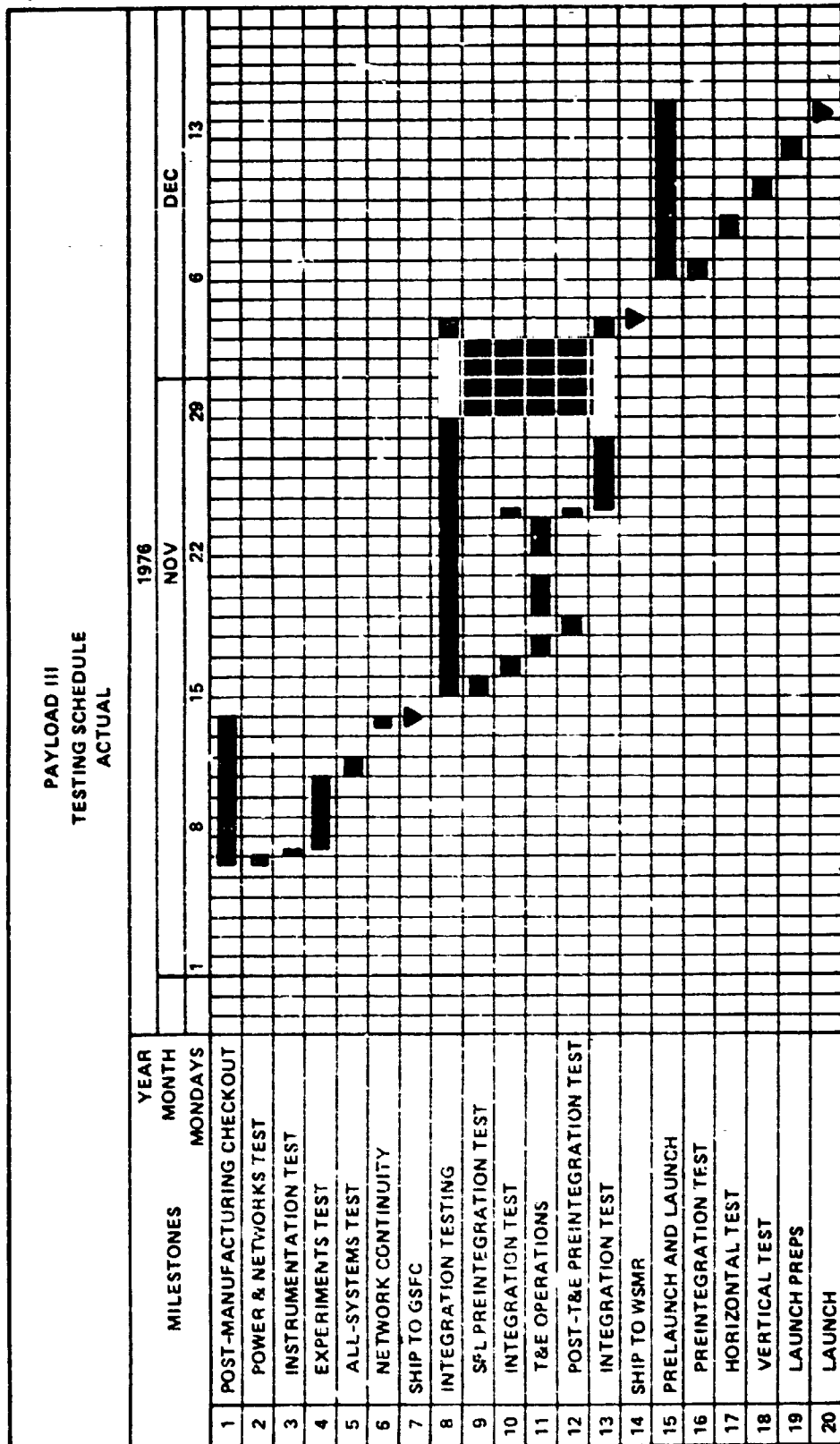


Figure 1. Actual test schedule.

POST-MANUFACTURING CHECKOUT

Test Title: Single Point Ground Isolation, Electrical Power, and Networks Subsystem

Procedure Number: MTCP-FS-SPAR-3-608

Test Objective:

The objectives of this test were to verify:

1. Single point ground isolation.
2. Proper power transfer between modules.
3. That the support module network circuitry conforms to systems design.

Test Performance:

The power and network subsystem was verified to conform to systems design. No anomalies occurred during the test.

Test Title: Instrumentation Subsystem Test

Procedure Number: MTCP-FS-SPAR-3-610

Test Objective:

The objectives of this test were to verify:

1. Proper transmitter deviation.
2. Subcarrier and commutated data channels
3. Proper operation of telemetry calibrator.

Test Performance:

The objectives of this test were met successfully. One anomaly occurred during the test. Support module voltage regulator A5 output terminal shorted to case. The voltage regulator was removed, repaired, and retested satisfactorily. Reference DR 1386 and TDR M-SPAR-3-610-1.

Test Title: Subsystem Test Procedure, Experiment 74-18-2 and 3

Procedure Number: MTCP-FS-SPAR-3-613

Test Objective:

To operate the experiment in a payload configuration using the ground support equipment (GSE) and to verify event timer operation.

Test Performance:

The objectives of the test were met successfully. Anomalies occurring during the test were:

1. The heater resistance of 74-18/2 thermal control unit (TCU) heater measured 14.0Ω and should have been 14.7 to 15.3Ω . The specification was changed, with PI concurrence, to bring measured resistance within acceptable limits. Reference TDR M-SPAR-3-613-1.
 2. The heater resistance of 74-18/3 TCU heater measured 10.5Ω and should have been 11.0 to 11.6Ω . The specification was changed to bring measured resistance within acceptable limits. Reference TDR M-SPAR-3-613-2.
 3. Transients were generated by support module and Experiment 74-18 event timers randomly when power was applied to the event timers. System configuration changes due to the transients were corrected by procedure. Reference DR 1415 and TDR M-SPAR-3-613-3.
-

Test Title: Subsystem Test Procedure, Experiment 74-53.

Procedure Number: MTCP-FS-SPAR-3-614

Test Objective:

To operate the experiment in a payload configuration and to demonstrate experiment-GSE compatibility.

Test Performance:

The objectives of the test were met successfully. One anomaly was detected during the test. The experiment event timer functions started when power was applied to the experiment instead of a signal from the liftoff relays. Two transient paths were randomly setting the event timer start relay. One path was from the support module liftoff relay, the transient being generated when payload power was applied. The second path was from the experiment GSE panel simulated liftoff circuit, the transient being generated when GSE panel power was applied. A relay, set by experiment power application, was put in series with the liftoff relay to stop the transient generated by payload power application. The simulated liftoff circuit in the experiment GSE panel was eliminated. The circuit was not used for test and launch activities. Reference TDR M-SPAR-3-614-1.

Test Title: Subsystem Test Procedure, Experiment 74-36

Procedure Number: MTCP-FS-SPAR-3-611

Test Objective: ---

To verify proper operation of the experiment and to demonstrate experiment-GSE compatibility.

Test Performance:

Operation of the experiment and compatibility of the experiment and GSE were verified. Test samples were heated to operating temperature. No anomalies occurred during the test.

Test Title: Subsystem Test Procedure, Experiment 74-45

Procedure Number: MTCP-FS-SPAR-3-612

Test Objective:

To verify proper operation of the experiment and to demonstrate experiment-GSE compatibility.

Test Performance:

Operation of the experiment and compatibility of the experiment and GSE were verified. One anomaly occurred during the test. The event times of slider extend and retract were 251 s and 307 s, respectively. The extend time expected was 254 (± 2) s and the retract time expected was 314 (± 1) s. The actual times were acceptable and the specifications were changed per CCBD SPAR 224 to bring the event times within acceptable limits. Reference TDR M-SPAR-3-612-1.

Test Title: Subsystem Test Procedure, Experiment 74-48

Procedure Number: MTCP-FS-SPAR-3-609

Test Objective:

To verify operation of the experiment and to demonstrate experiment-GSE compatibility.

Test Performance:

Operation of the experiment and compatibility of the experiment and GSE were verified. No anomalies occurred during the test.

Test Title: All Systems Test

Procedure Number: MTCP-FS-SPAR-3-615

Test Objective:

To functionally verify systems operational compatibility and to detect nonconformances to test requirements and specifications.

Test Performance:

The objectives of this test were met successfully. All systems were verified to be operational and compatible. Anomalies occurring during the test were:

1. The input cable to the charge amplifier for measurement E02-MM, vibration X-axis, was loose. The cable was reconnected and the measurement operated as designed. Reference TDR-M-SPAR-3-615 1.

2. Water was dumped into the lower cavity of the TCU for both 74-18/2 and 74-18/3 prematurely when power was applied to the experiments. The relays controlling the solenoid valves to dump water into the lower cavity for cooling were not reset when water was placed into the TCU reservoir. Power application to the experiment allowed solenoid operation and dumping of the water. The TCU's were removed and dried and the relay system reconfigured. Operation of the TCU's during the test were normal. Reference TDR-M-SPAR-3-615-2.

3. The measurement range resistors in signal conditioner board A3 for measurements C29-S3, temperature 74-18/3 external, and C78-S2, temperature 74-18/2 external were of the wrong values producing erroneous measurement readings. The resistors in the signal conditioning board were changed (from 1K to 46.4K) and measurements were verified satisfactorily. Reference DR 1396 and TDR's M-SPAR-3-615-3 and 4.

4. The event timer for Experiment 74-53 started when power was applied to the experiment instead of receipt of the simulated liftoff signal. Elimination of the transient paths detected during subsystem testing had not eliminated the problem. This anomaly was overcome by applying power to the experiment by the liftoff relays. Reference DR 1414.

5. The camera for Experiment 74-36 was operating at 1.04 frames/s, out of the specification of 1.0 frames/s maximum. The frame rate was acceptable to the PI. Reference DR 1413.

6. Measurement D06-18, space payload ambient pressure, input to telemetry was greater than 6.5 V at ambient causing noise on the telemetry channel. Measurement was used "as is." Reference DR 1412.

Test Title: Network Continuity Test

Procedure Number: MTCP-FS-SPAR-3-636

Test Objectives:

To verify that systems operation remains acceptable and that network cabling remains unchanged after installation in the payload housing.

Test Performance:

The objectives of this test were met successfully. No anomalies occurred during the test.

INTEGRATION TESTING

Test Title: Science Payload Preintegration Test

Procedure Number: GTCP-FS-SPAR-3-618

Test Objective:

To functionally verify that no damage occurred to science payload systems during transporting operations.

Test Performance:

Science payload systems were verified to be functional. No anomalies occurred during the test.

Test Title: Integration Test

Procedure Number: GTCP-FS-SPAR-3-619

Test Objective:

To verify that the science payload and rocket systems perform as designed when mated.

Test Performance:

The objective of this test was met successfully. All systems were operated through a simulated flight sequence. Anomalies occurring during the test were:

1. The science payload battery measurement, M01-SM, had no output through telemetry. The measurement monitors the battery voltage through the liftoff relay K16. A wiring error in the support module GSE panel simulated liftoff switch resulted in a constant voltage applied to the set side of the K16 coil preventing relay operation. The wiring error was corrected and liftoff relays and measurement operated properly. Reference TDR's G-SPAR-3-619-1 and G-SPAR-3-621A-1.

2. The telemetry output of the science payload ambient pressure measurement, D06-18, indicated a pressure range lower than ambient when sensor was at ambient pressure. Test of the pressure measurement through three of six ranges with a vacuum pump showed the measurement would indicate correct pressure. The pressure measurement was used without changes. Reference TDR G-SPAR-3-619-2.

SCIENCE PAYLOAD VIBRATION

The science payload without rocket systems was vibrated at protoflight levels in X, Y, and Z axis. The vibration levels during the test were:

Sine Spec. — 10 to 24 Hz at 0.075 in. double amplitude
24 to 110 Hz at 2.3 g maximum peak
110 to 800 Hz at 5.3 g maximum peak
800 to 2000 Hz at 15.0 g maximum peak

Random — 19.1 gm

No science payload systems were active during the vibration. All batteries were installed, but only Experiment 74-48 battery was connected electrically. The camera for Experiment 74-36, which had been subjected to previous vibration, was removed for vibration. Experiment 74-53 positive pressure system was pressurized to 1200 psi, and Experiment 74-45 slider mechanism cylinder was pressurized to 100 psi. Water was not installed in the TCU reservoirs.

Post vibration inspection of the science payload revealed the following three discrepancies:

1. Screw loose on cable connector clamp on cable to Experiment 74-45 solenoid.
2. Adjustment screw was loose on Experiment 74-45 regulator.
3. Cable connector loose on Experiment 74-53 solenoid.

The screws and connector were tightened and no further problems with the discrepant items occurred. Reference TDR G-SPAR-3-Protoflight Vibration.

Test Title: Post-Protoflight Vibration Science Payload Test

Procedure Number: GTCP-FS-SPAR-3-621A

Test Objective:

To verify that science payload systems operation was not degraded when subjected to a vibration environment.

Test Performance:

The objective of this test was met successfully. All systems were verified to be operational. Anomalies occurring during the test were:

1. Experiment 74-53 did not receive a signal at simulated liftoff. The error in wiring of the simulated liftoff GSE circuit, as discussed previously, prevented the signal being sent to the experiment. After correction of the simulated liftoff GSE circuit wiring, Experiment 74-53 was tested without problems. Reference TDR G-SPAR-3-621A-1.
 2. Measurement M31-48, 74-48 PF power output, was biased at 1.0 V instead of ground reference. Pin Z of Experiment 74-48 electronic package board No. 1, which carries regulated +15 V to the servo and coil power monitoring circuits, was broken. The voltage was routed to the circuits through pin Y of electronic board No. 1. Retest of the experiment was satisfactory. Reference TDR G-SPAR-3-621A-2.
-

BALANCE AND VIBRATION

Balance

The balance of the total payload, not including nose cone, was made at a rotation of 150 rpm on a spin-balance table. The lower plane for weights was in the rocket systems and the upper plane at 3.0 in. below the top of the science payload forward extension section. The balance weight mounted in the science payload at the upper plane was 1527 gm centered at 60 deg from 0 centerline.

Vibration (Procedure Number: GTCP-FS-SPAR-2-627)

The total payload was vibrated in X, Y, and Z axes and vibrations of sine sweep, sine spec, and random in each axis. The vibration levels during test were:

Sine Sweep — 10 to 20 Hz at 0.25 g peak; 20 to 2000 Hz at 1 g peak.

Sine Spec. — 110 to 800 Hz at 3.5 g; 800 to 2000 Hz at 10 g.

Random Spec. — 20 to 1000 Hz, 0.01 to 0.10 g^2/Hz ; 1000 to 2000, 0.10 g^2/Hz .

The science payload telemetry system and measurement module were active during vibration, and data transmission was monitored. No experiments were active. Review of telemetry data indicated no anomalies. Visual inspection of the payload showed no structural damage. Vibration testing was performed with water installed in the reservoirs of 74-18/2 and 74-18/3 and a flight type battery installed. Experiment 74-53 and 74-48 batteries were installed. Experiment 74-53 "Positive Pressure" bottle was pressurized to 1200 psi. The leak rate of the system was less than 2 psi/h. The camera for Experiment 74-36 was removed for vibration.

Test Title: Science Payload Post-T&E Preintegration Test

Procedure Number: GTCP-FS-SPAR-3-620

Test Objective:

To verify that systems operation was not degraded when subjected to a vibration environment.

Test Performance:

The objective of this test was met and all systems were verified to be operational. No anomalies occurred during the test.

Test Title: Post-Vibration Integrated Test

Procedure Number: GTCP-FS-SPAR-3-621

Test Objective:

To verify that the science payload and rocket systems perform as designed when mated.

Test Performance:

The objectives of this test were met. Flight type payload batteries were used for payload power. Experiment 74-45 was inoperative during the test because the system could not be controlled from the GSE. Anomalies occurring during the test were:

1. Experiment 74-45 furnace temperature could not be controlled through GSE. Components in the experiment furnace electronic control circuit were found defective. The components in the control circuit were replaced and the system verified. Reference TDR G-SPAR-3-621-1.
2. Experiment 74-48 camera stopped operation during the test. The film take-up reel was not seated on the motor drive and did not take up the film, resulting in jamming of the camera. Film was replaced in the camera and the camera was retested satisfactorily. Reference G-SPAR-3-621-2.
3. Measurement K03-36, camera output pulse, showed erratic camera operation of Experiment 74-36 camera for approximately 2 s. No cause could be found for the erratic operation. Retest of the camera was without problems. Reference TDR G-SPAR-3-621-3.

4. The umbilical connector on GSE cable W19 would not lock. The connector was replaced. Reference TDR G-SPAR-3-621-4.

5. One wire was loose on the thermistor for measurement C114-48, 74-48 engineering temperature. The thermistor was replaced and verified. Reference TDR G-SPAR-3-621-5.

BEND TEST

The bend test was made with the science payload and rocket systems mated. The bend force in increments to 1800 lb maximum was applied in each of four axis: +X, -X, +Y, and -Y. The canister containing Experiment 74-53 was pressurized to 30 psia throughout the test. There was no pressure loss from the canister. No structural damage was detected during inspection of the science payload after the test.

Test Title: Post-Bend Integrated Test

Procedure Number: GFCP-FS-SPAR-621

Test Objective:

To verify that the mated science payload and rocket systems operate as designed.

Test Performance:

The objectives of the test were met successfully. All systems, except Experiment 74-18, were operated through a simulated mission. Experiment 74-18 was satisfactorily tested prior to the integrated test per TDR G-SPAR-3-621A-2; therefore, the work chamber was removed and returned to the PI for installation of the flight sample. Anomalies during the test were:

1. A wire was loose on Experiment 74-15 slider position monitor terminal. The wire was resoldered and the circuit verified. Reference TDR G-SPAR-3-621-6.

2. Experiment 74-53 event times were changed prior to the post-bend integrated test. The actual event times were a maximum of 4 s out of specification. The actual event times were acceptable to the PI and the timer was used as set. Reference TDR G-SPAR-3-621-7.

PRELAUNCH TESTING AND LAUNCH

Test Title: Science Payload Preintegration Test

Procedure Number: WSTC-FS-SPAR-3-623

Test Objective:

To functionally verify that no damage occurred to science payload systems during transporting operations.

Test Performance:

All systems were verified to be functionally operational and no damage had occurred. No anomalies occurred during the test.

Test Title: Rocket 21.034 Horizontal Test

Procedure Number: WSTC-FS-SPAR-3-625

Test Objectives:

To verify that the science payload and rocket systems operate as designed and that ground support systems are ready to support a launch.

Test Performance:

The objectives of this test were met successfully. All systems were operated through a simulated mission. The TCU's for Experiments 74-18/2 and 74-18/3 were operated with water quench. Experiments 74-45 and 74-48 contained flight samples and were not operated through a simulated flight sequence. Anomalies during the test were:

1. Times of Experiment 74-53 event timer were changed prior to the horizontal test. The actual event times were not as specified by the PI but were acceptable. The event timer was used with times set. Reference TDR W-SPAR-3-625-1.

2. Measurement C81-83, temperature 74-18/3 No. 2, was noisy during a period of heat and water quench. The noise was not excessive and was used "as is." Reference TDR W-SPAR-3-625-2.

3. During installation of the flight samples in the TCU's of Experiments 74-18/2 and 74-18/3 (after completion of the horizontal test), the heater coils for samples 4 and 6 of the TCU for 74-18/3 broke. The TCU was returned to MSFC and new heater coils installed. The TCU was verified at MSFC before being returned to the launch site and installation into the payload. Reference TDR W-SPAR-3-625-3.

Test Title: Rocket 21.034 Vertical Test

Procedure Number: WSTC-FS-SPAR-3-626

Test Objective:

To verify the launch readiness of the rocket systems.

Test Performance:

All systems except Experiments 74-18/2, 74-18/3, 74-45, and 74-48, which were previously readied for launch, were operated through a simulated flight sequence. No anomalies occurred during the test.

The power control switch on Experiment 74-36 GSE TCU was damaged during installation on the launch tower. The switch was replaced and verified through use during the vertical test. Reference TDR W-SPAR-3-626-1.

Test Title: 21.034 NP Science Payload Countdown and Launch Procedure

Procedure Number: WTCP-FS-SPAR-3-628

Procedure Objective:

To perform close-out preparations of systems and to establish the systems configuration and necessary conditions of experiments for launch.

Test Performance:

The objectives of the countdown and launch procedure were met successfully. Flight payload battery SN07 was used for flight. The environmental temperature around the science payload was maintained at 71.0°F prior to launch. Two anomalies occurred during the countdown to launch:

1. The voltage output of Experiment 74-48 battery as monitored through telemetry was indicated to be below the minimum voltage of 24.0 V when subjected to a load. The battery was removed and an additional charge was applied to the battery. After additional battery charge, the battery was reinstalled and tested satisfactorily. Reference TDR W-SPAR-3-628-1.

2. No audible sound of film advance could be detected for each camera shutter operation during test of Experiment 74-36 camera. The camera was removed and the film replaced. Retest of the camera was satisfactory. Reference W-SPAR-3-628-2.

WEIGHT AND CENTER OF GRAVITY MEASUREMENT

Measurements of weight and center of gravity were made of the science payload and rocket systems prior to mate to the rocket motor. Measurements taken of the payload, minus the igniter housing and nose cone, were 754 lb weight and 72.6 in. from aft end of RCS unit for center of gravity.

LANDLINE VERIFICATION

Landlines between the blockhouse and launch tower were verified to be operational prior to science payload testing on the launch tower.

APPENDIX A

DISCREPANCY REPORT AND TEST DISCREPANCY REPORT SUMMARY

POST-MANUFACTURING CHECKOUT

<u>DR/TDR Number</u>	<u>Date Written/Closed</u>	<u>Description/Disposition</u>
1386	11/7/76	Support module voltage regulator shorted to case.
	11/9/76	Closed — Voltage regulator repaired and reverified.
1396	11/12/76	Measurement C78-82, temperature, 74-18/2 external, indicated wrong temperature at ambient.
	11/12/76	Closed — Resistor changed in signal conditioner board to provide measurement with correct range.
1395	11/12/76	Measurement C29-83, temperature 74-18/3 external, indicated wrong temperature at ambient.
	11/12/76	Closed — Resistor changed in signal conditioner board to provide measurement with correct range.
1414	11/12/76	Premature starts of Experiment 74-53 electronic timer.
	11/12/76	Closed — Use "as is." Correct by procedure.
1413	11/12/76	Shutter for Experiment 74-36 camera operated at 1.04 pulses/s, should be operating at 1.0 pulses/s maximum.
	11/12/76	Closed — Use "as is."
1412	11/12/76	Measurement D06-18, science payload ambient pressure, inputs greater than 6.5 V into telemetry causing noise on adjacent channels.

<u>DR/TDE Number</u>	<u>Date Written/Closed</u>	<u>Description/Disposition</u>
	11/12/76	Closed — Use "as is."
1401	11/12/76	Heater resistance of 74-18/2 TCU measured 14.0 Ω , should be 15.0 \pm 0.3 Ω .
	11/12/76	Closed — Use "as is."
1402	11/12/76	Heater resistance of 74-18/3 TCU measured 10.5 Ω , should be 11.3 \pm 0.3 Ω .
	11/12/76	Closed — Use "as is."
1415	11/12/76	Periodic erroneous operation of support module relays occurred when power was applied to payload.
	11/12/76	Closed — Use "as is." Correct by procedure.
M-SPAR- 3-610-1	11/7/76	Reference DR 1386.
	11/9/76	Closed — Voltage regulator tested satisfactorily.
M-SPAR- 3-613-1	11/7/76	Reference DR 1401.
	11/12/76	Closed.
M-SPAR- 3-613-2	11/7/76	Reference DR 1402.
	11/12/76	Closed.
M-SPAR- 3-613-3	11/7/76	Reference DR 1415.
	11/12/76	Closed.
M-SPAR- 3-614-1	11/8/76	Reference DR 1414.

<u>DR/TDR Number</u>	<u>Date Written/Closed</u>	<u>Description/Disposition</u>
	11/9/76	Closed.
M-SPAR- 3-611-1	11/8/76	Measurement C44-36, temperature 74-36/2 external, output was not within specification at ambient.
	11/10/76	Closed — Invalid calibration curve data used. Measurement tested satisfactory with valid calibration data.
M-SPAR- 3-612-1	11/8/76	Extend and retract time after simulated liftoff of Experiment 74-45 slider mechanism not within specification.
	11/12/76	Closed — Specification tolerance changed to bring slider mechanism operation within specification.
M-SPAR- 3-615-1	11/11/76	Measurement E02-MM, vibration X-axis, had 0 V output, should be 2.5 V.
	11/11/76	Closed — Cable to charge amplifier loose. Cable connected and measurement tested satisfactorily.
M-SPAR- 3-615-2	11/11/76	Water leak at lower cavity of Experiment 74-18/3 TCU.
	11/12/76	Closed — Relays controlling solenoid reset to prevent dump of water into lower cavity. TCU's removed, water removed, and unit dried. Units retested satisfactorily.
M-SPAR- 3-615-3	11/11/76	Reference DR 1396.
	11/12/76	Closed.
M-SPAR- 3-615-4	11/11/76	Reference DR 1395.

<u>DR/TDR Number</u>	<u>Date Written/Closed</u>	<u>Description/Disposition</u>
M-SPAR- 3-615-5	11 /11/76	Reference DR 1414.
	11/12/76	Closed.
M-SPAR- 3-615-6	11/11/76	Reference DR 1413.
	11/12/76	Closed.
M-SPAR- 3-615-7	11/11/76	Reference DR 1412.
	11 /12/76	Closed.

APPENDIX B

TEST DISCREPANCY REPORT SUMMARY INTEGRATION AND PRELAUNCH TESTING

<u>TDR Number</u>	<u>Date Written/Closed</u>	<u>Description/Disposition</u>
G-SPAR-3-619-1	11/16/76	Measurement M01-SM, science payload battery voltage, read 0 V during integrated test, should have read 3.0 V.
	11/20/76	Closed — Liftoff relay K16 was provided a constant 34.0 V from the GSE to the set coil, preventing relay operation and voltage to measurement M01-SM. GSE rewired and measurement verified. Reference TDR G-SPAR-3-621A-1.
G-SPAR-3-619-2	11/16/76	Measurement D06-18, science payload ambient pressure, indicated pressure lower than ambient during integrated test.
	12/2/76	Closed — Use "as is." Measurement operated properly when tested with vacuum pump.
G-SPAR-3-Protoflight Vibration	11/18/76	Loose screws noted after vibration.
	11/24/76	Closed — Screws tightened and verified to be tight after second vibration.
G-SPAR-3-621A-1	11/18/76	Experiment 74-53 timer functions did not start at simulated liftoff.
	11/20/76	Closed — Liftoff relay K16 was provided a constant 34.0 V from the GSE to the set coil, preventing relay operation at simulated liftoff. GSE rewired and experiment start verified.

<u>TDR Number</u>	<u>Date Written/Closed</u>	<u>Description/Disposition</u>
G-SPAR-621A-2	11/18/76	Measurement M31-48, Experiment 74-48 RF power output, was biased at 1.0 V during integrated test, should be at ground voltage.
	12/2/76	Closed -- Broken pin on electronics board repaired. Experiment retested satisfactorily.
G-SPAR-3-621-1	11/26/76	Experiment 74-45 furnace temperature could not be controlled from GSE.
	12/1/76	Closed -- Electronic card for ground control repaired and replaced. Furnace control from GSE tested satisfactorily.
G-SPAR-3-621-2	11/26/76	Experiment 74-48 camera stopped operation during integrated test.
	11/26/76	Closed -- Film did not take up on reel. Take up reel and film replaced and camera retested satisfactorily.
G-SPAR-3-621-3	11/26/76	Experiment 74-36 camera output measurement, K03-36, showed erratic operation for 2 s during integrated test.
	11/27/76	Closed -- Film replaced and camera retested satisfactorily.
G-SPAR-3-621-4	12/1/76	Umbilical connector on GSE cable W19 will not lock to umbilical J12.
	12/2/76	Closed -- Connector replaced on cable W19.
G-SPAR-3-621-5	12/1/76	Wire loose on engineering temperature thermistor for measurement C114-48.
	12/2/76	Closed -- Thermistor replaced and verified.

<u>TDR Number</u>	<u>Date Written/Closed</u>	<u>Description/Disposition</u>
G-SPAR-3-621-6	12/2/76	Wire loose on Experiment 74-45 slider position monitor.
	12/2/76	Closed — Wire resoldered and verified.
G-SPAR-3-621-7	12/2/76	Experiment 74-53 acoustic field operation not within specification.
	12/2/76	Closed — Use "as is."
W-SPAR-3-625-1	12/8/76	Experiment 74-53 acoustic field operation not within specification.
	12/8/76	Closed — Use "as is."
W-SPAR-3-625-2	12/8/76	Measurement C81-83, temperature 74-18/3 No. 2, noisy during furnace operation.
	12/9/76	Closed — Use "as is."
W-SPAR-3-625-3	12/9/76	Experiment 74-18/3 TCU coils for samples 4 and 6 broke during sample removal.
	12/11/76	Closed — Coils replaced and verified.
W-SPAR-3-626-1	12/9/76	Toggle switch on Experiment 74-36 GSE TCU.
	12/9/76	Closed — Switch replaced and verified.
W-SPAR-3-628-1	12/14/76	Battery voltage of Experiment 74-48 battery did not indicate minimum required voltage of 24.0 V when tested.
	12/14/76	Closed — Battery recharged and verified.
W-SPAR-3-628-2	12/14/76	No audible sound of film advance of Experiment 74-36 camera when tested.
	12/14/76	Closed — Film replaced and camera film advance verified.

CHAPTER III

LIQUID MIXING

Experiment 74-18

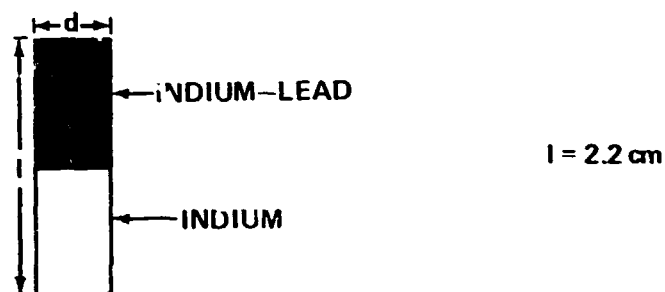
By

C. F. Schafer and G. H. Fichtl

Marshall Space Flight Center

~~RECORDING PAGE BLANK NOT FILMED~~
INTRODUCTION

The SPAR I payload, flown in December 1975, contained an experiment which had the objective of observing the effects of residual acceleration of the payload on a confined fluid system. The fluid system was chosen to be similar in geometry and in fluid properties to a class of materials science experiments. The samples were composed of two cylindrical sections each 2.2 cm long and 0.6 cm in diameter (Fig. 1). One cylindrical section was composed of pure In and the other of an alloy of 80 wt % In and 20 wt % Pb [1] (Fig. 2). The samples were enclosed in aluminum containers and placed in heaters. The experimental procedure consisted of melting the samples after the low-g portion of the payload trajectory had been achieved and then quenching them to solidification before leaving low-g. The returned samples were analyzed using X-ray radiographic techniques (Fig. 3) to determine whether flow had taken place due to the action of any residual accelerations on the density-stratified liquid metal samples. The results are shown in Figure 4. Sample 3 exhibited large scale, roughly antisymmetric flow with respect to a plane containing the cylinder axis. Samples 1 and 2 exhibited no large scale flows. These results were related to theoretical models and to ground-based experiments [2], both of which will be discussed in some detail. The predictive value of these theoretical and experimental considerations was an open question pending a repetition of the SPAR I experiment. The opportunity came to repeat the SPAR I experiment and to extend the experiment to cover samples of different aspect ratios on the SPAR III flight. Two TCU's were made available (Fig. 5). These were designated



FOR SPAR I - ALL SAMPLES HAD $d = 0.6$ cm

FOR SPAR III -
 { SAMPLES No. 1, No. 2, No. 3, No. 4 HAD $d = 0.6$ cm
 { SAMPLES No. 5 HAD $d = 0.45$ cm
 { SAMPLES No. 6 No. 7 HAD $d = 0.3$ cm

Figure 1. Samples for the SPAR liquid mixing experiments.

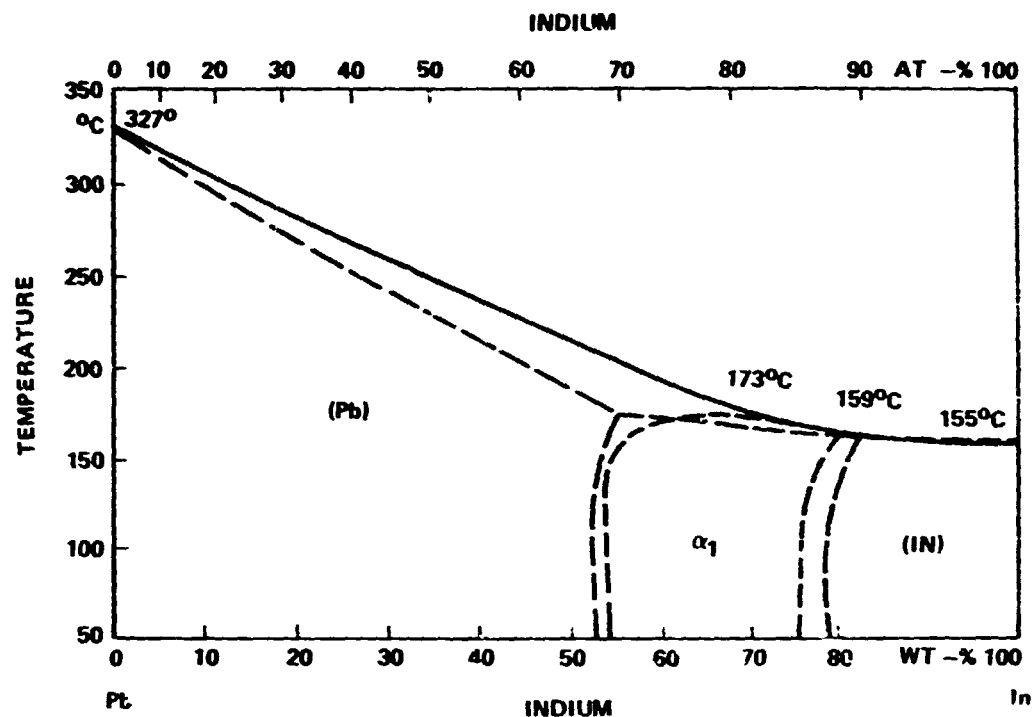


Figure 2. Indium-lead equilibrium phase diagram.

Experiments 74-18/2 and 74-18/3 and were mounted in the payload in the configuration shown in Figure 6. The SPAR III experiment timeline is shown in Figure 7. It is noted that total experiment time is slightly shorter than for SPAR I, with the samples being molten for approximately 180 s. The returned samples were subjected to X-ray radiographic analysis to determine whether flows had occurred.

EXPECTED RESULTS

The SPAR I liquid mixing experiment yielded results consistent with the application of a constant magnitude radial force (arising from residual rotation) on the liquid samples with a magnitude in the 10^{-6} g to 10^{-5} g range. If we anticipate that the SPAR III payload is subject to the same conditions, we see that forces on samples 2, 3, and 7 acted parallel to the original interface between the In and In-Pb (Fig. 8). The fluid mechanics problem presented here is that of a cylinder lying on its side with a constant body force applied vertically. The density distribution in the sample is originally given by a step

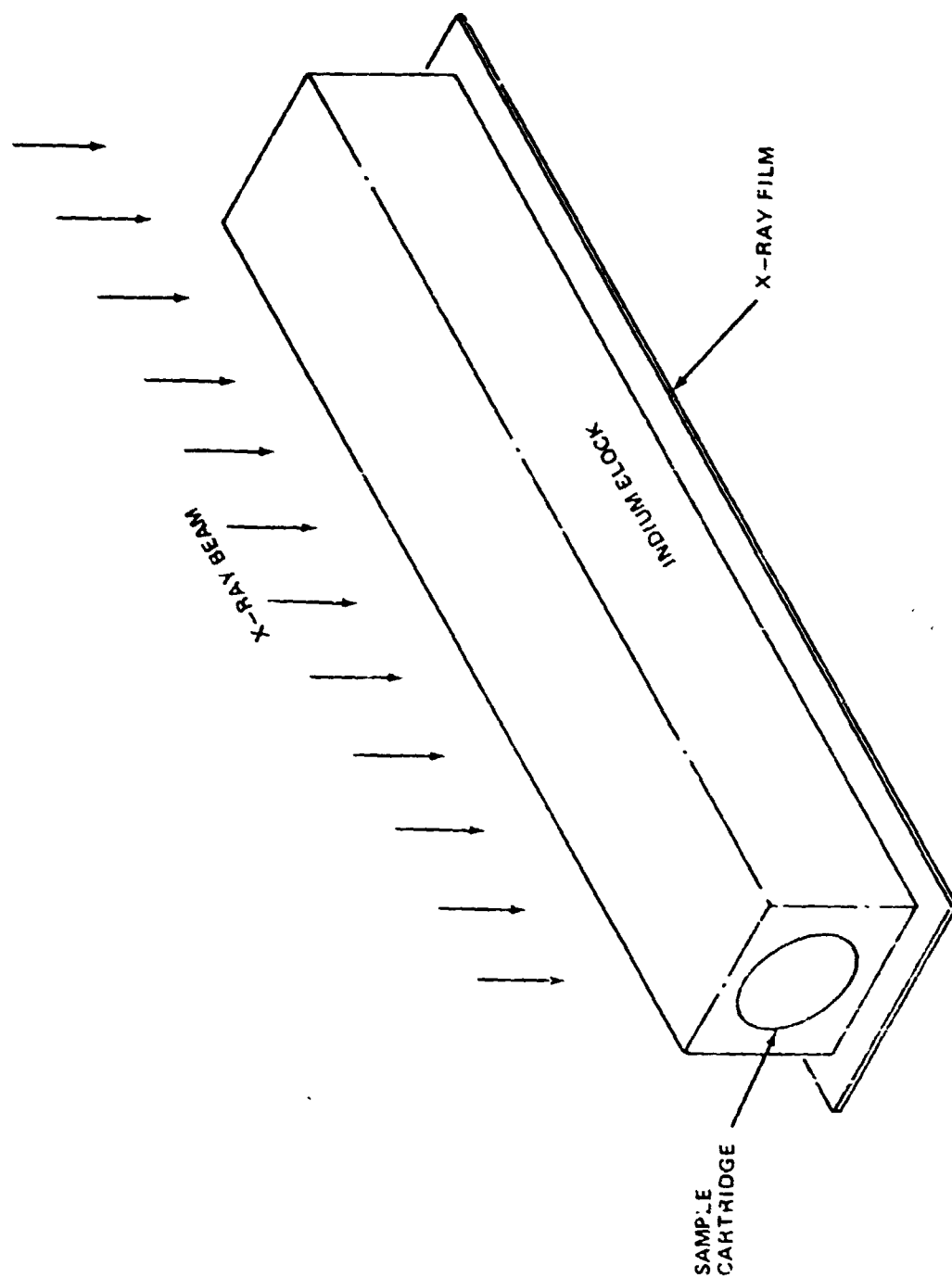


Figure 3. X-ray radiographic technique used on returned samples.

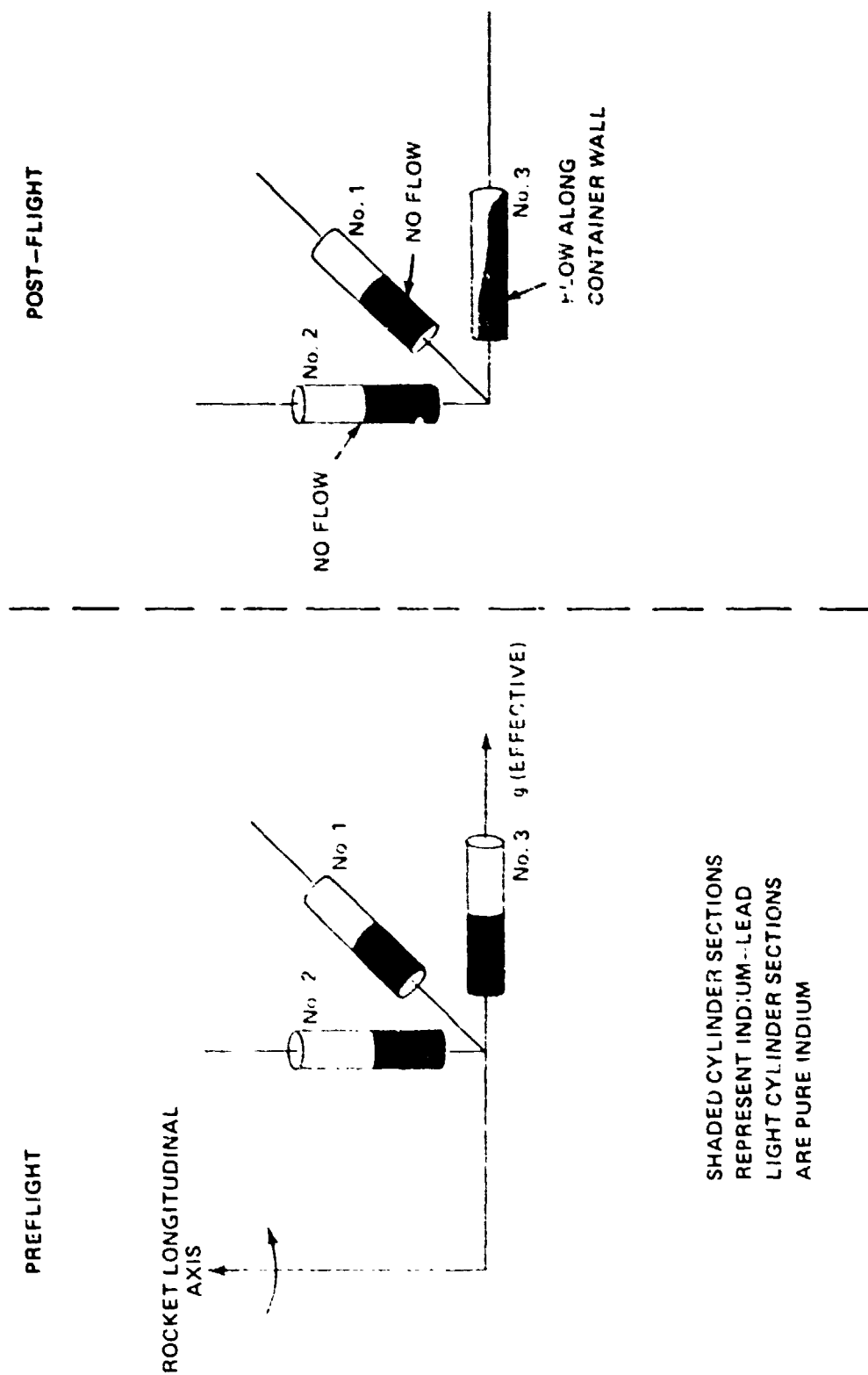


Figure 4. SPAR liquid mixing experiment results.

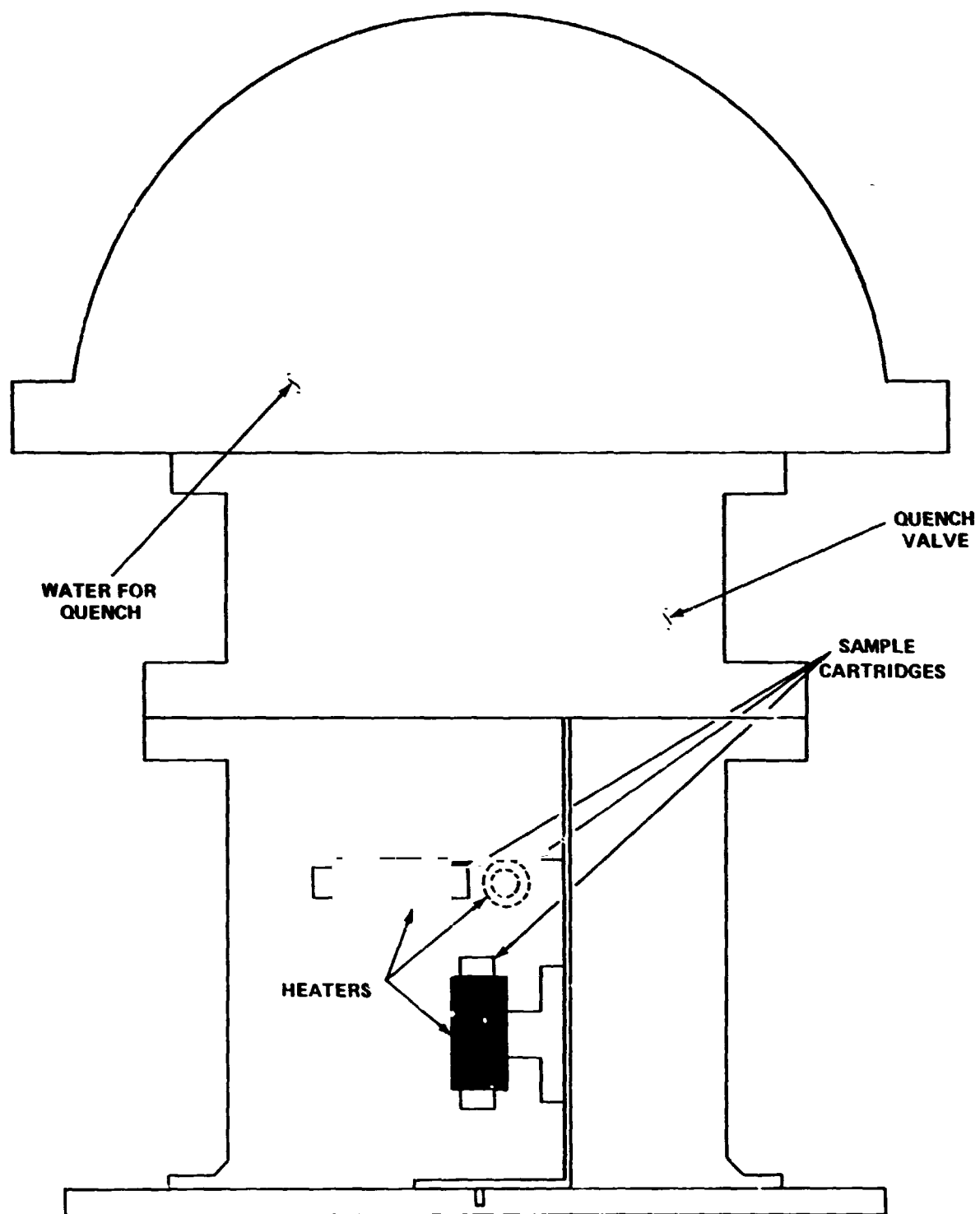


Figure 5. Thermal control unit.

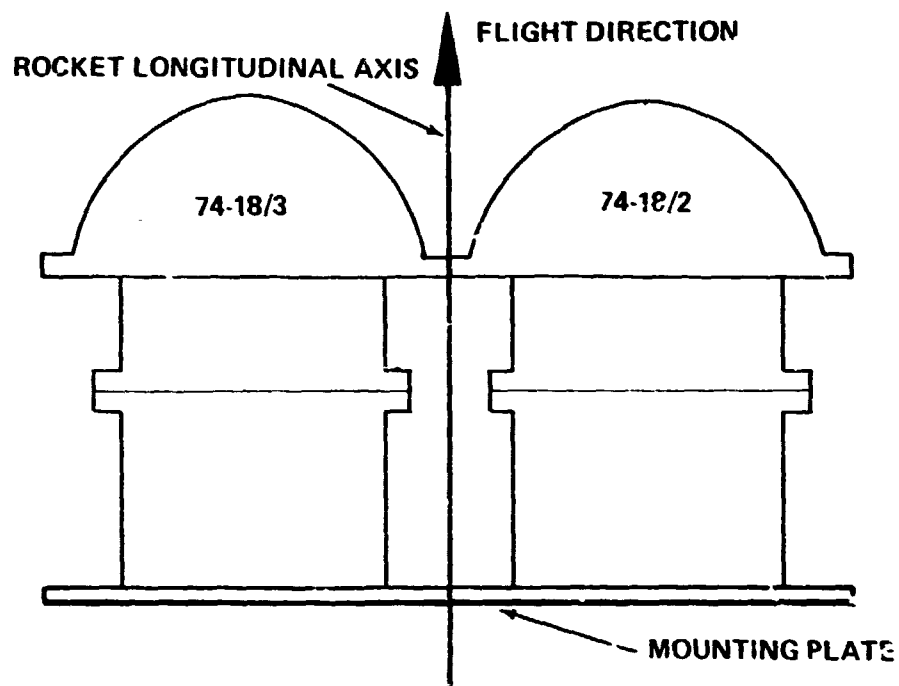


Figure 6. Thermal control units as mounted in payload.

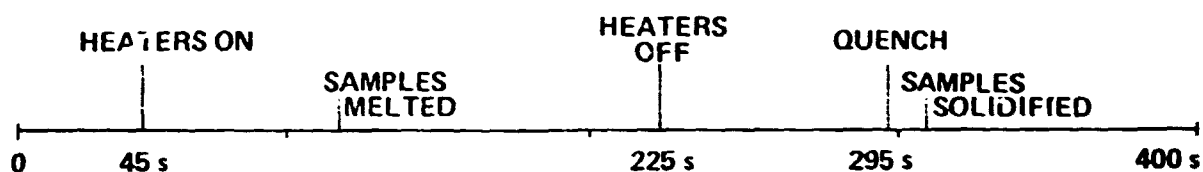


Figure 7. Experiments 74-18/2 and 74-18/3 timeline.

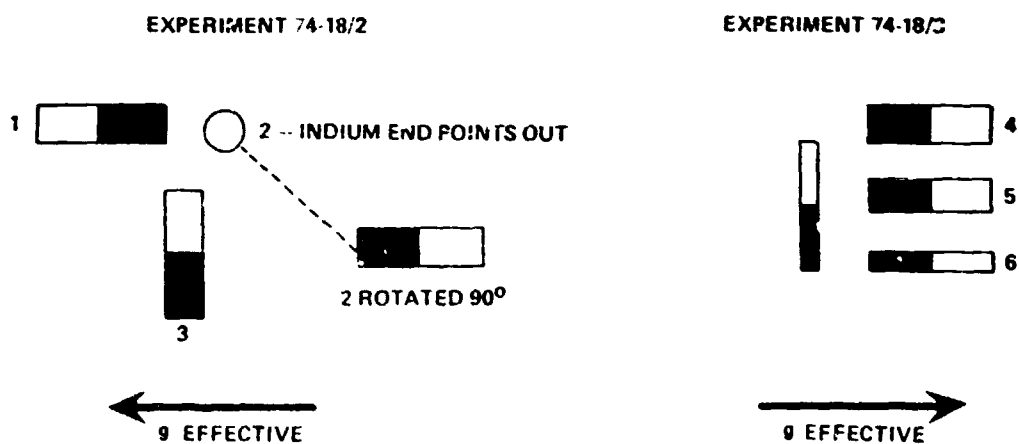


Figure 8. Acceleration directions for SPAR III samples.

function gradient (Fig. 9). The solution to this problem is not available. There exist analytical solutions for a situation which can provide a model for the system of interest, however. If we approximate this system with a two-dimensional (rectangular) model with a linear density gradient, we can apply the nonlinear analysis of Cormach, Leal, and Inberger [3]. These results are used to compute flow velocities in the neighborhood of the original interface and parallel to the cylinder axis of the sample. If we assume that the detectable interface motions (interface velocity times experiment duration) is on the order of the thickness of the diffusion region (approximately 0.2 cm), we obtain a plot of interface motion as a function of acceleration levels for the various sample sizes. These are shown in Figure 10 where it may be noted that an acceleration level sufficient to cause an observable interface motion will be a few times 10^{-5} g or greater.

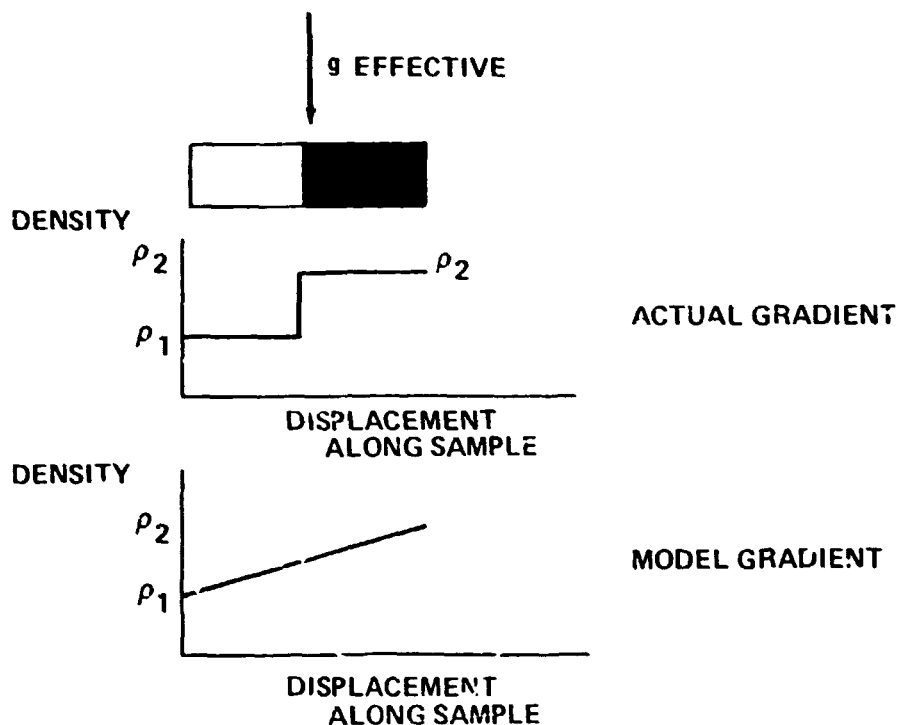


Figure 9. Density gradient, actual and model, samples 2, 3, 7.

The orientation of samples 1, 4, 5, and 6 (Fig. 8) with respect to a radially outward directed force presents a different fluid dynamical problem. These samples are cylindrical fluid systems with a heavier liquid overlaying a lighter liquid in a vertically downward directed force field. Again, we have a problem that is not tractable analytically. Some insight into the problem can be

SAMPLE LONGITUDINAL AXIS \perp g VECTOR

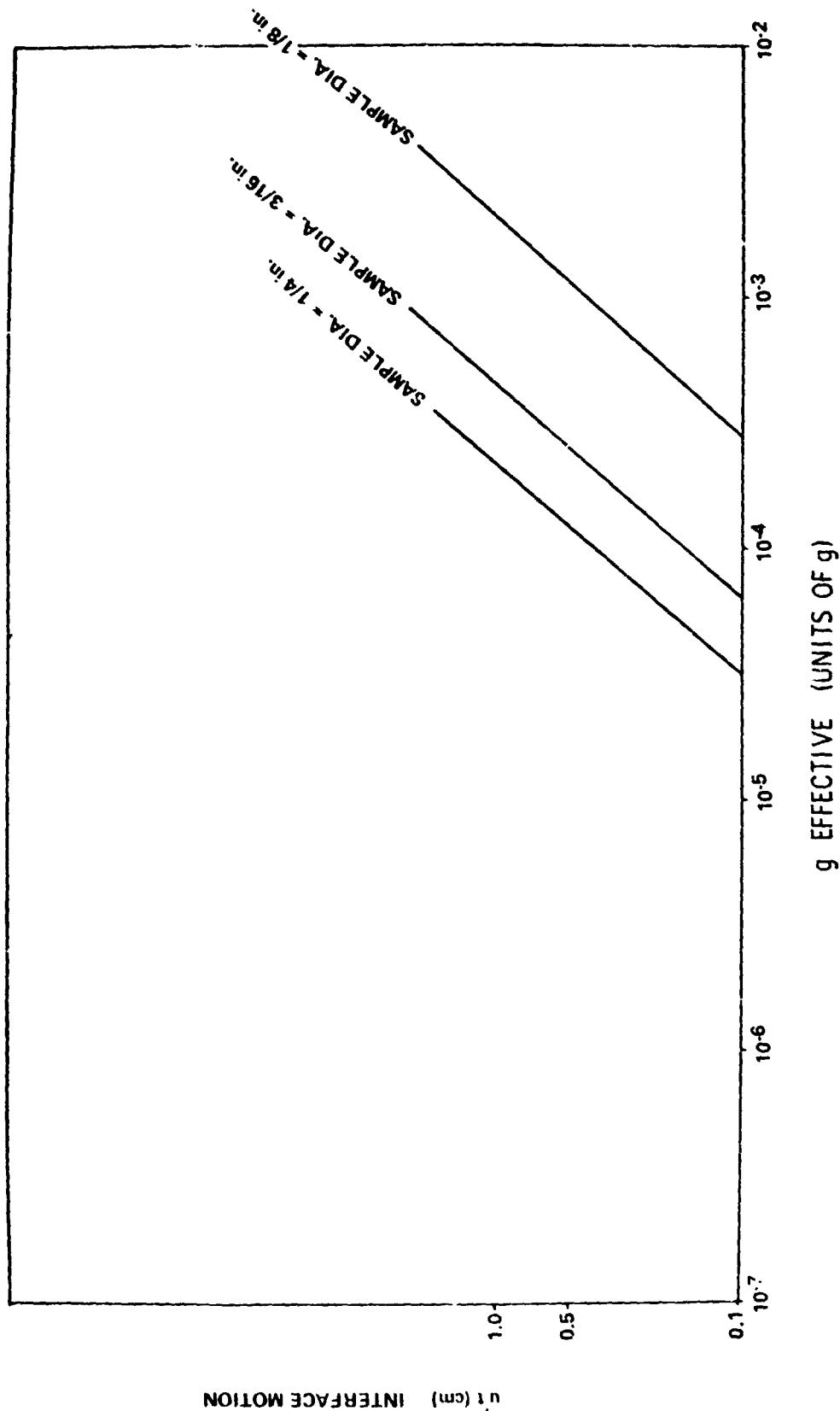


Figure 10. Interface motion plotted as a function of acceleration levels for the three sample sizes.

gained through, first, the application of Rayleigh-Taylor instability theory [4] and then by considering nonlinear effects. The system modeled here is in a state of unstable equilibrium until some perturbation initiates flow. In Reference 2, it was determined that the most unstable mode corresponded to an antisymmetric flow relative to a plane containing the cylinder axis. In addition, the growth rate for such a disturbance was found by applying results from Chandrasekhar [4] and from inviscid theory for a finite cylinder. For a sample 2.2 cm long and 0.6 cm in diameter, the e-fold time for disturbance growth was 50 s for $g_{\text{eff}} = 10^{-5} g$ and 300 s for $g_{\text{eff}} = 10^{-6} g$. This indicates that disturbance can grow significantly at $10^{-5} g$ for this configuration in a time on the order of our experiment duration.

Once the instability has developed, the problem becomes nonlinear and a solution for the problem does not exist. One may turn to results of experimental work by Taylor [5] and Wooding [6] to provide insight into expected results. These authors found that for long capillary tubes containing a more dense liquid overlaying a lighter liquid, a finger of the denser fluid penetrated a distance into the lighter fluid in an antisymmetric fashion initially. After a period of time a stable situation was reached (Fig. 11) which was characterized by the more dense fluid still overlaying the lighter, but with a region between them having a linear density gradient. The bulk of the flow was observed to occur rapidly with respect to total experiment duration with the final state achieved by diffusion. This final state is characterized by a critical Rayleigh number for a linear density gradient in an infinite cylinder (essentially the same results were obtained in Reference 7 for a finite cylinder):

$$Ra (\text{critical}) = g_{\text{eff}} \frac{\Delta \rho a^4}{2 \rho \delta \nu D} = 67.94$$

where

$Ra (\text{critical})$ = the critical Rayleigh number

ρ = the density

a = the sample radius

δ = the penetration distance of the heavier material into the lighter

ν = the kinematic viscosity

D = the diffusion coefficient.

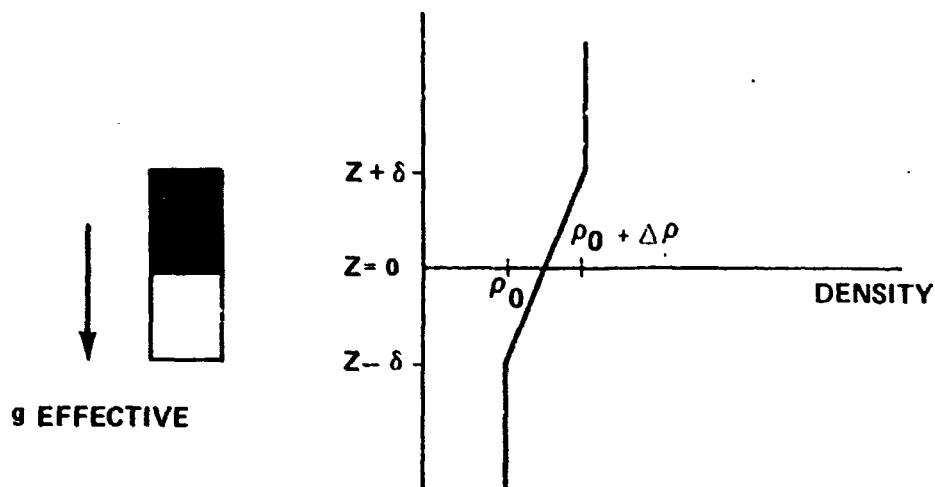


Figure 11. Model for predicted final state density gradient.

This penetration depth is plotted as a function of g_{eff} for the three sample diameters in Figure 12.

To summarize the expected sample flow behavior then, we would expect, given a radially directed residual acceleration with a magnitude of between $10^{-6} g$ and $10^{-5} g$, no measurable flows in samples 2, 3, 6, and 7. We would expect measurable flows in samples 1, 4, and 5.

RESULTS OF EXPERIMENTS 74-18/2 AND 74-18/3

The expected results described serve to explain the behavior of the SPAR I experiment as well as to provide a prediction of the behavior of the SPAR III samples. After opening the experiment cartridges and subjecting the samples to visual observation and X-ray radiography, we can construct the sketch of results shown in Figure 13. The experiment performed well in an engineering sense in that all samples melted and were quenched at the proper times. Samples 4 and 5, however, did not have good joints between the In and In-Pb sections so that no flow could have occurred in these samples. Sample 1 experienced flow as expected and by an amount consistent with a radially directed acceleration with a magnitude in the $10^{-6} g$ to $10^{-5} g$ range (approximately $5 \times 10^{-6} g$). Samples 2, 3, 6, and 7 experience no flow as expected for radial acceleration of that magnitude. In summary, the SPAR III results were predicted by the considerations used to fully explain the SPAR I sample results.

SAMPLE LONGITUDINAL AXIS II g VECTOR

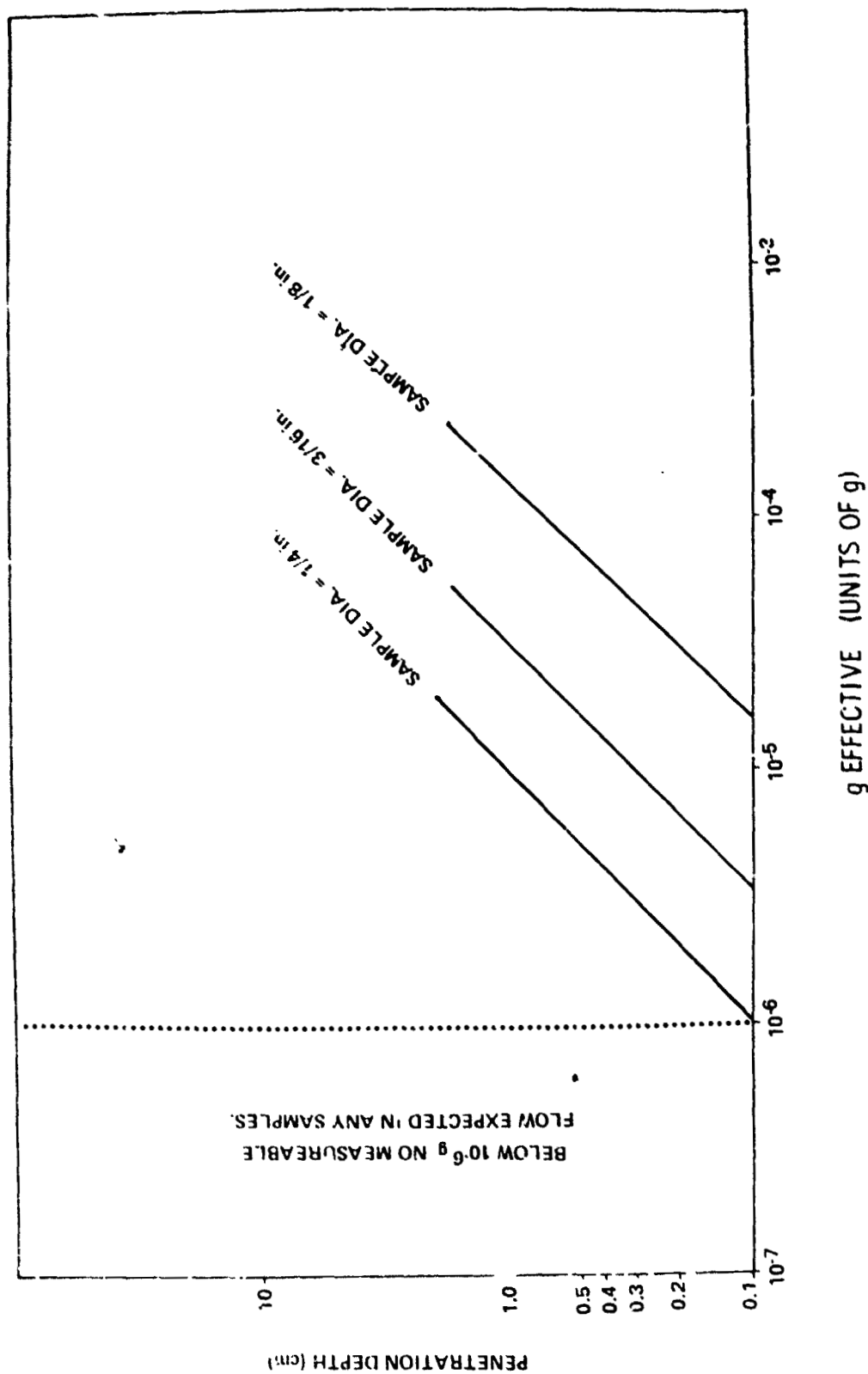
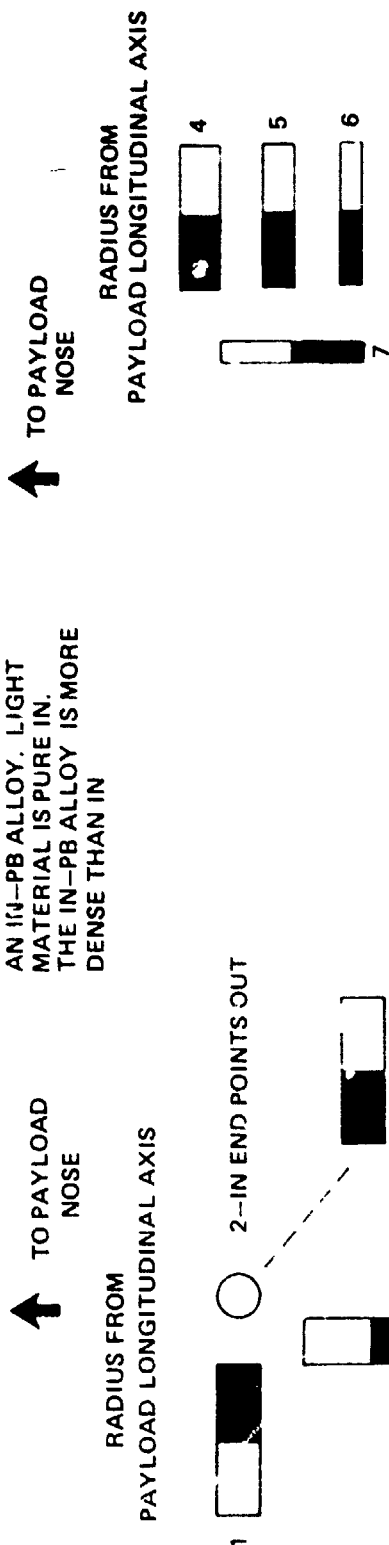


Figure 12. Penetration depth plotted as a function of g_{eff} for the three sample diameters.

74-18/2

74-18/3

(PREFLIGHT)
SHADED MATERIAL IS
AN IN-PB ALLOY. LIGHT
MATERIAL IS PURE IN.
THE IN-PB ALLOY IS MORE
DENSE THAN IN.



(POST-FLIGHT)
FROM RADIOGRAPHS

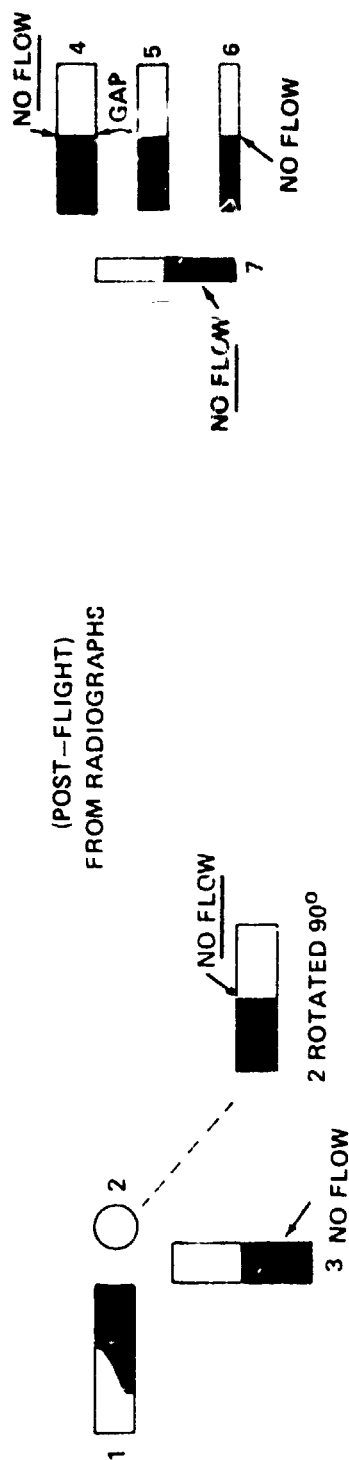


Figure 13. SPAR III liquid mixing experiment results.

We can conclude that these theoretical considerations constitute a predictive capability (in an order of magnitude sense) for these sample systems, and further that the flows observed here were induced by residual accelerations in the 10^{-6} g to 10^{-5} g range and directed radially outward from the payload cylinder axis.

REFERENCES

1. Hansen, M.: Constitution of Binary Alloys. McGraw-Hill. New York, 1958, p. 854.
2. Schaffer, C. F. and Fichtl, G. H.: SPAR I Liquid Mixing Experiment. AIAA 15th Aerospace Sciences Meeting, Paper No. 77-119, Los Angeles, California, January 24-26, 1977.
3. Cormack, P. E., Leal, L. G., and Inberger, J.: Natural Convection in a Shallow Cavity with Differentially Heated End Walls. Part 1, Asymptotic Theory. J. Fluid Mech., vol. 65, part 2, 1974, pp. 209-229.
4. Chandrasekhar, S.: Hydrodynamic and Hydromagnetic Stability. Oxford University Press, London, 1961, pp. 428-477.
5. Taylor, G. I.: Diffusion and Mass Transport in Tubes. Proc. Phys. Soc. LXVII, vol. 12-B, 1955.
6. Wooding, R. A.: The Stability of a Viscous Liquid in a Vertical Tube Containing Porous Material. Proc. Roy. Soc. A., vol. 252, 1969.
7. Verhoeven, J. D.: Convection Effects in the Capillary Reservoir Technique for Measuring Liquid Metal Diffusion Coefficient. Trans. Met. Soc. AIME, vol. 242, September 1968, pp. 1937-1941.

CHAPTER IV

INTERACTION OF BUBBLES WITH SOLIDIFICATION INTERFACES

Experiment 74-36

By

John M. Papazian*

Grumman Aerospace Corporation

and

William R. Wilcox**

Clarkson College of Technology

* Research Department, Materials and Structural Mechanics

** Department of Chemical Engineering

ABSTRACT

The formation of voids and the behavior of bubbles were studied during low-g solidification of CBr_4 . With the exception of a fourfold increase of the temperature gradient to $20^\circ\text{C}/\text{cm}$ and the use of higher purity material for one of the four specimens, this experiment was identical to the experiment previously performed on SPAR I. In this experiment we observed cylindrical rather than spherical voids in the commercial purity material, irrespective of gravitational forces (1 g versus 10^{-4} g). The high purity material, however, shifted from cylindrical to spherical voids in the low-g experiment. No large scale thermal migration of bubbles, bubble pushing by the solid-liquid interface, or bubble detachment from the interface were observed. A unique bubble motion-fluid flow event occurred in one specimen: a large bubble moved downward and pushed several neighboring small bubbles. These observations and plans for the final flight experiment are discussed.

INTRODUCTION

This report presents the results of the SPAR III flight of Experiment 74-36; this flight was the second in a series of three planned for the program. The overall objectives of this study are to investigate the effect of gravity on the interaction of bubbles with solidification interfaces and to generate preliminary data on the thermal migration of bubbles. Specific objectives for this flight were to repeat the first flight experiment with a higher temperature gradient and to compare the behavior of high purity zone refined CBr_4 to that of commercial purity material. The experimental apparatus functioned correctly once again, and the results of analysis of the flight film and low-g processed specimens are described herein.

EXPERIMENTAL PROCEDURE

Apparatus

The same apparatus was employed for this flight as had been used on flight I. Details of the design and construction are given in the SPAR I final report [1]. The apparatus was modified slightly to achieve a higher temperature gradient while preserving the same freezing rate. This modification involved replacing the aluminum specimen holder heater block with a slightly shorter but otherwise identical unit fabricated from stainless steel. The shorter length and lower thermal conductivity of the stainless steel allowed a fourfold increase in the temperature gradient to $20^\circ\text{C}/\text{cm}$. The maximum temperature (at the top block) was purposely kept low to minimize the length of the liquid zone at launch and suppress decomposition of the CBr_4 .

Specimen Preparation

Filling of the sample tubes with CBr_4 was effected in a manner identical to that described in Reference 1. For this flight all of the specimens were saturated with nitrogen. Two of the four specimens were commercial purity (CP) CBr_4 and the remaining two were high purity CBr_4 . The high purity (ZR) material was prepared by zone refining. The zone refining was carried out at Clarkson College of Technology in a modified Fisher Scientific Co. apparatus. Purification by zone refining reduced the relative optical absorptivity of a 0.76 M solution of CBr_4 in CCl_4 at 417 nm from 0.064 to 0.009. Bromine is

thought to be the impurity responsible for this coloration; its concentration was substantially reduced by zone refining. The other major residual impurity was bromoform, its concentration was monitored by gas chromatography. Complete details of the purification procedures and results are given in Reference 2. The CP specimens were installed in positions A and B and the ZR specimens in C and D.

Experimental Sequence

The intended sequence of operations for this experiment was:

$t_0 - 45 \text{ min}$	heater on
$t_0 - 4 \text{ min}$	heater off
t_0	launch
$t_0 + 100 \text{ s}$	camera starts
$t_0 + 330 \text{ s}$	camera stops.

The actual sequence followed this plan with the exception of a 16 min hold which occurred at $t_0 - 13 \text{ s}$. During the hold the heaters were reactivated, the count was reset to $t_0 - 15 \text{ min}$, and the normal sequence of operation followed. We chose to begin cooling the sample before launch because ground base experiments had shown that several minutes were required for a stable cooling rate to be established after the heaters were shut off.

RESULTS

Initial Observations

During the rocket flight the apparatus functioned perfectly and the experiment was performed according to plan. The telemetered data show that the camera began operating at $t_0 + 100 \text{ s}$ and took pictures at a rate of 1.08 frames/s.

A two part 16 mm movie was made from the 35 mm \times 226 exposure flight film. The first part was step printed with each original frame repeated eight times.

The second part was printed one for one. Therefore, when projected at 24 frames/s, the movie film shows the experiment speeded up by factors of 3 and 24, respectively. A copy of this film has been submitted to the SPAR program office at MSFC.

Growth and Morphology of Voids

Figure 1 shows the appearance of the specimens at 101 s after liftoff. Payload de-spin occurred at approximately 65 s and all accelerations were below $10^{-3}g$ at 78 s. Between 85 and 338 s no accelerations greater than $10^{-4}g$ were present. Figures 2, 3, and 4 show how solidification proceeded in specimens B, C, and D during the low-g interval. The figures show that in specimens B and C numerous cylindrical voids developed and grew. The growth direction was upward and sharply inclined toward the center of the specimen. The locus of the inner ends of the voids defines the solid-liquid interface; this appears to have been roughly hemispherical and concave towards the liquid. Voids nucleated repeatedly, apparently near the periphery of the sample. Figure 5 is a transmission optical micrograph of specimen C and shows that the cylindrical voids have uneven surfaces and usually begin at a large (approximately 0.05 to 0.1 mm diameter) faceted, roughly spherical void. It is also seen that many small spherical voids are present which did not give rise to cylindrical voids. From stereoscopic observation it can be seen that the voids are totally enclosed by CBr_4 . They are always situated at a small distance (approximately 0.1 mm) in from the outer (cylindrical) surface of the sample. Figure 6 is a micrograph of specimen A showing the overall distribution and morphology of the voids as previously described. Specimens A, B, and C all showed similar void morphologies.

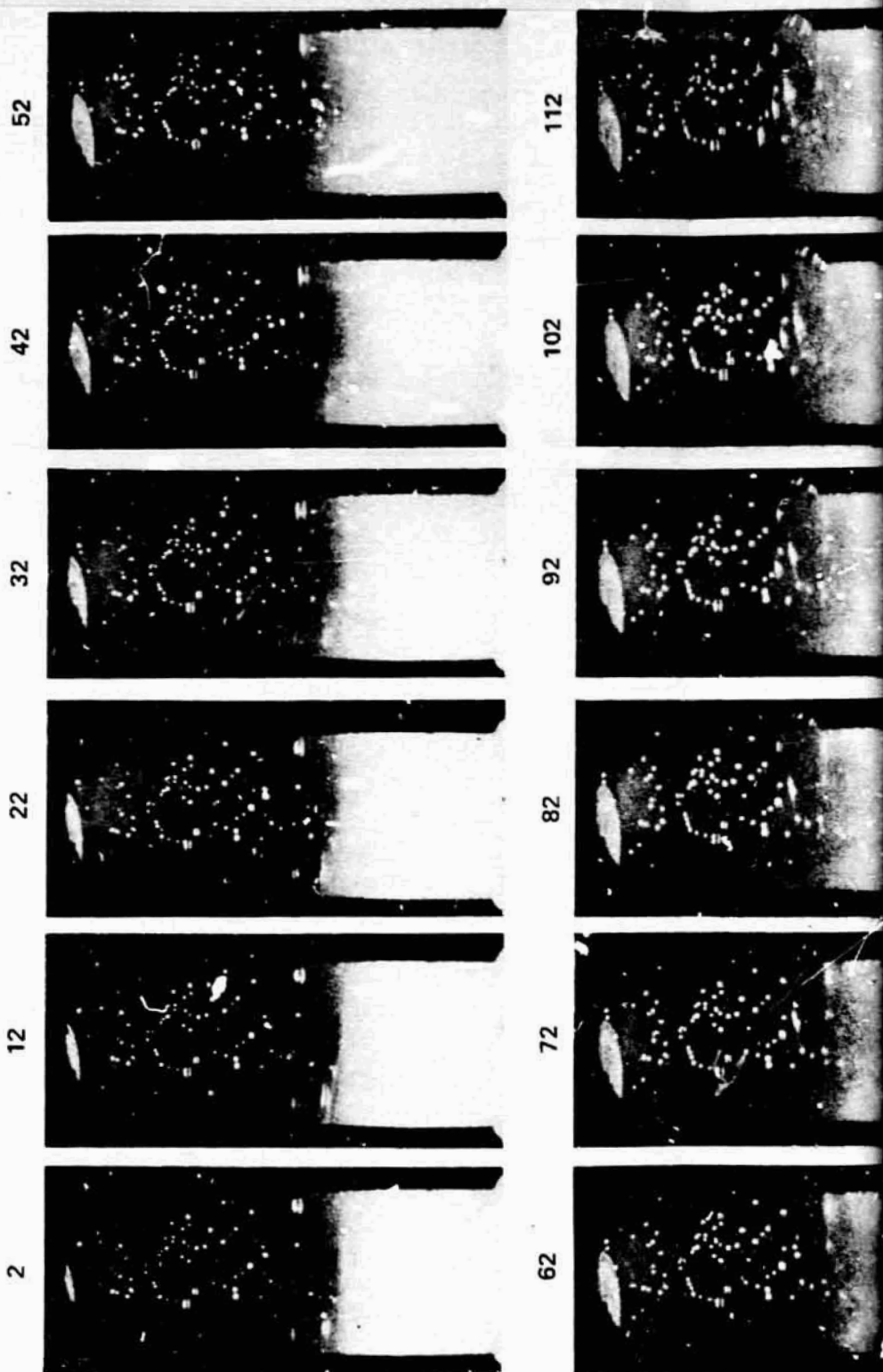
The fourth specimen, D, does not show the same inclined cylindrical void morphology (Fig. 4). From the flight photographs, it is difficult to decide on the number and shape of these voids. It seems, however, that some large voids were grown in and that they are generally of a spherical morphology. They are much less distinct than the spherical voids observed in flight I. An optical micrograph of specimen D is shown in Figure 7; there are indications of spherical voids in the flight grown portion of the specimen. It is also evident in Figure 1 that at $t = 101$ s the interface of specimen D is more planar and more distinct than the interface of the other three specimens. Specimens A, B, and C had a more extensive mushy zone than specimen D.



Figure 1. Appearance of the specimens at 101 s after liftoff. The specimens are designated A through D from left to right. Vertical fiducial grooves in the heat leveler block are spaced 10 mm center to center.

FOLDOUT FRAME

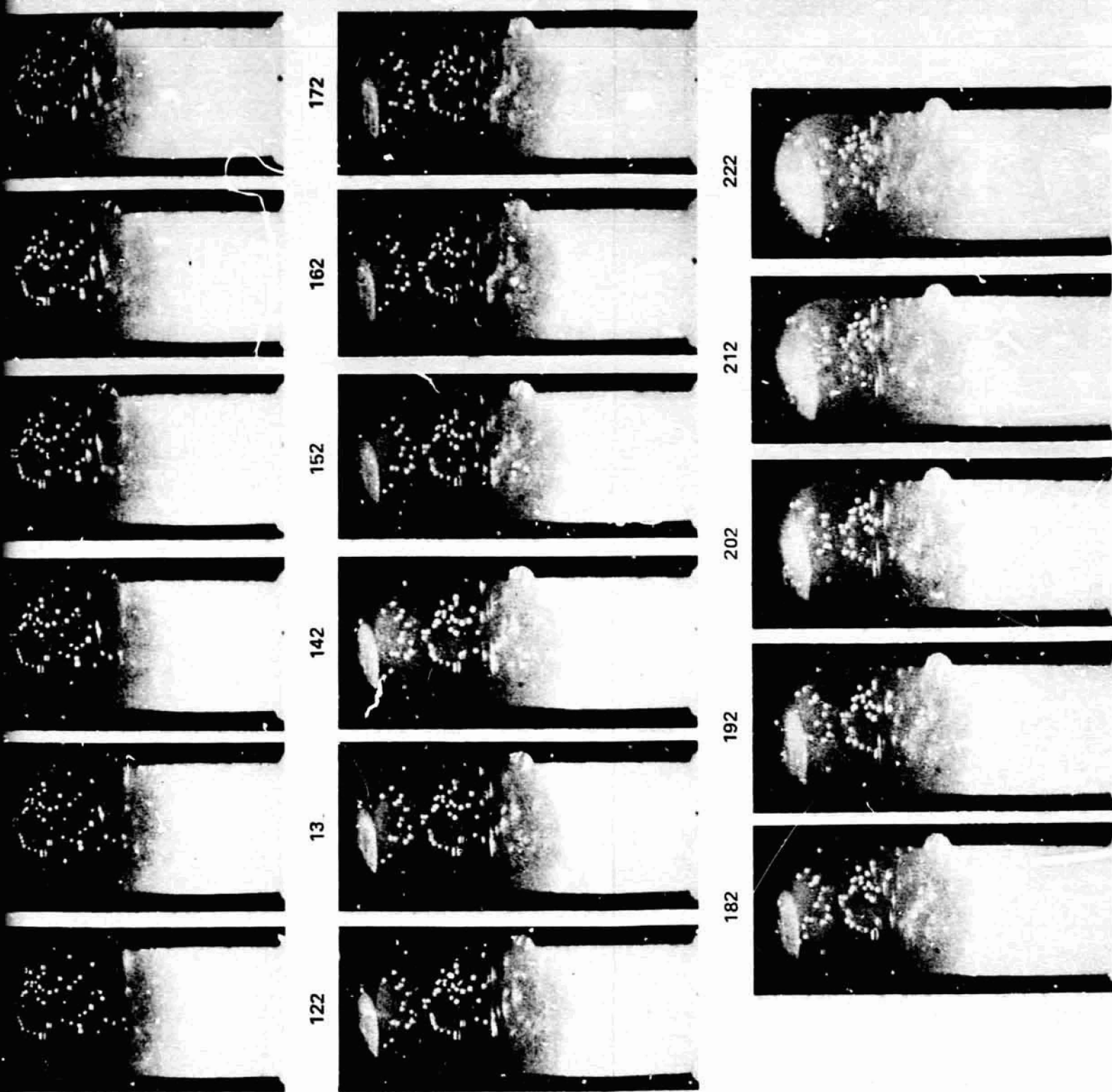
TYPICAL MONTAGE, SPECIMEN B



ORIGINAL PAGE IS
OF POOR QUALITY

Figure 2. Montage photograph
The frame numbers
liftoff is equal

FOLDOUT FRAME 2



Montage photograph of the growth of specimen B during SPAR III. frame numbers are shown above each view; the time since liftoff is equal to the frame number plus 100 s.

FOLDOUT FRAME

TYPICAL MONTAGE, SPECIMEN C

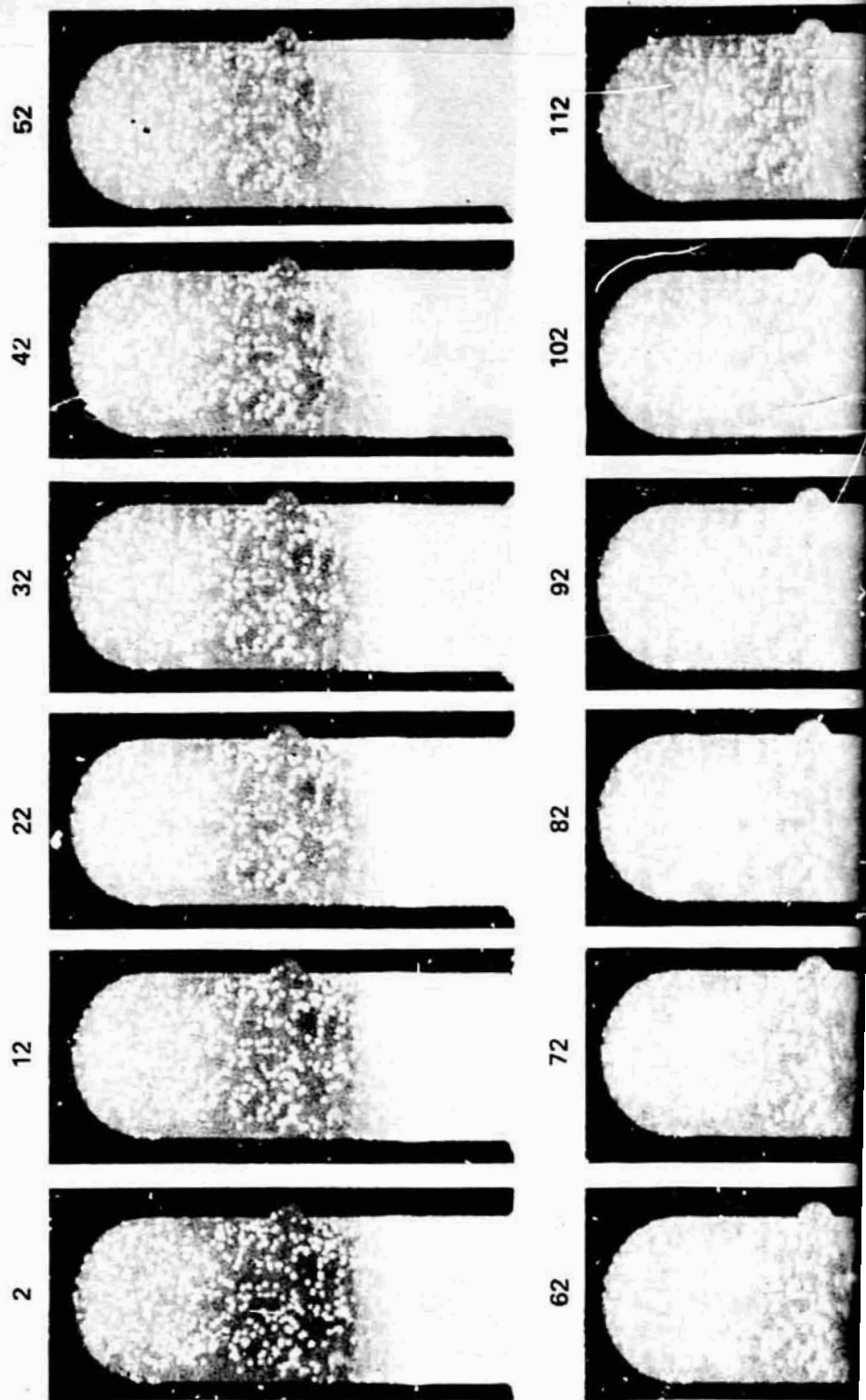
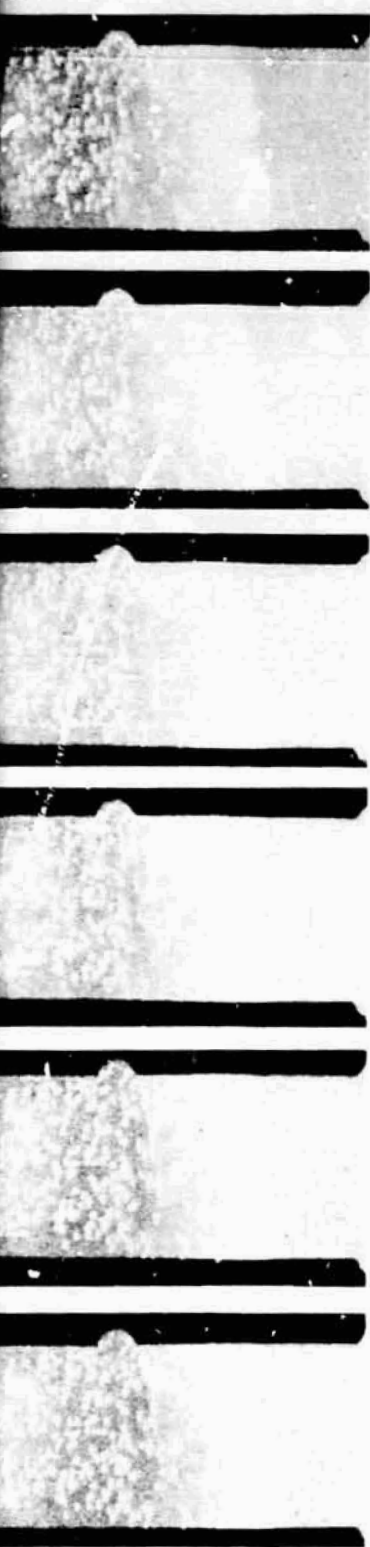


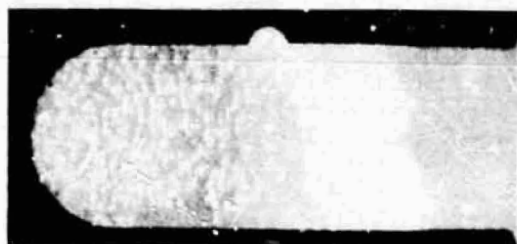
Figure 3. Montage photo

ORIGINAL PAGE IS
OF POOR QUALITY

FOLDOUT FRAME *2*



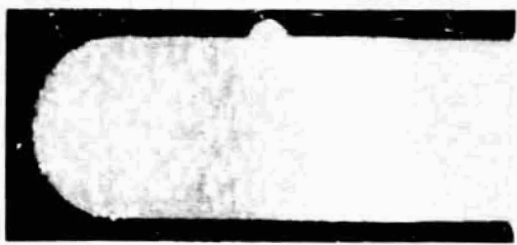
172



162



152



142



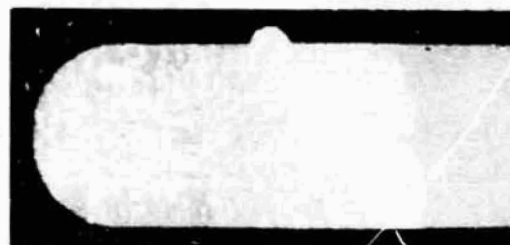
132



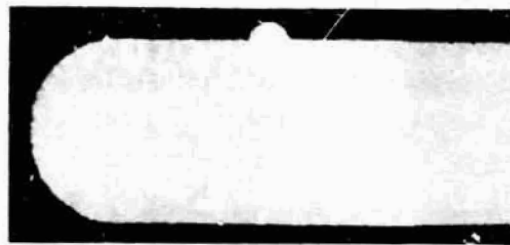
122



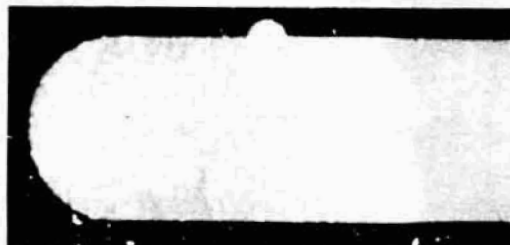
222



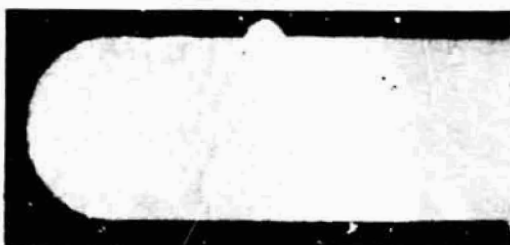
212



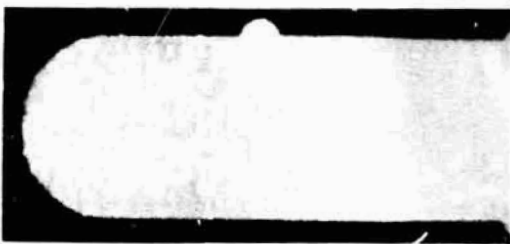
202



192



182

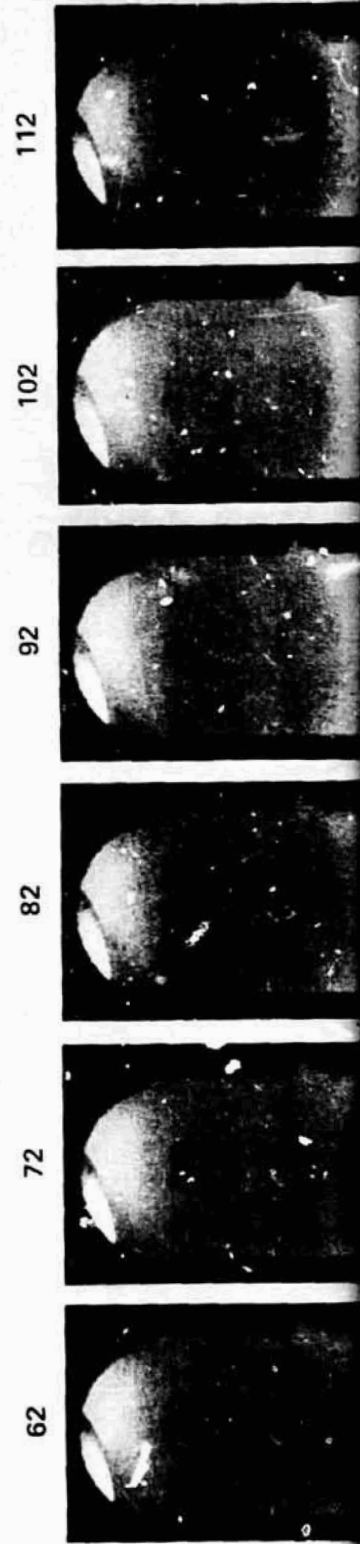
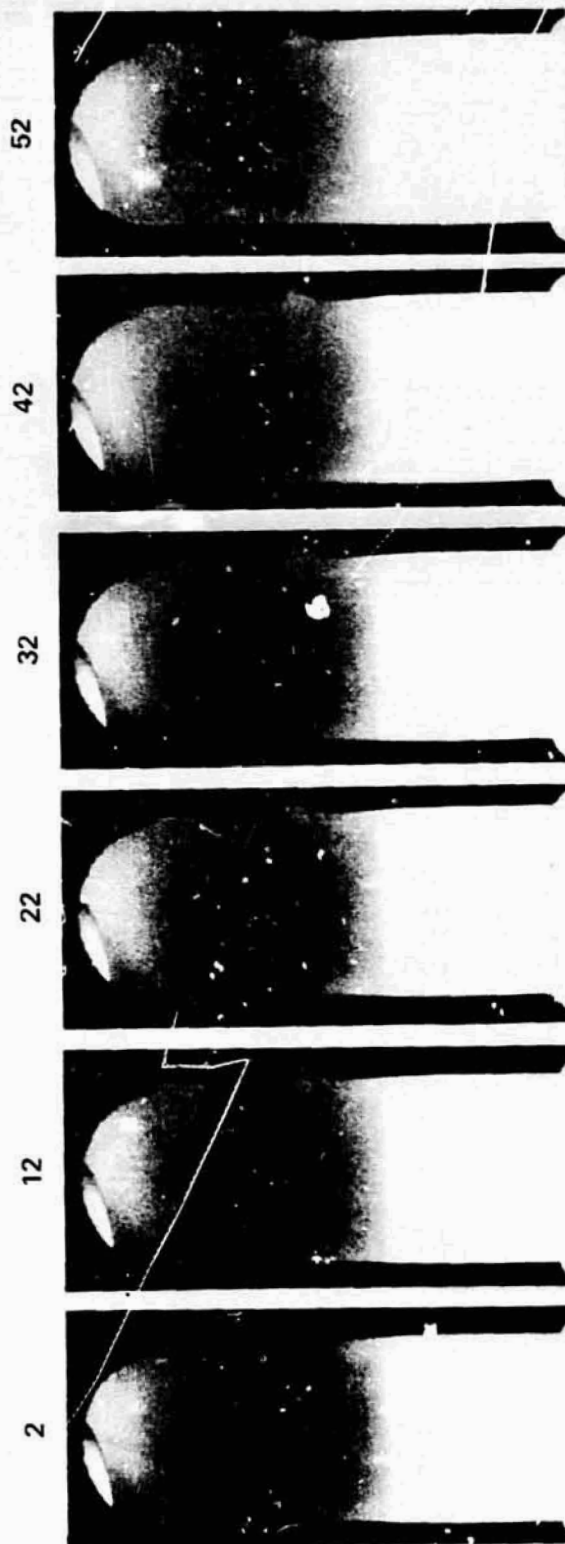


Montage photograph of the growth of specimen C during SPAR III.
Same conditions as Figure 2.

PRECEDING PAGE BLANK NOT FILMED

FOLLOUT FRAME

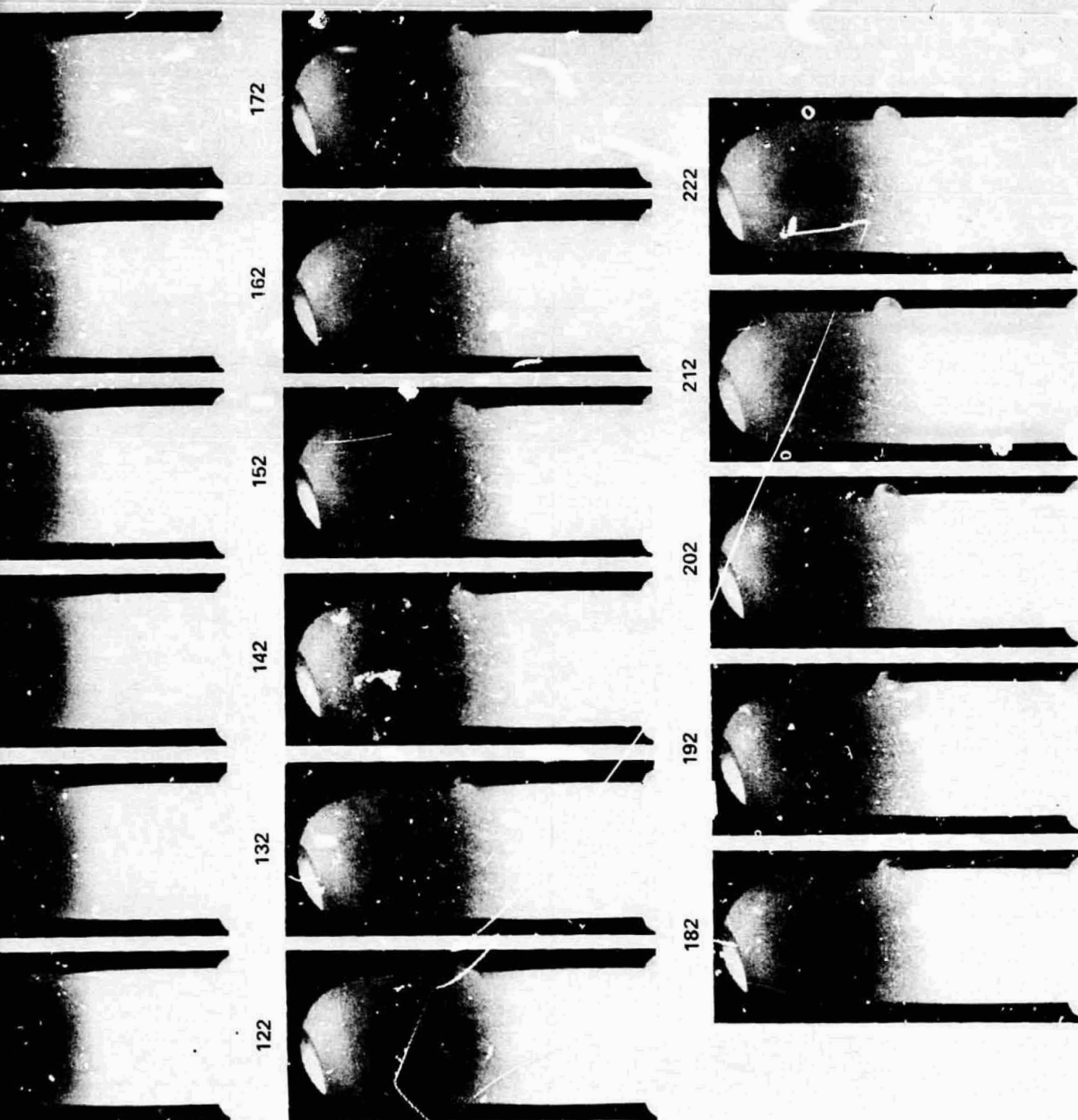
TYPICAL MONTAGE, SPECIMEN D



ORIGINAL PAGE IS
OF POOR QUALITY

Figure 4. Montage photo

BOLDOUT FRAME 2



stage photograph of the growth of specimen D during SPAR III.
Same condition as Figure 2.

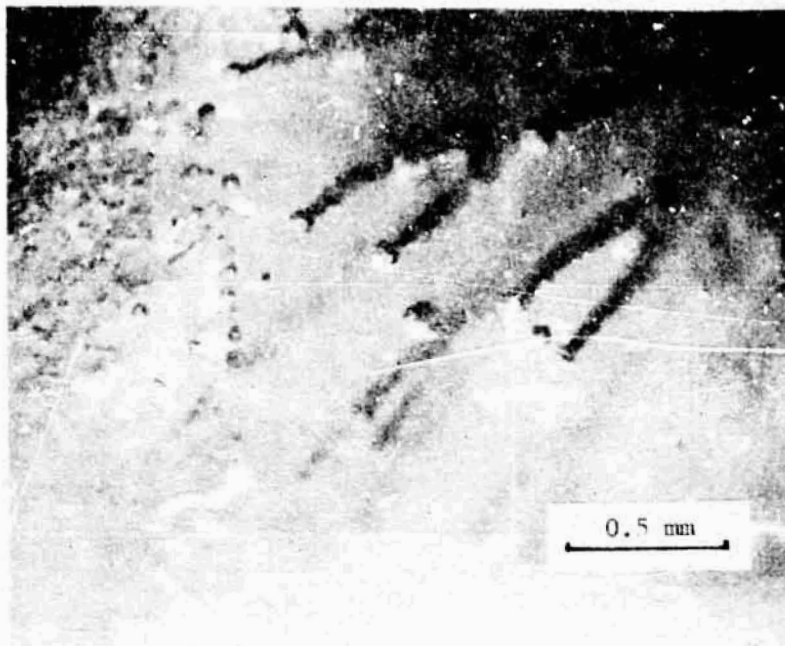


Figure 5. Transmission micrograph of voids in specimen C, SPAR III.
The growth direction is from left to right.

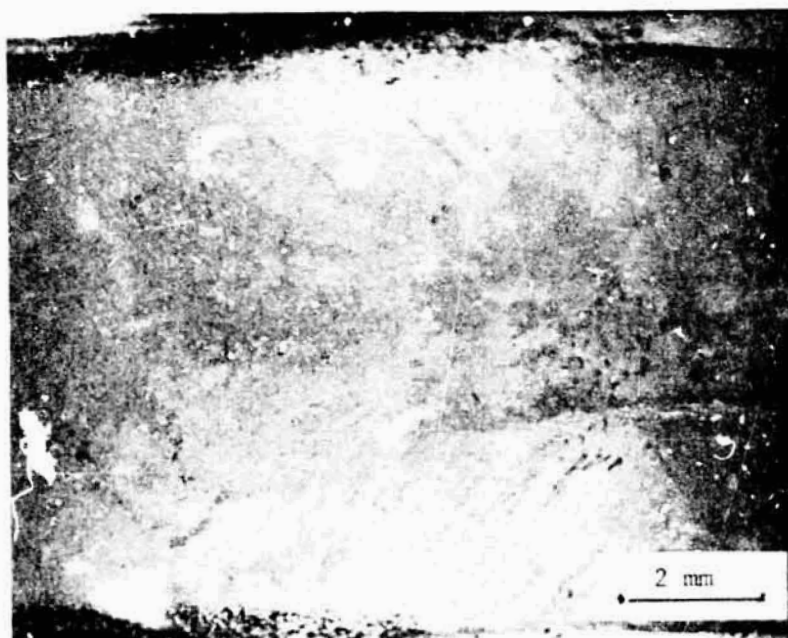


Figure 6. Transmission micrograph of voids in specimen A, SPAR III.
The growth direction is from left to right.

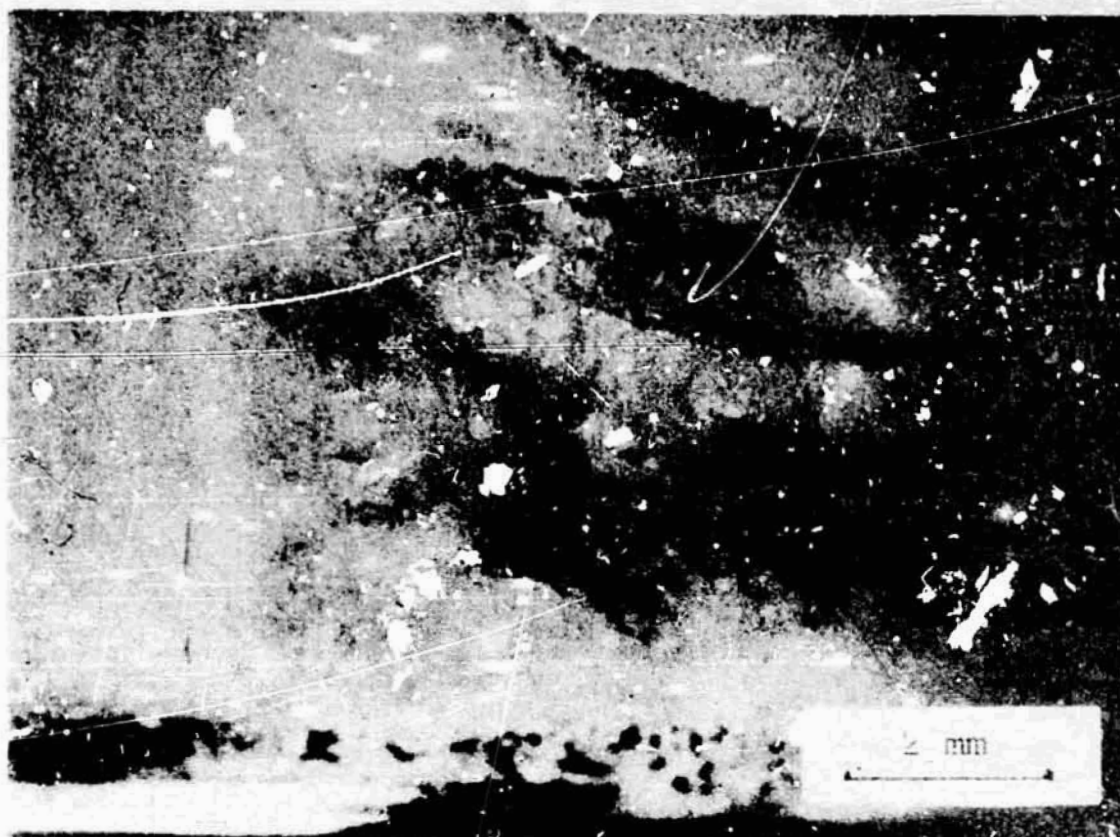


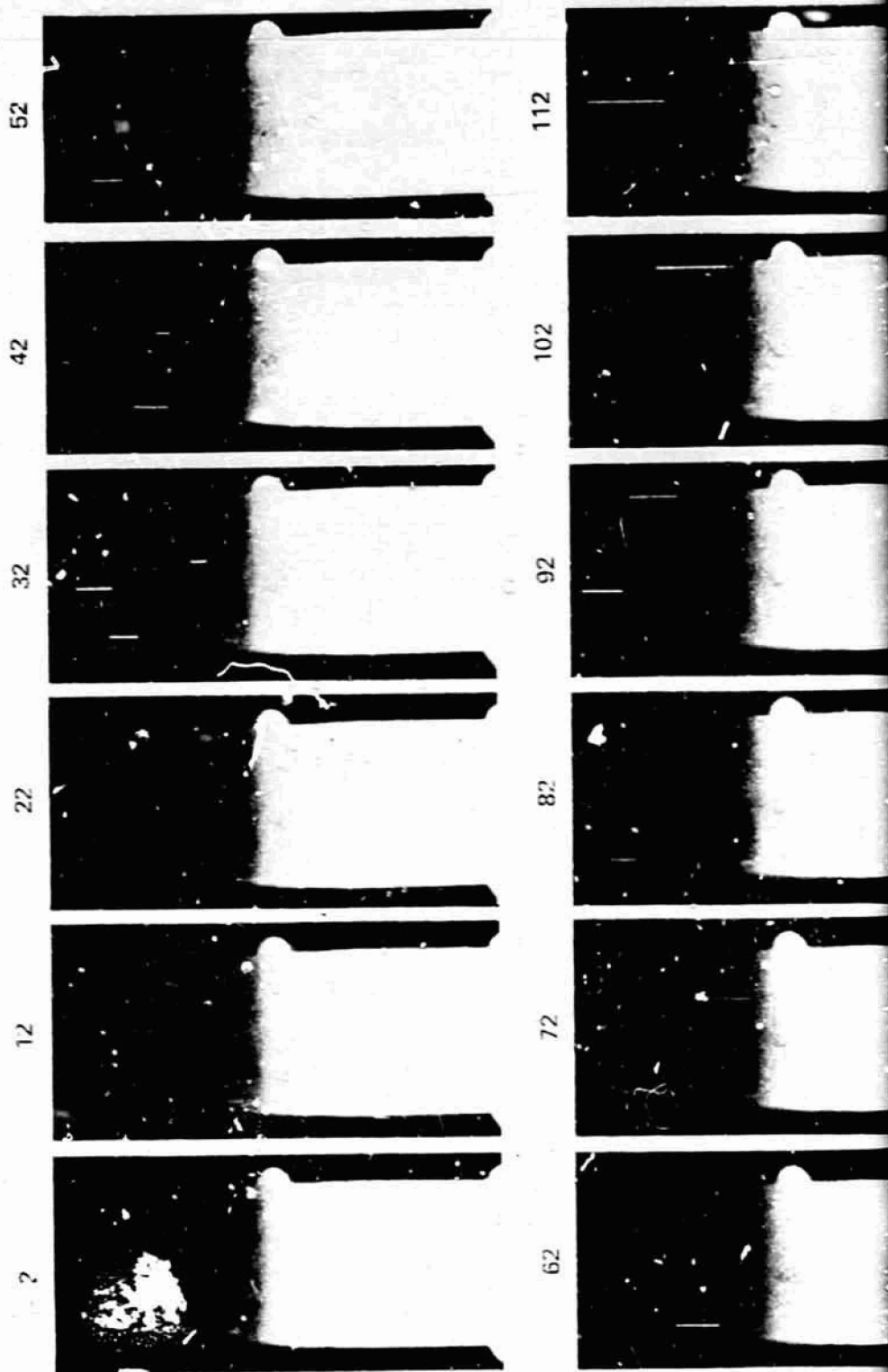
Figure 7. Transmission micrograph of voids in specimen D, SPAR III.
The growth direction is from left to right, the meltback interface
is at the left-hand edge of the picture.

For comparison purposes Figures 8 and 9 show the growth of two specimens during a ground base simulation experiment performed before the flight. Both of these specimens were CP CBr₄. Figures 8 and 9 also show the growth of several voids. Simultaneous optical observations showed that most of the voids were of a cylindrical morphology with the axis of the cylinder parallel to the growth direction (upward).

Small spherical voids were occasionally observed during laboratory simulations, but, in general, cylindrical voids predominated. The number of voids present was generally small. These observations also held true for ZP material. Figures 8 and 9 also show the escape of small bubbles from the solid-liquid interface. The bubbles appear as vertical white lines in the dark, liquid portion of the specimen. The exposure time was 0.25 s, and the bubbles

FOLDOUT FRAME

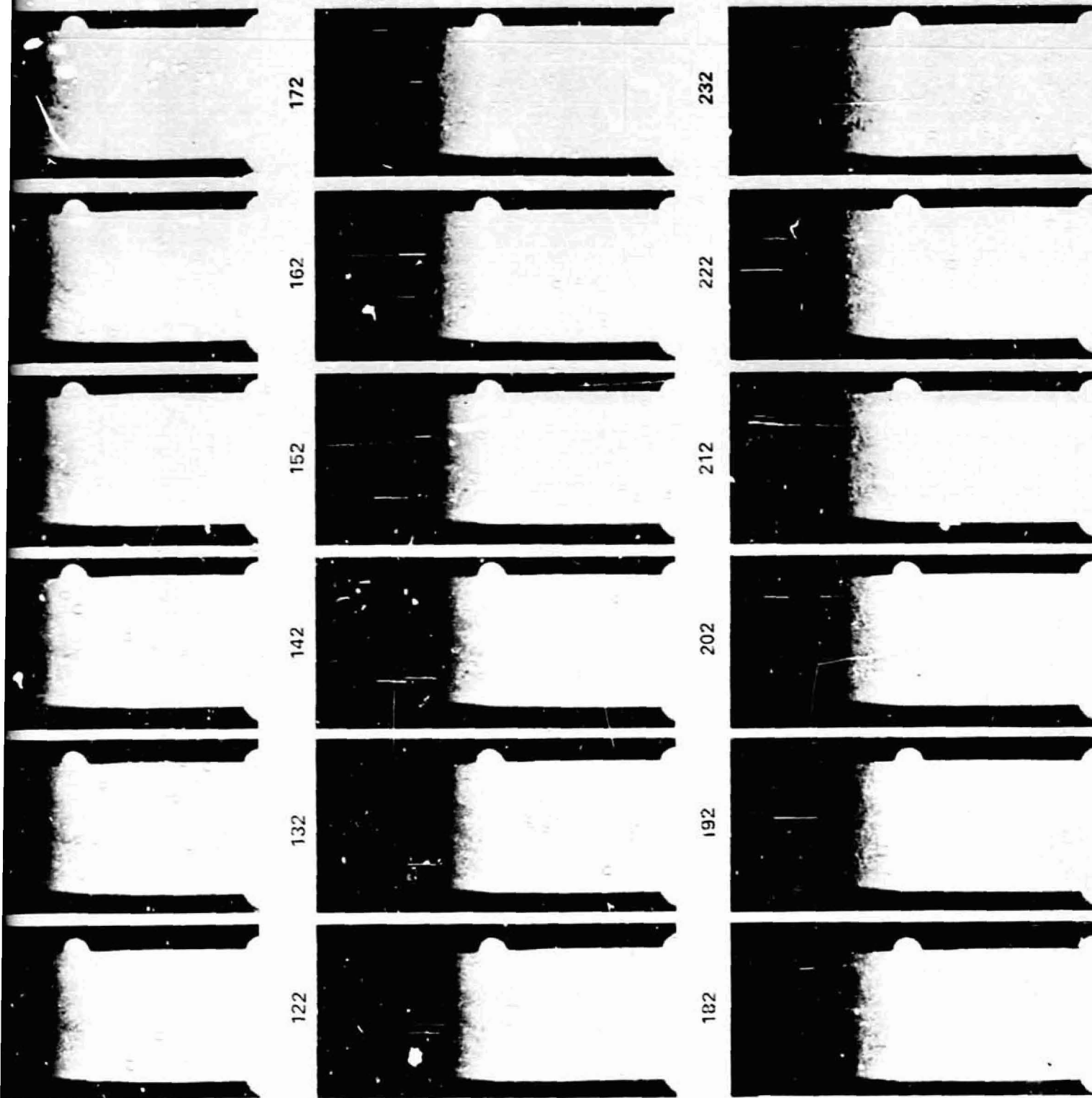
SPECIMEN B, GBS



ORIGINAL PAGE IS
OF POOR QUALITY

Figure 8. Montage photo
experiment. The fra
since liftoff

FOLDOUT FRAME *2*



Montage photograph of specimen B during ground base simulation. The frame numbers are shown above each view; the time since liftoff is equal to the frame number plus 100 s.

ORIGINAL PAGE IS
OF POOR QUALITY

PREVIOUS PAGE BLANK NOT FILMED

FOLDOUT FRAME

SPECIMEN D, GBS

ORIGINAL PAGE IS
OF POOR QUALITY

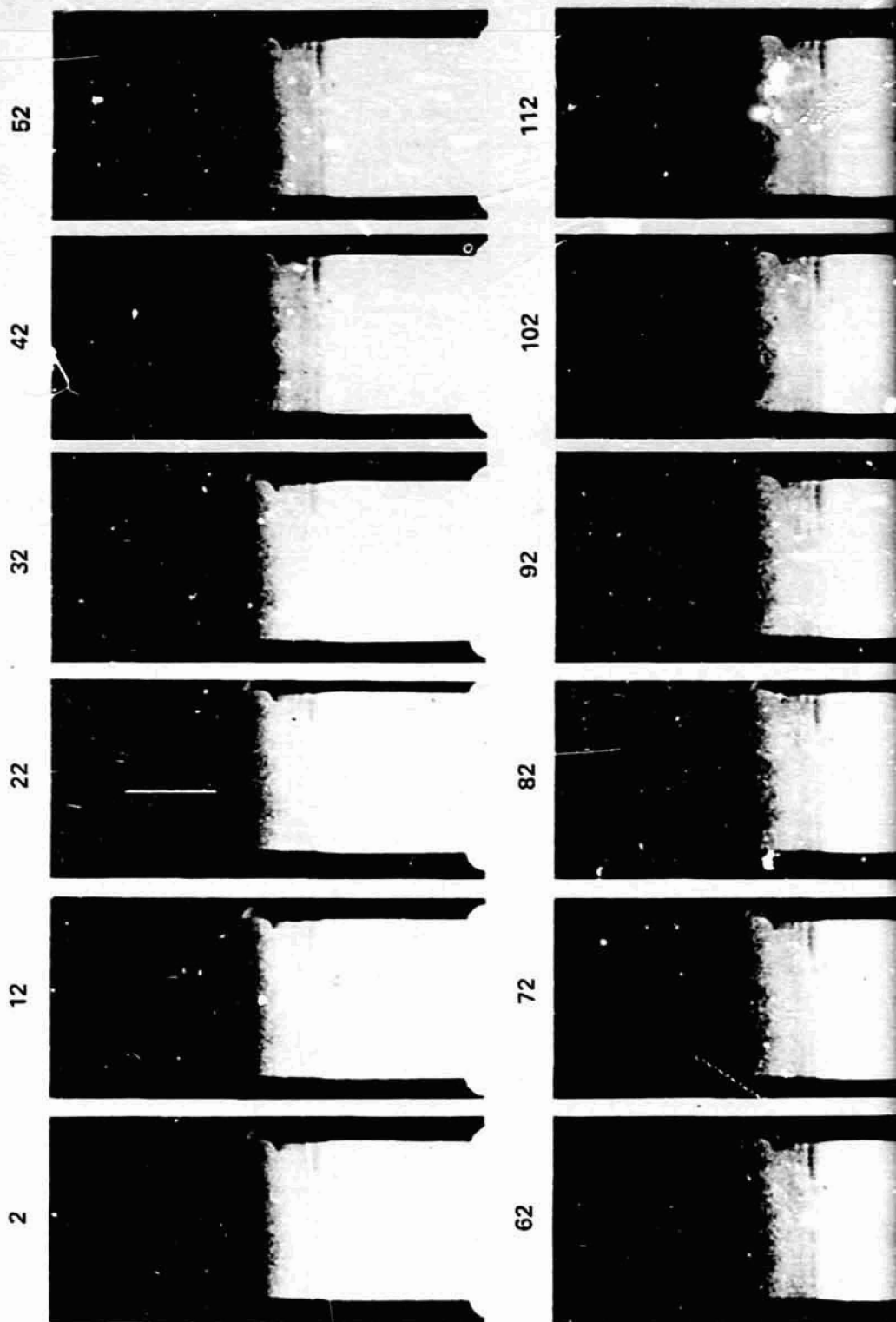


Figure 9. Montage photo
simulation exper

FOLDOUT FRAME 2

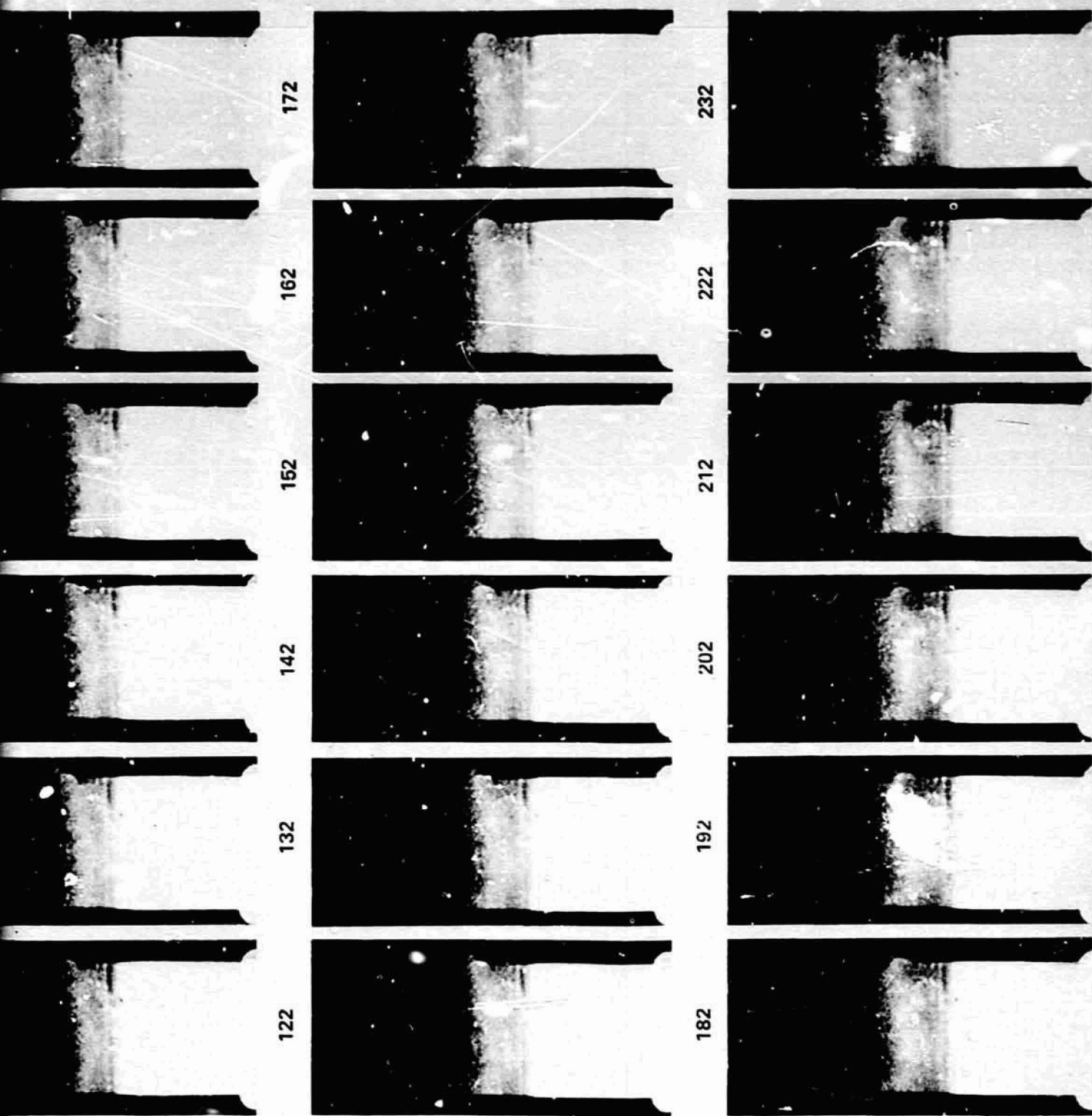


Figure 9. Montage photograph of specimen D during a ground base simulation experiment. Same conditions as Figure 8.

moved rapidly upwards. It was also observed during laboratory experiments that small bubbles often dissolved as they were rising and disappeared before they reached the top of the liquid zone. This was either due to increasing gas solubility with increasing temperature or to nonsaturation of the melt.

Figure 10 shows contact radiographs of the flight and ground base specimens. One can barely see the curved cylindrical voids in the flight specimens. There are no indications of voids in the ground base simulation specimens.

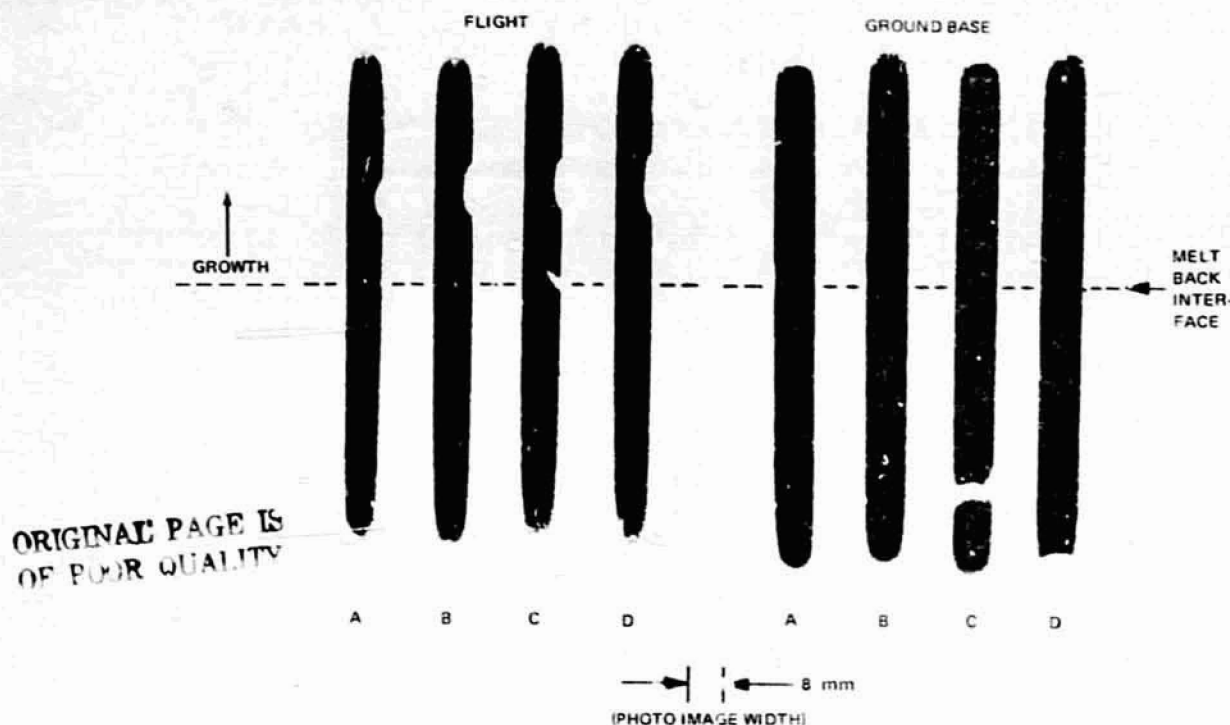


Figure 10. Radiograph of CBr_4 specimen, SPAR III, 90 deg.

Growth Rates

The rate of growth of solid CBr_4 during the experiment was determined from 8×10 in. prints of the flight film. The position of the interface was measured and plotted as a function of time. A straight line was then fit to the data. The slope of this line was taken as the growth rate. Two features were measured, the fastest dendrite tips and the locus of the ends of the voids. Both were measured along the centerline of the sample tube. The results from

SPAR III and representative ground base simulations are listed in Table 1. All of the ground base simulation specimens in the table were CP CBr₄. For flight specimens A and B the voids were sharply inclined to the axis of the tube. Thus, their apparent vertical velocities should be multiplied by a projection factor of approximately $\sqrt{2}$ to get their true velocities. The voids in flight specimen C were also inclined, but several layers nucleated and grew one on top of the other. It is seen, therefore, that the voids and dendrites grew at approximately the same rate in the flight specimen. It is also seen that three of the flight specimens grew approximately twice as rapidly as the laboratory simulation specimens. This effect is probably due to modification of the thermal gradient by rocket spin, as discussed in the following text. For comparison purposes, Table 2 lists average values of the growth rates observed in SPAR I and SPAR III.

TABLE 1. AVERAGE GROWTH RATES ($\mu\text{m/s}$), SPAR III

Specimen	Dendrites	Voids
Flight A	34	18
Flight B	32	18
Flight C	34	23
Flight D	17	5 to 10
GBS A	13	9
GBS B	15	12
GBS C	16	8.5
GBS D	11	9

TABLE 2. GROWTH RATES ($\mu\text{m/s}$), SPAR I AND SPAR III

	Voids/Translucent	Dendrites
SPAR I Flight	14	110
SPAR I GBS	2.5	110
SPAR III Flight	25	33
SPAR III GBS	10	14

Bubble Phenomena

A notable feature of Figure 1 is the presence of small bubbles in the liquid portion of the specimens. There were approximately 400 small (approximately 0.1 mm diameter) bubbles in specimen A, 75 in specimen B, 300 in specimen C, and none in specimen D at the beginning of filming. Also visible toward the top of the viewing slot is the lower portion of a large, approximately 4 mm diameter, bubble in specimens B and D. Examination of Figures 2, 3, and 4 shows that most of the bubbles appear to be stationary throughout the experiment but seem to increase in size. Close examination using transparent overlays and repeated viewing of the 16 mm film confirms that none of the bubbles in A, C, and D moves, but significant bubble motion occurred in specimen B as can be seen in Figure 2. The direction of bubble motion in B is complex, and the motions occurred in two stages. Figure 11 is a schematic representation of the motion of several representative bubbles in specimen B. During the interval between $t_0 + 100$ s and $t_0 + 160$ s the lower edge of the large bubble moved downward by 0.5 mm. The small bubbles in the center of the liquid region also moved downward, but some small bubbles moved upward and others moved sideways. The small bubbles only moved approximately 0.2 mm.

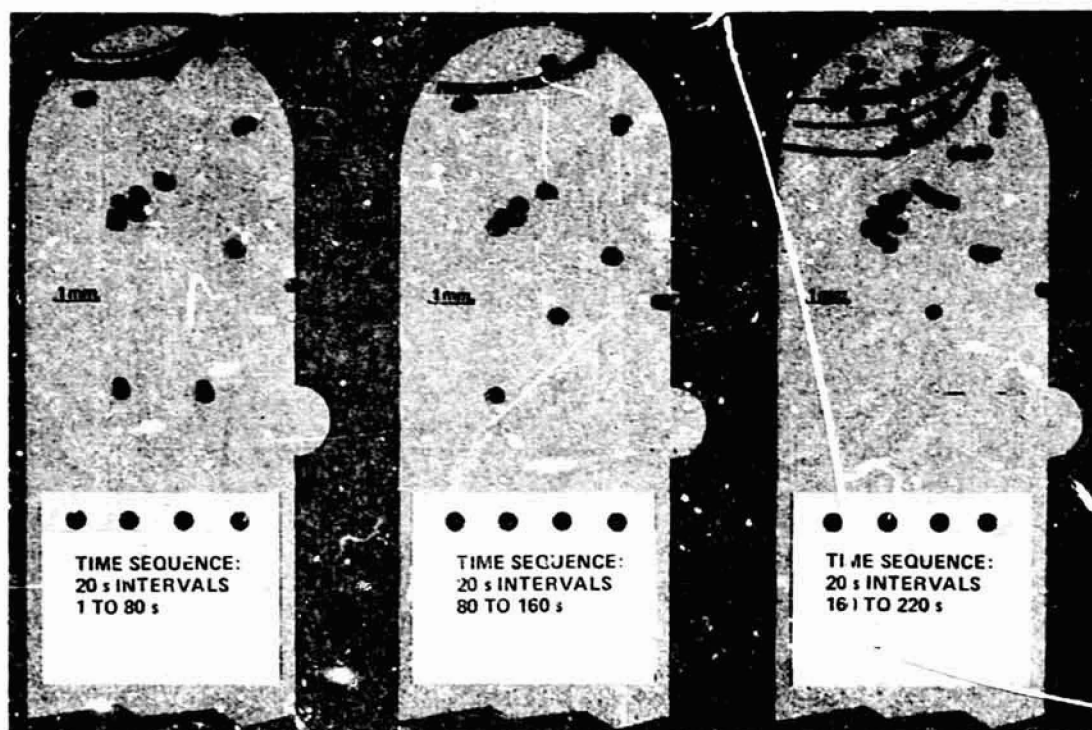


Figure 11. Schematic representation of bubble motion in specimen B, SPAR III.

Almost no bubble motion occurred between $t_0 + 160$ s and $t_0 + 260$ s, but at $t_0 + 260$ s the lower edge of the large bubble began to move downward again.

The small bubbles also moved: those in the center of the field-of-view followed a curved trajectory downward and to the right; those at the top, very near to the large bubble, moved upwards. The large bubble moved 1.3 mm and the small bubbles moved between 0.3 and 1.1 mm. When viewing this motion speeded up by a factor of 24 on the 16 mm film, one has the distinct impression that the small bubbles were swept along in a fluid flow which was driven by the motion of the large bubble.

The diameters of several bubbles in specimen B were measured every tenth frame. Typical results are plotted in Figure 12, with a least squares straight line fit to the data. One bubble did not grow but remained at a constant diameter; in general, however, the bubble diameters increased linearly with time. Bubble diameters were not measured in specimens A and C, but had the same qualitative behavior. This behavior is in contrast to that of SPAR I in which bubbles were observed to disappear during the first 100 s as shown in Figure 13.

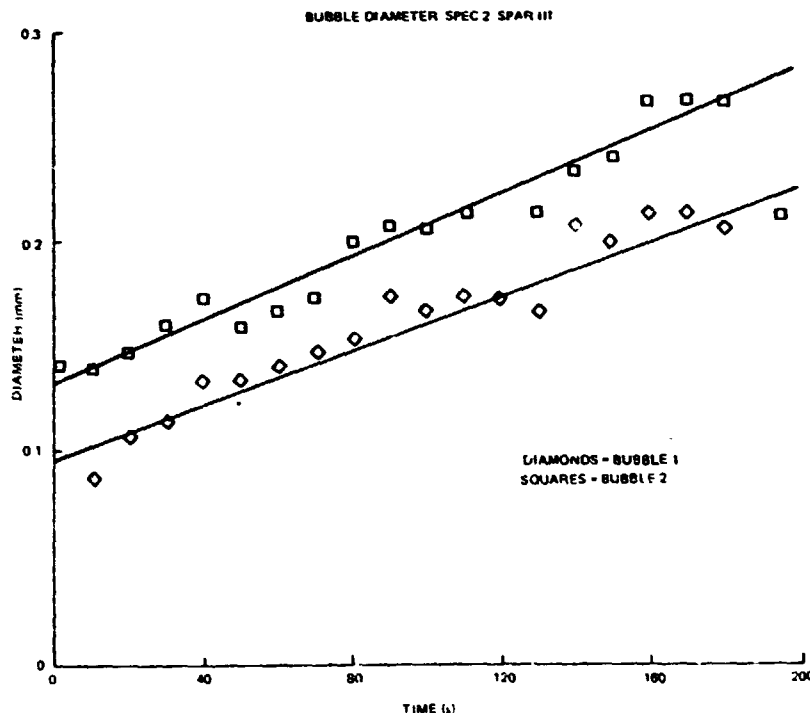


Figure 12. Bubble diameters as a function of time, specimen B, SPAR III.

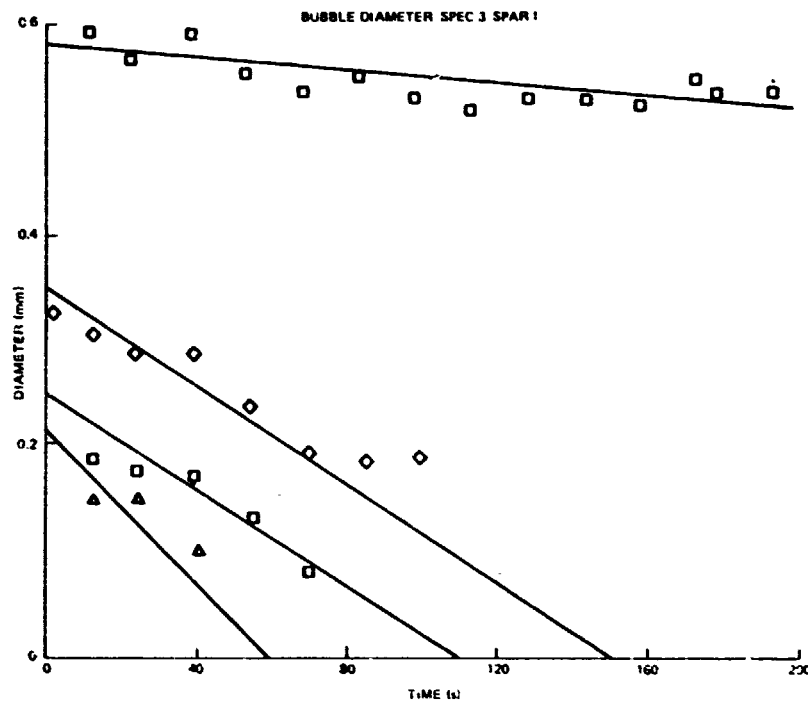


Figure 13. Bubble diameters as a function of time, specimen A, SPAR I.

DISCUSSION

There are several important aspects of these results. Among them are the greater void density observed in samples solidified in the absence of gravity, the observation that an initial temperature gradient of $20^{\circ}\text{C}/\text{cm}$ did not cause bubbles to detach from the interface or migrate through the liquid, and the fact that significant bubble pushing by the interface did not occur. All of these observations are identical to those of flight I, but we have now extended the regime to a higher temperature gradient.

It is probable that fluid motion induced by rocket spin and de-spin caused some leveling of the temperature gradient. As discussed in Reference 1, however, the direction of fluid motion, the superposed rocket thrust, and the specimen geometry were not conducive to complete homogenization of the temperature gradient. In addition, the pyrex tube, although isolated by vacuum along its length, is thermally tied to the heater blocks at its top and bottom ends. This will lead to some reestablishment of the thermal gradient. Crude estimates

of the time required for thermal reestablishment, however, indicate that it could only be partially complete in the 300 s available.¹ The inclination of growth direction in A, B, and C indicates the presence of a radial temperature gradient in addition to the longitudinal one. This radial gradient persists through the flight, and is probably due to the greater thermal conductivity of pyrex ($K = 9.6 \text{ mW/cmK}$) as compared to CBr_4 ($K = 2 \text{ to } 4 \text{ mW/cmK}$). The lower growth rate in D probably resulted from better thermal contact with the cell walls, thus greatly increasing reestablishment of the thermal gradient.

Void Morphology and Density

Gravitational forces have not affected the void morphology in specimens A, B, and C from flight III. Cylindrical voids were observed in both laboratory simulations and the flight experiment. Likewise, all of the specimens from flight I displayed spherical void morphology whether processed in the laboratory or in a weightless environment. The exception to this observation is specimen D for SPAR III. This zone refined material produced only one or two vertical cylindrical voids when processed in the laboratory, but spherical voids were grown in during flight III.² This behavior is thought to be significant for the following reasons. Previous work in this area has related observed void morphologies to the freezing rate, concentration of dissolved gasses, and the gas (solute) distribution coefficient. The systems studied were water-carbon dioxide [3,4,5] and stainless steel-hydrogen [6]. It is generally held with all other parameters constant, a low freezing rate will lead to bubble pushing, an intermediate freezing rate will give cylindrical voids, and a high freezing rate will produce spherical voids. The critical velocity for bubble pushing varies from system to system and has not been widely studied but is thought to be fairly low, approximately $5 \mu\text{m/s}$ for a planar interface.³ A comparison of our flight and ground base results, Table 2, shows that the void morphology seems to be more affected by a change in temperature gradient, G , than by a change in

1. The distance, a , from the solid-liquid interface to the top end of the specimen tube is approximately 3 cm, the thermal diffusivity, K , is approximately $10^{-3} \text{ cm}^2/\text{s}$ for CBr_4 and $5 \times 10^{-3} \text{ cm}^2/\text{s}$ for pyrex. Thus, in 300 s we have $(Kt/a^2) \sim 0.03$ for the CBr_4 and 0.15 for the pyrex. Reestablishment of one-half of the lost gradient would require $(Kt/a^2) \sim 0.2$.
2. Specimen C, which was originally zone refined material, behaved similarly to A and B. Examination of C after the flight revealed a distinct yellowish tinge, typical of impure material, and the presence of numerous foreign particles. It is concluded that C was contaminated during preparation and was therefore not a high purity material.
3. D. R. Uhlmann, Private Communication, 1976.

growth rate R : i.e., spherical voids observed with $G = 5^\circ\text{C}/\text{cm}$, $R = 2.5$ to $14\ \mu\text{m}/\text{s}$, cylindrical voids observed at $G = 20^\circ\text{C}/\text{cm}$, $R = 10$ to $25\ \mu\text{m}/\text{s}$. These results are summarized in Figure 14. It is clear from this figure that G , the temperature gradient in the liquid, is a potent factor in determining void morphology. This was not anticipated and will be investigated further.

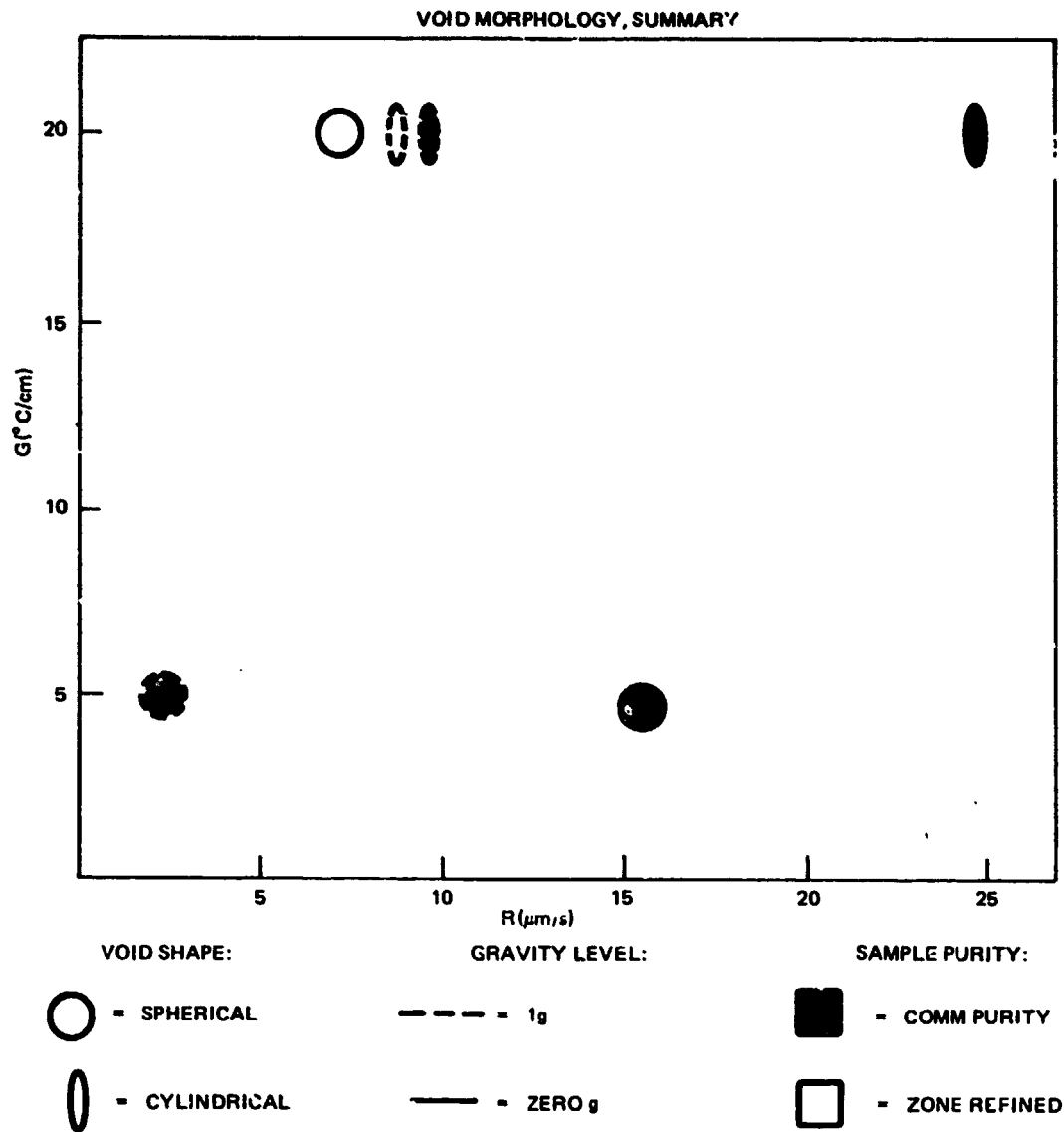


Figure 14. Summary of observation on void morphology.

Figure 14 also shows that, in general, the gravity level had little effect on void morphology except for the zone refined material processed on SPAR III (specimen D). The observed dependence of void morphology on temperature gradient might explain the behavior of specimen D. We suspect that in flight tests the initial temperature gradient is somewhat leveled by the rocket de-spin. This suspicion is founded on the observation that the growth rate, R , in flight was almost always greater than R in the laboratory, and we assume that the change in R is linked to a change in G . This assumed change in temperature gradient might have been sufficient to cause the morphological shift to occur. However, this shift could also be explained on the basis of a reduction in buoyancy force. It is thought that under conditions in which a cylindrical void is marginally unstable, a buoyancy force tending to keep the bubble uppermost during vertical growth might stabilize the cylindrical void rather than allow the interface to pinch it off. If either of these explanations is correct then we must also postulate an effect of interface morphology (i.e., dendritic versus planar) on void growth to explain specimens A, B, and C. These specimens should also have shifted to a spherical void morphology during rocket flight. The greatest difference between A, B, C, and D is the occurrence of a narrower mushy zone and a more planar interface in D. It is thought that during dendritic growth bubbles are trapped in interdendritic channels and therefore the cylindrical morphology is stabilized, whereas a bubble at a planar interface will be more exposed to the liquid. Thus, a shift from cylindrical to spherical voids would be expected to occur at different values of the buoyancy force or temperature gradient for the two types of interfaces. These results and our interpretation lead us to the tentative conclusion that void morphology is dependent upon the temperature gradient and interface morphology, and possibly the gravity level, in addition to the previously recognized dependence on growth rate, impurity concentration, and distribution coefficient.

The greater number of voids observed during low- g solidification on SPAR I and SPAR III might be simply explained. If the same quantity of gas were evolved and the same number of bubbles nucleated irrespective of gravitational forces, then one expects more voids in the low- g specimens because of the lack of buoyancy forces. The buoyancy forces detach bubbles from the interface and sweep them out of the liquid. However, the absence of gravity can also lead to an enhanced nucleation rate because of the reduced hydrostatic head [7]. This effect may be significant in heterogeneous nucleation. An enhanced nucleation rate could explain the extremely large number of voids observed in A, B, and C of SPAR III. In particular, Figure 4 shows that many bubbles were nucleated shortly after solidification began. Measurements of void length and growth rate indicate that the voids first appeared at $t_0 + 70$ s, which coincides with establishment of low- g . However, the location of voids

may simply be a reflection of the time necessary to achieve the required supersaturation of gas in the liquid after enough solidification had occurred. The fact that specimen D did not have many small voids but merely a few larger ones might be taken as evidence in favor of the heterogeneous nucleation hypothesis, since the purer material would offer fewer sites for heterogeneous nucleation and hence would be less affected by the hydrostatic head. We are unable to verify either hypothesis on the basis of current data.

As a footnote to the above discussion, it was observed that in some badly contaminated areas of the specimens, orange-brown pockets of bromine were present, but that none of the voids discussed were colored. Thus, we conclude that the voids were not a spurious result of the decomposition of CBr_4 .

Bubble Motion and Growth

The increase in bubble diameter as a linear function of time is not understood, since any surface area-related phenomenon should obey a power law. The simplest explanation for this behavior is that the liquid is saturated with nitrogen and the gas solubility decreases with decreasing temperature. The combination of a power law dependence with the decreasing temperature, hence solubility, of the liquid might lead to the roughly linear behavior shown in Figure 12. We can offer no explanation for the opposite behavior of bubble diameter in flight I.

The presence of so many small bubbles in the liquid portion of A, B, and C was totally unexpected. The origin of these bubbles is unknown; they must have been generated during the 100 s interval between launch and the start of picture taking. Three possible explanations are thought to be as follows: (1) the bubbles were released by the solid while being melted back by the spinning liquid and subsequently dispersed by fluid flow; or (2) the bubbles were nucleated spontaneously due to the reduction of hydrostatic head upon attainment of low-g; or (3) the bubbles were nucleated by a particular vibrational frequency of the rocket motor. It is thought that (1) is unlikely since there are an extremely large number of bubbles, they are uniformly distributed throughout the liquid, and they are not situated on the tube wall as might be expected if they were dispersed by de-spin. It is not possible to distinguish between (2) and (3), but we plan to start the camera earlier on SPAR V in hopes of observing the specimens immediately after de-spin.

The existence of these small bubbles and their subsequent growth shows that they are in equilibrium with the liquid. This may occur because of the cooling of an initially saturated liquid or it may be a gravity related effect.

Larson [8] has shown that the reduction in hydrostatic head which occurs under gravity-free conditions can be accounted for by considering a reduced pressure regime in the P-T-X equilibrium diagram. When this is done a liquid + vapor field is often found to move downward in temperature. Thus, a single phase liquid can, upon reduction of the applied pressure or hydrostatic head, decompose to a two phase liquid and vapor mixture. Variations in the pressure inside the specimen ampoules and the temperature in various locations in the liquid could then give rise to the observed variations in bubble densities.

The absence of any uniform, surface tension driven bubble motion in the liquid portion of our specimens was once again unexpected. We think that this immobility was either due to contamination of the bubble surface by an impurity which arrested the flow or a temperature gradient insufficient to cause flow. Earlier suppositions that the bubbles were pinned by being in contact with the tube wall have been discounted because the flight film shows that the advancing interface obscures the bubbles; therefore, the bubbles are on the far side of the interface and cannot be against the nearer tube wall, and the surfaces of the returned samples are smooth with no surface voids (i.e., all of the bubbles are totally enclosed by CBr_4).

Recent attempts to duplicate the Young, Goldstein, and Block experiment (upon which our estimates of bubble velocities of several millimeters per second were based) have shown once again that surface tension driven flow occurs readily in viscous silicone oils [9,10], and that this flow can counterbalance the gravitationally induced buoyancy force on a bubble. However, attempts to cause this flow to occur in other materials were unsuccessful; it was thought by the experimenters that this lack of flow was due to an impurity effect.⁴ It is curious that our purified sample (D, SPAR III) had no small bubbles in the liquid. This may be a nucleation effect as discussed earlier, or perhaps bubbles were initially present, were mobile, and migrated to the not end of the sample tube in the 30 s between initiation of low-g and start of the camera. The large bubble visible at the top of the tube did not move; however, since it was present before the flight, it would have had ample time to become contaminated.

The Marangoni numbers for the bubbles encountered in this experiment are listed in Table 3; they were calculated from measured values of the physical properties of CBr_4 [11] and an assumed value of the thermal conductivity, $K = 0.12 \text{ J/msk}$. They range from approximately 1 to 5000. Although Pearson calculates that a critical Marangoni number of 80 must be exceeded for flow to occur in a horizontally planar geometry [12], both the Young, Goldstein, Block, and Corriell, Hardy, Cordes experiments demonstrate significant surface tension

4. S. C. Hardy, Private Communication, 1977.

TABLE 3. MARANGONI NUMBERS (Ma) FOR
VARIOUS BUBBLE DIAMETERS

SPAR I (5°C/cm)		SPAR III (20°C/cm)	
d (mm)	Ma	d (mm)	Ma
0.1	0.6	0.1	3.1
1.0	80	1.0	310
2.0	1250	4.0	5000

driven flow in bubbles at very low Marangoni numbers of the order of 10^{-4} . Therefore, Pearson's criterion is not applicable to thermocapillary flows in bubbles. An analogy is the occurrence of natural convection in horizontal or vertical planar geometries. In a horizontal geometry, the critical Grashoff number must be exceeded for flow to occur. In a vertical geometry, convection will occur for any non-zero Grashoff number.

The observation of bubble and fluid motion in B is significant but puzzling. It seems clear that the downward motion of the large bubble caused the other bubbles to move. One possible driving force for the motion of the large bubble is surface tension driven flow, but the bubble moved opposite to the predicted direction (i.e., from hot to cold). This is reminiscent of observations of the motion of two phase inclusions in salt crystals, which also go from hot to cold [13,14]. The mechanism in that case is complex, involving evaporation and condensation. Alternatively, surface active impurities whose adsorption is thermally activated can cause the temperature dependence of the surface tension to change sign [15, 16, 17]; this would result in a reversal of the predicted direction of motion. Either of these mechanisms or modifications thereof might explain the motion of the large bubble. Coalescence could not be the driving force because the observed motion was relatively uniform and low velocity, rather than abrupt and rapid. Shrinkage due to solidification and cooling could be expected to account for a maximum uniform downward motion of approximately $(0.04)(6 \text{ mm}) = 0.24 \text{ mm}$. The motion observed in B was much greater. Similarly, downward motion of the liquid is sometimes observed during directional solidification of plastic crystals; this is thought to be caused by aspiration of the melt into cracks and cavities which occur during cooling of the solid. This mechanism should, however, lead to a relatively uniform downward motion of the liquid.

As shown in Table 3, the largest bubbles have the largest Marangoni numbers, and they would be expected to move first as a result of surface tension forces. If the motion was actually driven by Marangoni flow, then the major unanswered questions are: why did not the other large bubble (specimen D) move, and what was the specific mechanism which caused motion in the wrong direction?

Subsequent to these observations, the film of SPAR I was reviewed at high speed. It was noticed that the abrupt coalescence of two large bubbles at the interface of specimen C, SPAR I, caused a smaller bubble in the liquid to move a short distance (approximately 0.2 mm). Thus, we have another instance in which the motion of a large bubble caused fluid flow and hence pushed neighboring small bubbles. These observations document a source of fluid flow in low-g, namely, fluid motion due to bubble coalescence or due to the motion of large bubbles.

CONCLUSIONS

1. A greater number and a greater total volume of voids are present in specimens of nitrogen saturated CBr_4 when they are solidified in a low-g environment. This is directly attributable to the absence of buoyancy forces.
2. The morphology of grown-in voids was found to be dependent upon the applied temperature gradient. A temperature gradient of $20^\circ\text{C}/\text{cm}$ results in cylindrical voids whereas a gradient of $5^\circ\text{C}/\text{cm}$ results in spherical voids, all other things being equal. The void morphology was dependent on gravity in the case of zone refined material only.
3. Reduced gravity favors easier void nucleation and may favor easier bubble nucleation in CP CBr_4 .
4. An initial temperature gradient of $20^\circ\text{C}/\text{cm}$ does not cause bubbles to detach from a liquid-solid interface or to migrate to the hot end in liquid CBr_4 .
5. Solidification interfaces in CBr_4 are not able to cause long distance (greater than 0.2 mm) pushing of bubbles.
6. Motion or coalescence of bubbles can cause significant fluid flow in weightless liquids.

REFERENCES

1. Papazian, J. M. and Wilcox, W. R.: Thermal Migration of Bubbles and their Interaction with Solidification Interfaces. In SPAR I Final Report, NASA TM X-3458, December 1976, p. VII-1.
2. Gutowski, R. M.: Purification of Carbon Tetra bromide. M.S. Thesis, Clarkson College of Technology, 1977.
3. Chalmers, B.: Principles of Solidification. John Wiley and Sons, Inc., New York, 1964.
4. Rocquet, P., Rossi, J. C. And Gironne, J. Adam: Comparative Quality on Flat Rolled Products Produced from Continuously Cast and Conventionally Rolled Slabs. J. Metals, August 1967, p. 57-61; and Recherches sur l'Effervescence lors de la Solidification de l'Acier. Revue de Metallurgie, vol. 4, Anné 1968, p. 257.
5. Vasconcellos, K. F. and Beech, J.: The Development of Blowholes in the Ice/Water/Carbon Dioxide System. J. Crystal Growth, vol. 26, 1975, pp. 85-92.
6. Fredrikson, H., and Svensson, I.: On the Mechanism of Pore Formation in Metals, Met. Trans., vol. 7B, December 1976, p. 599.
7. Wilcox, W. R. and Kuo, V. H. S.: Gas Bubble Nucleation During Crystallization. J. Crystal Growth, vol. 19, 1973, pp. 221-228.
8. Larson, Jr., D.: Effects of Gravity Reduction on Phase Equilibrium. Grumman Research Department Memoranda RM-608, September 1975; RM-622, July 1976.
9. Young, N. O., Goldstein, J. S., and Block, M. J.: The Motion of Bubbles in a Vertical Temperature Gradient. J. Fluid Mech., vol. 6, 1959, p. 350.
10. Coriell, S. R., Hardy, S. C., and Cordes, M. R.: Melt Shape in Weightless Crystal Growth. NBS Space Processing Research, NBSIR 77-1208, Annual Report, February 1977, p. 72.
11. Chou, S. A.: Physical Properties of Carbon Tetra bromide. M.S. Thesis, Clarkson College of Technology, 1976.

REFERENCES (Concluded)

12. Pearson, J. R. A.: On Convection Cells Induced by Surface Tension. *J. Fluid Mech.*, vol. 4, 1958, pp. 489-500.
13. Wilcox, W. R.: Anomalous Gas-Liquid Inclusion Movement. *Industrial and Engineering Chemistry*, vol. 61, March 1969, pp. 76-77.
14. Anthony, T. P. and Cline, M. E.: The Thermomigration of Biphase Vapor-Liquid Droplets in Solids. *Acta Met.*, vol. 20, 1972, p. 247.
15. Jones, H. and Leak, G. M.: The Effect of Surface Adsorption on Zero Creep Measurements in Iron-Silicon Alloys. *Acta Met.*, vol. 14, 1966, p. 21.
16. Jones, H. and Leak, G. M.: The Surface Entropy of Solid Metals. *Metal Science Journal*, vol. 1, 1967, p. 211.
17. Murr, L. E.: *Interfacial Phenomena in Metals and Alloys*. Addison-Wesley, Reading, Massachusetts, 1975.

CHAPTER V

EPITAXIAL GROWTH OF SINGLE CRYSTAL FILM

Experiment 74-45

By

Dr. M. David Lind

Rockwell International Science Center

BACKGROUND

Liquid phase epitaxy (LPE) is a method of growing crystals by bringing a substrate crystal into brief contact with a melt or molten solution near its melting point. Low-g environment is of particular benefit to LPE because of the elimination of convection during crystal growth, as well as simplification of the problem of initial homogenization of the molten solution prior to initiating crystal growth. Modest improvements in crystal quality can have significant technological and economic importance.

OBJECTIVES

The objectives of the experiment are to grow an epitaxial film of gallium arsenide (GaAs) using the LPE technique in a microgravity environment, and to examine, characterize, and determine the quality of the film produced.

DISCUSSION

In this experiment, two GaAs wafer substrates are mounted in a graphite slider moved by means of a piston to bring the GaAs wafers into contact with a high temperature ($\sim 720^{\circ}\text{C}$) saturated solution of GaAs in liquid Ga. At the end of a 1 min growth period the piston was intended to retract the slider, thus ending the contact between the substrates and the growth solution, terminating crystal growth.

During the SPAR III flight, the furnace and its control system worked properly until the slider mechanism with the substrate was moved into contact with the growth solution. The temperature readings became erratic at that time making it difficult to determine what temperature was near the growth solutions. Post-flight inspection showed that the slider mechanism was broken during substrate contact with the solution. When the slider mechanism was withdrawn, it failed to remove the substrate from the growth solution.

PRECEDING PAGE BLANK NOT FILMED

CONCLUSION

A temperature anomaly and mechanical failure precluded achieving the experiment objectives. Modification of the slider mechanism has been carried out to correct the mechanical problem experienced on SPAR III. A post-flight analysis is underway to determine the cause of the temperature anomaly and to make modifications as required to prepare the experiment for reflight, expected to occur on SPAR V.

CHAPTER VI

CONTAINERLESS PROCESSING OF BERYLLIUM

Experiment 74-48

By

Gerald Wouch, George H. Keith, and
Robert T. Frost

Space Sciences Laboratory
General Electric Space Division

and

Norman P. Pinto

Kawecki Beryllco Industries, Inc.

ABSTRACT

Melting and solidification of a beryllium alloy containing 1.5 percent BeO by weight in the weightless environment of space has produced a new material not produced terrestrially, to our knowledge, namely cast beryllium with a relatively uniform dispersion of BeO throughout. Examination of the cast material shows that it is coarse grained, although the BeO is not heavily agglomerated in the flight specimen. Ground based comparison experiments show extreme agglomeration and segregation of BeO, resulting in large zones which are practically free of the oxide. Several postulated hypotheses for the failure to grain refine the beryllium have been formulated. These are: (1) spherodization of the BeO particles during specimen preparation and during the molten phase of the experiment, (2) loss of nucleation potency through aging in the molten phase, and (3) inability of BeO to act as a grain refiner for beryllium. Further investigation with non-spherodized particles and shorter dwell times molten may delineate which of these hypotheses are valid. The results of this flight experiment indicate that the weightless environment of space is an important asset in conducting research to find grain refiners for beryllium and other metals for which cast dispersions of grain refining agents cannot be prepared terrestrially due to gravitationally driven settling and agglomeration.

SUMMARY

This report describes preparatory ground based research and subsequent sounding rocket experiment wherein beryllium alloy HIP-50 was melted and solidified in the weightless environment of space in the NASA Electromagnetic Containerless Processing Payload (ECPP) on SPAR III. During that experiment, successful melting and solidification was achieved. Although a stiff oxide layer formed on the specimen due to the lack of a clean vacuum environment for the specimen in this first containerless experiment, the technique allowed rapid radiative cooling and solidification of the specimen and pyrometric observation of the specimen surface without interference from a container or hot oven walls.

Comparisons with ground based produced specimens show that the flight specimen has a much more uniform distribution of beryllia (BeO) and is essentially unagglomerated. Heavy agglomeration and separation was produced in the ground based reference experiments. The results of metallographic investigations and scanning electron microscopy are presented in the following discussion.

It was observed that while the BeO distribution was uniform and unagglomerated in the flight specimen, grain refinement did not occur and the castings are coarse grained. Several hypotheses requiring further investigation have been formulated to explain the failure to produce a relatively fine grained casting. These experiments would require a shorter dwell time while molten and utilize material prepared so that BeO particles with smooth facets with sharp corners were present initially.

Whereas many potential grain refining agents for beryllium agglomerate and segregate from the melt terrestrially due to (1) Stokes collisions and (2) velocity gradient collisions, this experiment indicates that the weightless environment of space is an important asset for conducting research to assess the potency of these agents as grain refiners. The results show that agglomeration and separation times are greatly extended in the weightless environment of space due to the reduction in collision frequency through gravity driven mechanisms such as Stokes collisions and fluid motions induced by gravity driven convection.

INTRODUCTION

Cast beryllium is coarse grained and, consequently, brittle. Subsequent hot working is required to refine the grain structure before cast beryllium can be used for most applications. Because of the problems in casting and subsequent

hot working the cast beryllium, powder metallurgy is used. Beryllium metal is principally produced in final form by consolidating a fine powder, usually No. 200 or 300 mesh; that is, 77 or 44 μm , respectively, either by vacuum hot-pressing or by hot-isopressing. Occasionally, standard cold pressing and sintering techniques are used to produce some material. Some cast metal is used after hot working, particularly where its purity and cleanliness cannot be matched by the powder metallurgical product.

The desirability of obtaining fine grained castings of beryllium with good mechanical behavior has spurred research to find a suitable grain refining agent for beryllium. Based on classical heterogeneous nucleation theory [1], a good grain refining agent should: (1) have a relatively high surface energy between the particle and the melt; (2) have a low surface energy between the solid and the particle; (3) be stable in the molten metal; (4) possess a maximum of surface area; and (5) have optimum surface character. Because of the lack of information [1] about the majority of these parameters, attention mainly has been concentrated on lattice disregistry between the nucleating particle material and the solid. The surface energy between the solid and the particle should decrease with decreasing lattice mismatch between particle and solid and with increasing chemical affinity between particle and solid [1]. Empirically, then, the search for grain refiners for casting has begun with lattice disregistry between the particle and the solid.

Consequently, for beryllium, one logical choice of a grain refining agent is BeO. Additionally it has been shown [2] that the grain growth stabilization temperature of beryllium can be raised by an oxide dispersion, the extent being inversely proportional to the particle size of the oxide dispersion. Thus, BeO might act as a grain refining agent to produce fine grained beryllium and to stabilize the grains produced, preventing excessive grain growth at high temperatures after solidification.

Attempts to produce castings of beryllium with a uniform dispersion of BeO, terrestrially, have not been successful due to agglomeration in the liquid state of the oxide particles and subsequent segregation of BeO from the melt. Agglomeration may occur due to: (1) Stokes collisions, which arise whenever larger particles rising or settling through the melt collect smaller particles and (2) gradient collisions, arising when particles are swept together by fluid flow. Stokes collisions require the presence of a gravity field, while gradient collisions may originate from gravity induced fluid flows such as convection but may also originate from other sources of fluid flow. A discussion of these mechanisms has been presented by Lindborg and Torsell [3]. NASA Contract No. NAS8-29748 has also considered these collision mechanisms in respect to agglomeration in immiscible liquid systems.

In the weightless environment of space, the reduced gravity should considerably reduce the agglomeration due to Stokes collisions and through reduction in gravity driven convection may also reduce agglomeration due to gradient collisions, although other sources of fluid motion such as Marangoni convection and stirring must be considered. Thus, in the weightless environment of space, a uniform dispersion of BeO might be obtained in cast beryllium. In light of these considerations, a sounding rocket experiment was flown on the NASA SPAR III sounding rocket. The experiment and the results of the experiment are discussed in the following paragraphs.

Experiment Objectives

The experiment objectives were:

1. To prepare cast beryllium with enhanced service properties through utilization of dispersed oxide, BeO, as a grain refining agent. Obtaining a finer grained casting of beryllium with a uniform dispersion of oxide throughout would produce a cast beryllium with enhanced room temperature ductility, coupled with high temperature strength. This would eliminate the present problems in subsequent hot working of the coarse grained castings presently produced to refine the cast structure. This goal has not been achievable in the terrestrial environment because of the unavoidable agglomeration and separation of BeO, as well as other potential grain refining agents from the melt.

2. To improve the microstructure of cast beryllium. Achievement of a uniformly dispersed oxide phase in ingot beryllium may lead to enhancement of some service properties of beryllium even if grain refinement is not achieved, provided that grain sizes do not exceed 100 μm and do not grow when the material is worked. Obtaining a uniformly dispersed oxide phase of sub micron sized particles may produce dispersion strengthened cast beryllium [2] and stabilize against further grain growth at high temperatures. Achievement of a uniform dispersion of oxide can also demonstrate the feasibility of casting beryllium with additions other than BeO (e.g., titanium, tungsten, etc.) as possible grain refining agents in the weightless environment of space.

Minimum Criteria for Success

To measure the success of the experiment in terms of the experiment objectives previously discussed, a set of minimum criteria for success was established. These were:

1. Satisfactory melting and solidification (minimum contamination from atmosphere, no contamination by contact, proper shape of casting).

2. Improved cast microstructure — presence of a dispersed oxide phase in ingot beryllium. This will also indicate feasibility of using additions other than BeO, e.g., Ti, W (impossible in conventional melting).

3. Improved cast microstructure — finer cast grain size.

4. Improved service properties.

General Experiment Description

The experimental program followed, leading up to the flight experiment, accomplished the necessary preliminaries to the flight experiment, including:

1. The selection of the flight specimen composition.

2. The establishment of cleanliness requirements during the melting and solidification, particularly with respect to water vapor and oxygen.

3. Ground based reference experiments, representing the best attempt to simulate, terrestrially, the conditions of melting, cooling, and solidification occurring during the flight.

The specimens obtained from the ground based reference experiments are the basis of comparison between the results of the flight experiment in the weightless environment of space and what can be achieved terrestrially. The results obtained in these ground based reference experiments were compared with previous experiments conducted in beryllium casting at Kawecki Beryllco Industries (KBI) and also with the results of experiments conducted on NASA Contract No. NAS8-29626 [4].

After establishing the necessary preliminary data, the flight specimen composition was selected (HIP-50 KBI alloy) to be a hot isostatically pressed beryllium alloy containing 1.5 percent BeO by weight. The flight experiment consisted of melting and solidification of a specimen of this composition in the ECPP developed for the SPAR program. The results of this experiment were then compared with that obtained from the ground based reference experiments performed.

Ground Based Experiment Description and Apparatus

Experiments in the terrestrial environment were performed in either a hot wall furnace at KBI or in the General Electric breadboard apparatus at KBI. The hot wall furnace was used to prepare a range of compositions of specimens by melting and solidifying a range of compositions of hot isostatically pressed beryllium alloys. The BeO content was varied from 0.6 to 4.5 percent BeO by weight. Melting and cooling curves were obtained by optical pyrometry. As the thermal time constant is large in this furnace, the rapid heating and cooling capability of the LCPP cannot be duplicated with this furnace. Thus, in no way were these initial furnace experiments intended to serve as the ground based reference experiment. They did enable the grain size, agglomeration of BeO, and homogeneity of product as functions of the initial composition and slower temperature-time kinetics to be studied. The metallographic studies of these specimens, reported in the following test, enabled the flight specimen composition to be chosen, 1.5 percent BeO by weight (KBI HIP-50 alloy) on the basis of smallest particle size obtained. All of these meltings were conducted with laboratory grade argon as the gaseous environment.

The General Electric breadboard apparatus was used to conduct the ground based reference experiments for melting and solidification of the HIP-50 beryllium alloy. The breadboard chamber contains a duplicate of the cusp coil and r.f. tank circuit used in the flight chamber. This apparatus is (as it is named) a breadboard of the ECPP, with a somewhat larger levitation chamber. The chamber can be evacuated to 10^{-5} torr and filled with high purity argon through a small vacuum/gas supply system designed for this purpose. A mass spectrometer such as the VEECO GA-4 residual gas analyzer may be coupled into the chamber to study the residual gases present in the chamber prior to and after filling with high purity argon.

Two ground based reference experiments, duplicating insofar as is possible terrestrially the flight experiments, were performed in this apparatus, heating, melting, and solidifying a specimen of the KBI HIP-50 beryllium alloy in the presence of high purity, research grade argon. These experiments were performed at KBI's laboratory in Reading, Pennsylvania in a safe facility for beryllium, utilizing the breadboard apparatus. The specimens (0.922 cm in diameter spheroids of HIP-50 alloy) were sting mounted on a tungsten sting in the cusp coil. The specimens are heated and melted as in the flight apparatus by the r.f. induction field of the coil. Because beryllium is a light metal (density 1.848 gm/cm^3) enough levitation force is provided by the coil to support the specimens and they do not flow down the sting or fall when melted. Temperature is observed with a breadboard pyrometer, which is a duplicate of the

flight pyrometer, and a disappearing filament pyrometer looking through the observation port down onto the specimen through the mirror system provided in the chamber for this purpose. The performance and results of these experiments are described in the following text.

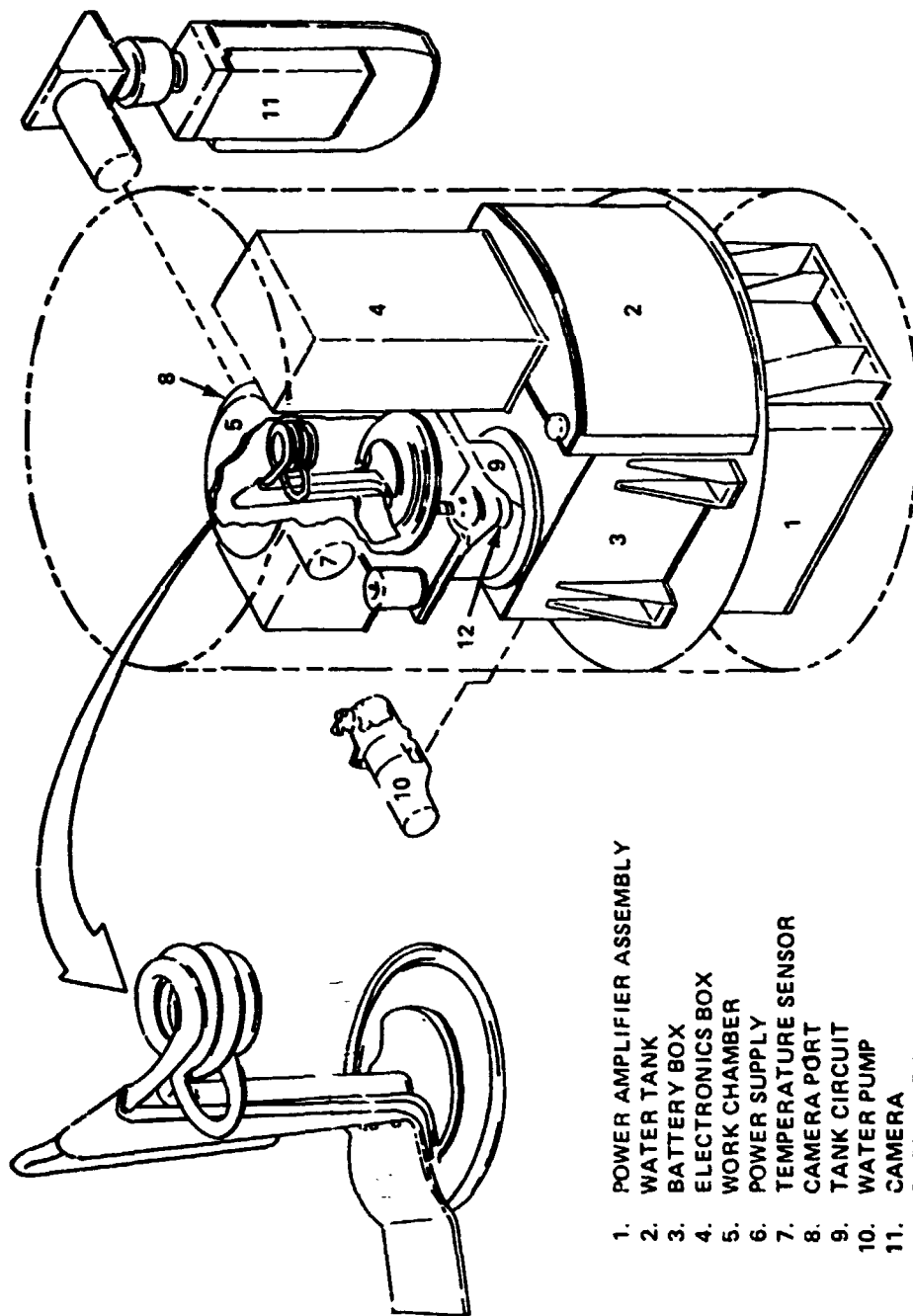
Flight Experiment Description and Apparatus

The flight experiment consisted of melting and resolidification, under 18 psi of research grade argon, a 0.922 cm diameter, spheroidal specimen of KVI HIP-50 beryllium alloy, containing 1.5 percent BeO by weight, in the weightless environment of space. The experiment was performed in the NASA ECPP flown on NASA SPAR III. A schematic of the ECPP is shown in Figure 1. Figures 2 and 3 show photographs of the ECPP and the levitation chamber, respectively.

The specimen is suspended in the electromagnetic field of the cusp coil and heated and melted by induction heating from the electromagnetic field of the coil. The cusp coil consists of adjacent coils having opposing alternating magnetic fields. The potential well in which the specimen is confined is symmetrical about the vertical axis and roughly shaped as shown in Figure 4. An active servo positioning system is utilized to maintain the specimen in the center of the coil system against accelerations during the flight and to damp out oscillations of the specimen in the coil system. During the low power mode, after heating and melting, the specimen solidifies with very little stirring.

The rocket-borne apparatus is described in the End Item Specification, SSL-ECPP-001, prepared under NASA Contract NAS8-30797. Drawings of the apparatus are referenced in this document. Mechanical, electrical, and functional interfaces with the rocked and prelaunch check-out equipment are detailed in the Final Interface Control Document, SSL-ECPP-009. Further information on the rocket-borne apparatus may be found in the final report for NASA Contract NAS8-30797 and the Experiment Implementation Plan for Containerless Processing of Beryllium prepared for NASA Contract NAS8-31963.

The processing chamber was cleaned, evacuated, and baked out for two days at 130°F. Mass spectrometric analysis of the residual gas showed less than 50 ppm of water vapor and oxygen present after evacuation before filling with research grade argon. The research grade argon used contains less than 2 ppm of oxygen and 3 ppm of water vapor, and was dried by passing through a cold trap with liquid nitrogen as the coolant. Thus, the water vapor and oxygen content of the gas was sufficiently low enough to prevent excessive oxidation of the specimen.



1. POWER AMPLIFIER ASSEMBLY
2. WATER TANK
3. BATTERY BOX
4. ELECTRONICS BOX
5. WORK CHAMBER
6. POWER SUPPLY
7. TEMPERATURE SENSOR
8. CAMERA PORT
9. TANK CIRCUIT
10. WATER PUMP
11. CAMERA
12. PRESSURE SENSOR

Figure 1. Electromagnetic levitation furnace.

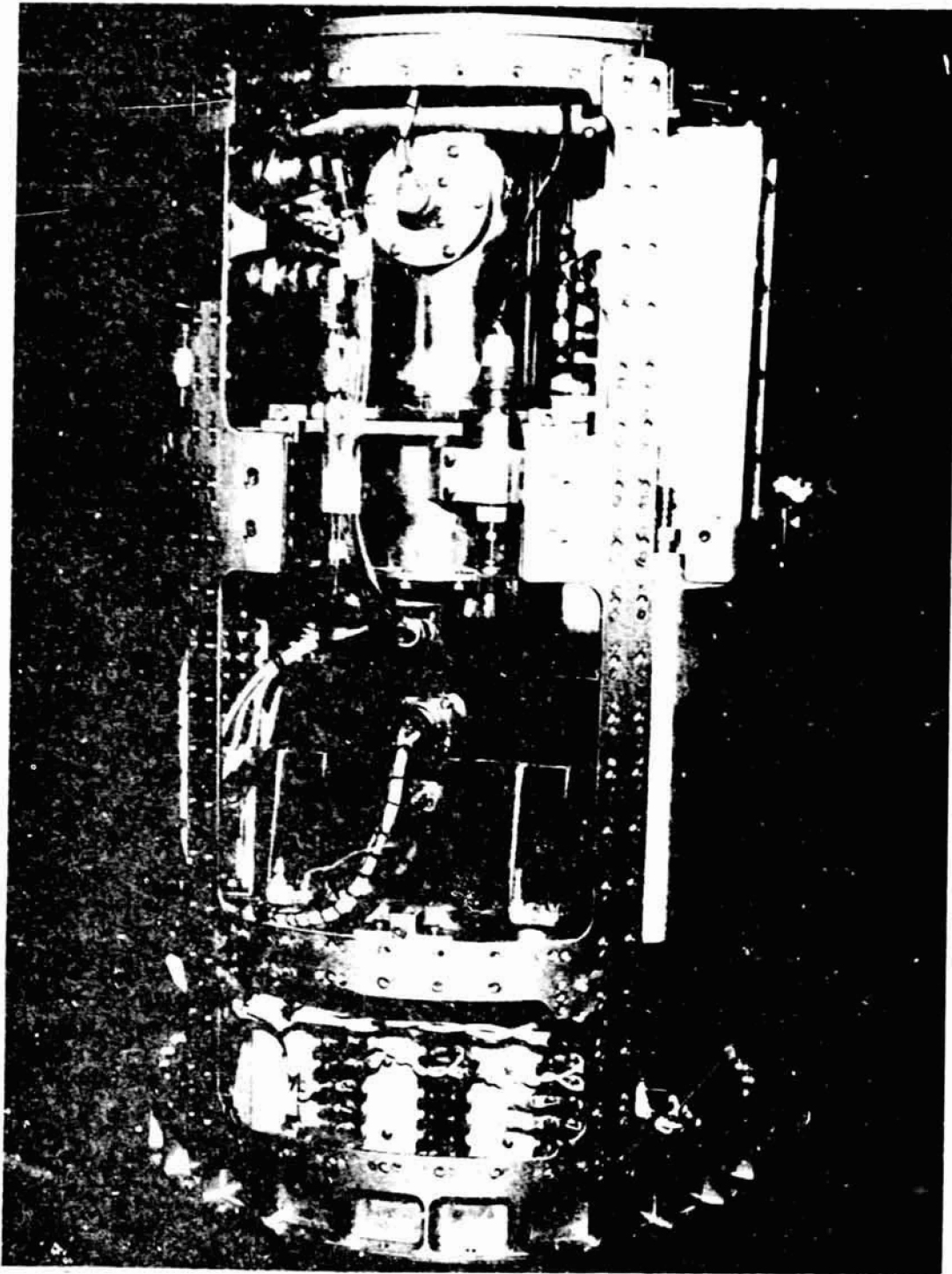


Figure 2. ECPP (outer skin removed).

VI-10

ORIGINAL PAGE IS
OF POOR QUALITY

ORIGINAL PAGE IS
OF POOR QUALITY

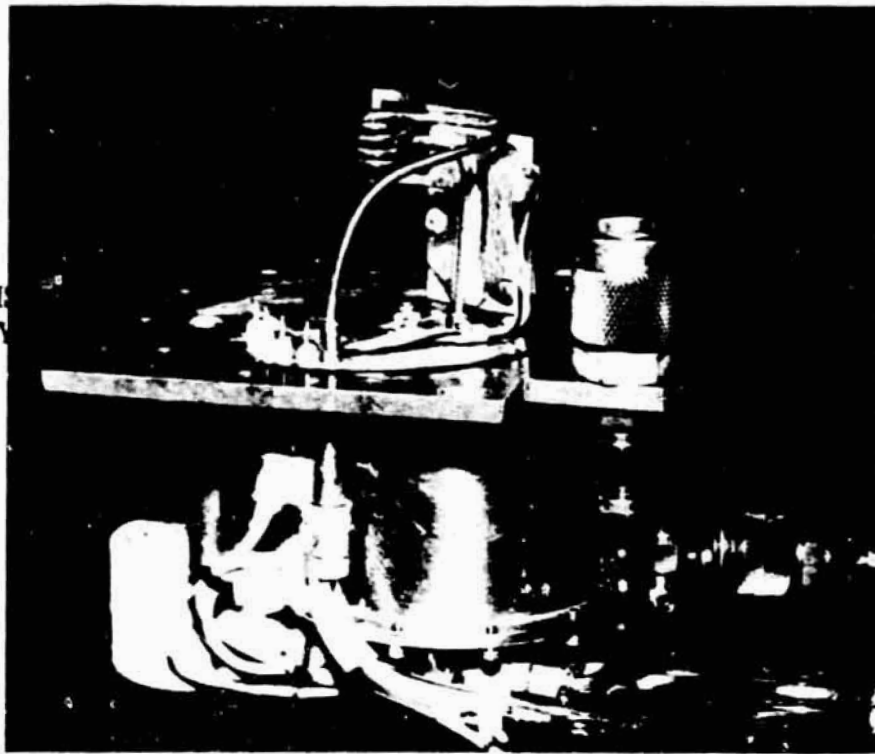


Figure 3. Work coil and matching transformer.

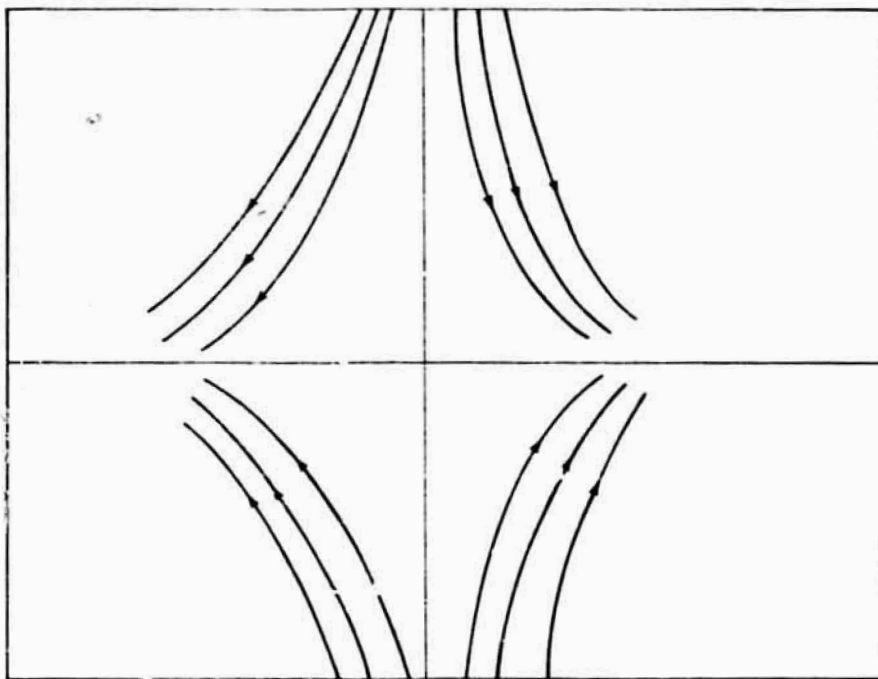


Figure 4. Field lines through vertical plane section of cusp coil.

The experiment sequence is controlled by a timer, which switches full power on 50 s after launch of the sounding rocket, when weightlessness has been established, and then into a low powered mode approximately 160 s after launch, so that the specimen may solidify. The ECPP is full automatic in operation when the timer sequence is initiated. A movie camera records the heating, melting, and solidification on film and a solid state, silicon detector records temperature data acting as a photometer. A full record of visual and temperature data is thus obtained. The performance and results of the flight experiment are described in the following text.

EXPERIMENT RESULTS

Ground Based Experiment Results: Basic Metallurgical Studies

Ground experiments performed were: (1) basic metallurgical studies and (2) ground based reference experiments. The basic metallurgical studies were performed in a hot wall furnace at KBI in commercial grade argon. With this furnace, the fastest cooling rate attained was 85°C/min and cooling rates varied 45°C/min to 85°C/min. Beryllium, with compositions of 0.6, 1.5, and 2 percent BeO by weight, were melted and solidified in this furnace. The 0.6 percent and 1.5 percent BeO alloys were high purity while the 2 percent BeO alloy was commercial purity. All of the alloys considered were prepared by hot isostatic pressing of powders and are standard KBI alloys.

Castings of these compositions were made of 0.922 cm diameter spheroidal specimens on a ceramic plaque (BeO) in the hot wall furnace. The basic metallurgical studies established: (1) a gravity effect on the BeO, showing agglomeration and settling, with the highest concentration of BeO at the bottom of each solidified specimen; (2) some retained BeO in the castings; (3) grain sizes of the order of 500 μm . The best castings with highest retained BeO and smallest grain size were with the 1.5 percent BeO by weight composition (HIP-50 alloy). Consequently, this composition was selected to be the flight specimen composition. The agglomeration and settling observed were expected as this has been the previous result of terrestrial casting experiments. Retained oxide in the castings, however, was encouraging. As these experiments were preliminary to the ground based reference experiments, no detailed SEM analysis was made of the oxide distribution. Smaller grain sizes were found at the surfaces of these castings not in contact with the ceramic plaque, where the specimen cooled fastest by radiation. They were not small enough, however, to be of significance (less than 100 μm would be significant).

Ground Based Reference Experiments

The ground based reference experiments, performed in the General Electric breadboard facility constitute the best attempt, terrestrially, to duplicate the flight experiment. These experiments were performed with spheroidal specimens of the KBI HIP-50 alloy, approximately 0.922 cm in diameter at a pressure of 1 torr of research grade argon. The results of these experiments constitute the reference comparison between what can be achieved terrestrially and what can be achieved in the weightless environment of space, utilizing apparatus identical in essential aspects to the flight experiment apparatus.

Figure 5 shows the heating and cooling curve as observed by a disappearing filament pyrometer during the experiment. The specimen was sting mounted upon a tungsten-rhenium thermocouple. Temperature-time data were recorded from the breadboard pyrometer and the thermocouple. However, the breadboard pyrometer saturated before melting and the thermocouple data were not reliable due to poor contact between thermocouple and specimen. The disappearing filament pyrometer data are reliable however and, consequently, are the data presented.

Grain Size and Morphology

Preliminary experiments, conducted by induction melting small beryllium samples of a mass approximately equal to the flight specimen geometry in a glove box, were characterized by microstructure evaluation. These specimens consisted of beryllium alloys with from 0.6 to 4.5 percent BeO by weight. The variables investigated were: (1) amount of BeO, (2) purity, (3) atmosphere (argon or vacuum), (4) dwell time in the molten state, and (5) surface condition.

Heating and cooling rates were measured by optical pyrometry. The maximum cooling rate observed was $85^{\circ}\text{C}/\text{min}$. This is attributed to the relatively large mass of the furnace, susceptor, and crucible used. Superheat obtained was 70 to 100°C . Recalescence was observed on freezing of all melts with the exception of one at an apparent freezing temperature of 1200 to 1220°C . It was also observed that an approximately $2\text{ }\mu\text{m}$ BeO surface layer formed on all pieces regardless of purity and BeO content.

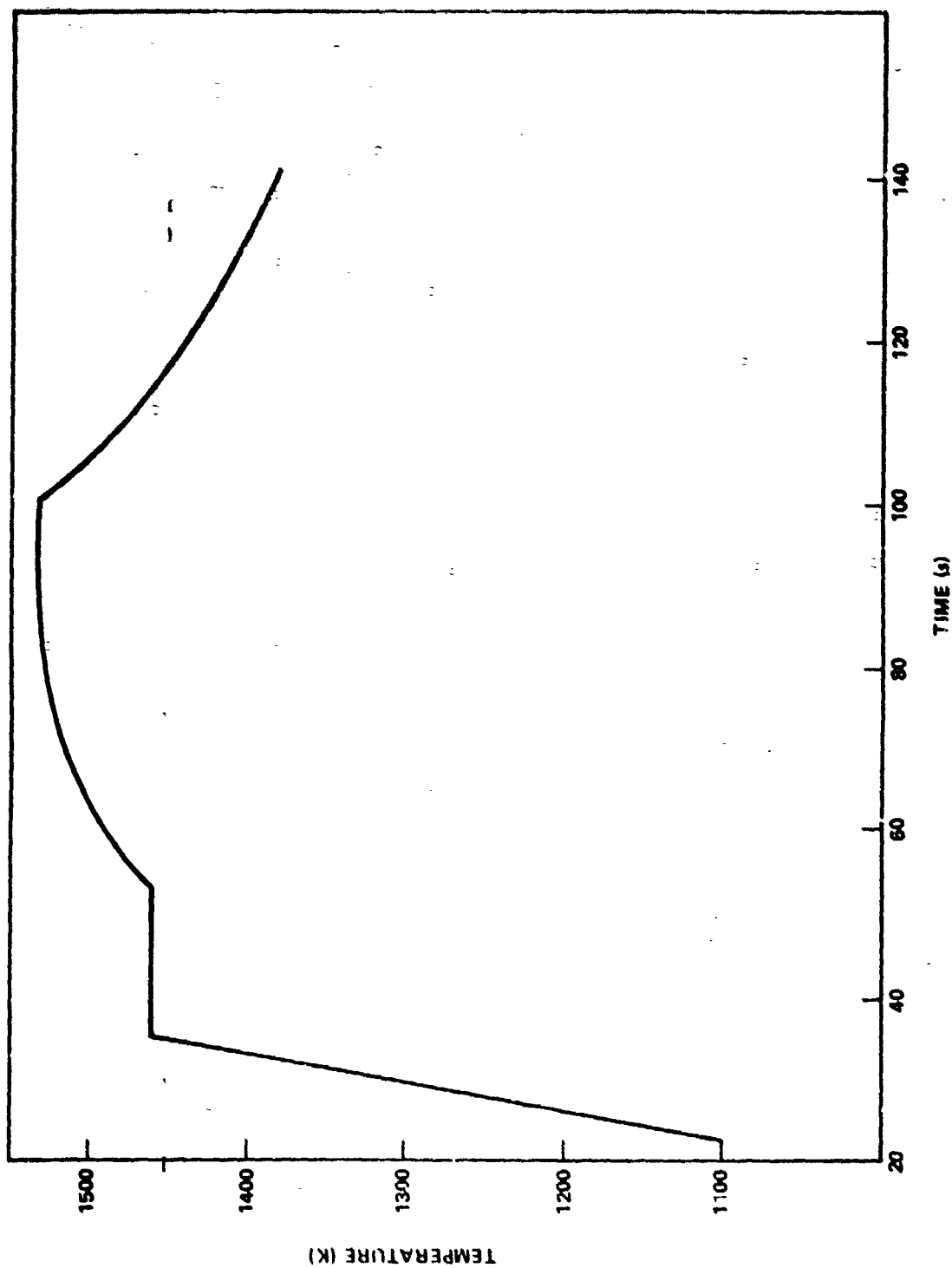


Figure 5. Time temperature curve for ground based specimen No. 1.

All specimens produced were large grained with an average grain size of 500 μm . Voids were left where low melting impurity phases had melted out. Figure 6, taken with polarized light, shows the typical microstructure produced. Figure 7, taken in bright field, shows the voids present. From these studies, two compositions were selected and these were 0.6 and 1.5 percent BeO by weight. High purity specimens of these compositions were solidified in the previously mentioned facility with cooling rates approximately 65 to 80°C/min and examined metallographically. The 1.5 percent BeO material showed the smallest grain size observed in the interior of the specimen. In contrast, the 0.6 percent BeO specimen showed a relatively fine grain size near the surface and extremely large grains in the interior. Therefore, the high purity 1.5 percent BeO material was chosen as the flight specimen material.

The flight and ground based experiments were conducted on material cut from a single pressing. Table 1 shows the mechanical properties based on an average of six tests, and Table 2 shows the grain size and chemistry. Two melts were made from the flight material using the previously mentioned facility. The measured cooling rate of both melts was 60°C/min. Figure 8 shows the starting pressed microstructure, and Figure 9 shows the microstructure after melting and solidification.

Two experimental melts were made in the General Electric breadboard facility using flight specimen material machined into 0.922 cm diameter spheres. Microstructure evaluation confirmed results of the previous work which was a relatively large grain size (though somewhat smaller than previously found) and development of porosity. Figure 10 (polarized light) and Figure 11 (bright field) show the typical grain size and shape and the voids, respectively. These two experiments constituted the ground based reference experiments for comparison with the flight specimen microstructure.

Oxide Particle Distributions

Using scanning electron microscopy, the oxide particle distributions in the ground based reference specimens were characterized. Figure 12 is a montage of one of the specimens made up from 30X SEM micrographs after sectioning and metallographic preparation. It is the result of the experiment duplicating (insofar as possible) the flight experiment, terrestrially. It is observed that gross agglomeration and segregation of BeO have occurred. The dark areas are virtually "cleared out" of oxide, whereas the white areas contain heavy agglomerations of oxide. Ground based reference specimen No. 2, which was melted and solidified at a slower rate, exhibits the same behavior showing gross agglomeration and segregation of BeO.



Figure 6. Typical microstructure produced from preliminary furnace experiments with HIP-50 alloy. Magnification is 100X.
Taken with polarized light.



figure 7. Bright field micrograph showing voids produced from preliminary furnace experiments with HIP-50 alloy.

TABLE 1. MECHANICAL PROPERTIES OF HIP-50 ALLOY BILLET,
BILLET NUMBER 75044A

Grain Size (μm)	Ultimate Tensile Strength (ksi)	Yield Strength (ksi)	Elongation (%)
3.6	88.2	66.2	4.2
(Based on metallographic measurements)	(Based on average of 6 tests)	(Based on average of 6 tests)	(Based on average of 6 tests)

TABLE 2. CHEMICAL PURITY OF BILLET NUMBER
75044A (HIP-50 ALLOY)

BeO	1.597 by weight
C	390 ppm
Fe	450 ppm
Al	85 ppm
Si	33 ppm
Mg	21 ppm
Ni	88 ppm

ORIGINAL PAGE IS
OF POOR QUALITY

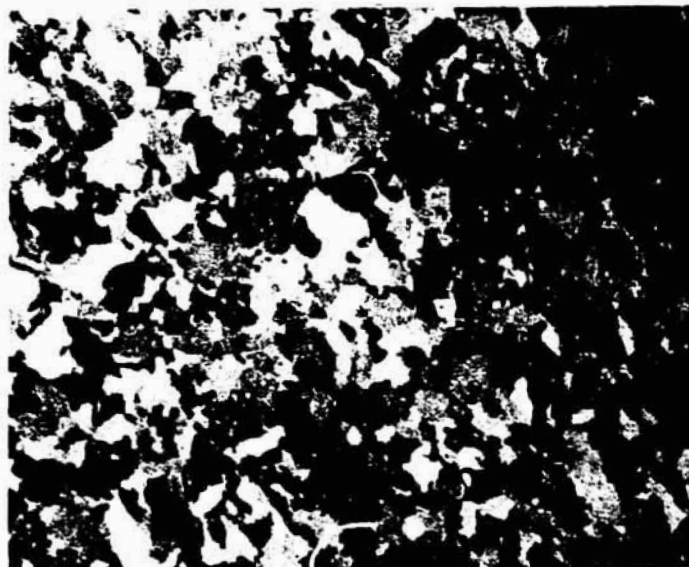


Figure 8. Starting pressed microstructure of HIP-50 alloy.
Magnification is 800X.



Figure 9. Microstructure produced from preliminary furnace experiment with HIP-50 alloy material cut from flight billet. Magnification is 100X. Taken with polarized light.

**ORIGINAL PAGE IS
OF POOR QUALITY**

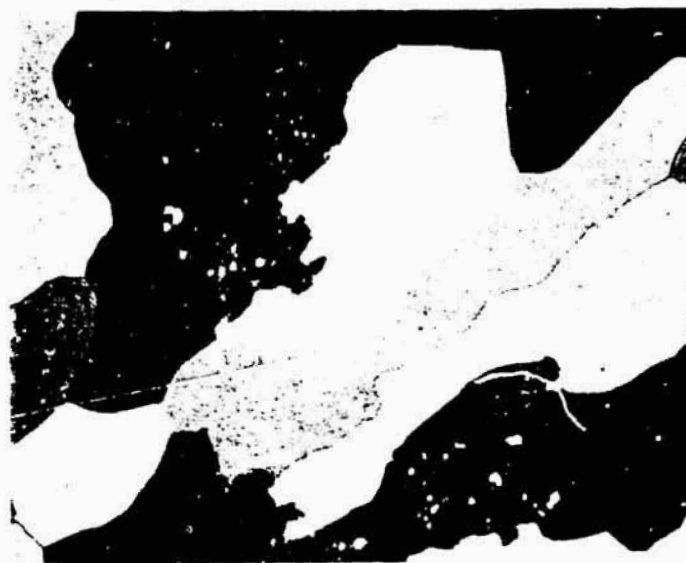


Figure 10. Microstructure produced from ground based reference experiment No. 2. Magnification is 100X.
Taken with polarized light.

ORIGINAL PAGE IS
OF POOR QUALITY

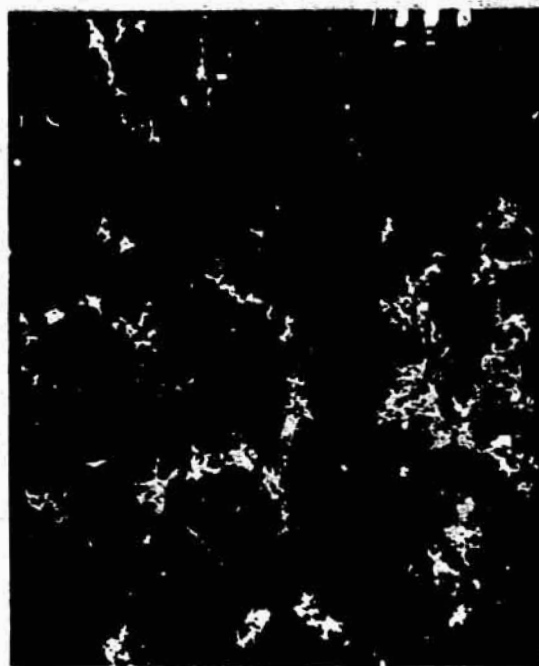
Figure 11. Bright field micrograph showing voids produced from ground based reference experiment No. 2.
Magnification is 100X.



Figure 12. Montage of 30X SEM micrographs of ground based reference specimen No. 1, reduced to size for reproduction. White regions are heavily agglomerated regions. Dark areas are cleared out regions.

Detailed SEM studies to magnifications of 30 000X were made of the various regions comprising each specimen. An overlay was made for each specimen and the regions labeled alphabetically. Figures 13 through 16 show region A of ground based specimen No. 1 with magnifications 1000X, 3000X, 10 000X, and 30 000X, respectively. This is a region of moderately heavy oxide concentration, having a volume fraction of 2 percent, determined by Quantimet Analysis, for the 1000X micrograph. As can be seen in the 30 000X micrograph, the oxide networks are composed of agglomerates of small oxide particles ranging in size from 0.02 to 1.3 μm .

Figures 17 through 20 show region B of ground based specimen No. 1, with magnifications 1000X, 2000X, 10 000X, and 30 000X, respectively. This is a region almost devoid of oxide, having a volume fraction of 0.002 percent



ORIGINAL PAGE IS
OF POOR QUALITY

Figure 13. SEM micrograph of Region A at 1000X magnification.
Region is not heavily agglomerated.

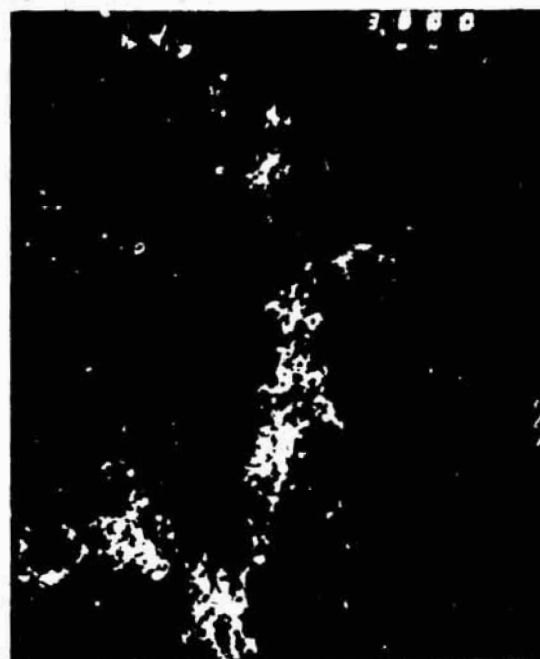


Figure 14. SEM micrograph of Region A at 3000X magnification.
Region is not heavily agglomerated.



Figure 15. SEM micrograph of Region A at 10 000X magnification.
Region is not heavily agglomerated.



Figure 16. SEM micrograph of Region A at 30 000X magnification.
Region is not heavily agglomerated.



ORIGINAL PAGE IS
OF POOR QUALITY

Figure 17. SEM micrograph of Region B at 1000X magnification.
Region is virtually void of all oxide but one composite particle
composed of oxide particles collected by collisions.



Figure 18. SEM micrograph of Region B at 3000X magnification.
Region is virtually void of all oxide but one composite particle
composed of oxide particles collected by collisions.



Figure 19. SEM micrograph of Region B at 10 000X magnification.
Region is virtually void of all oxide but one composite particle
composed of oxide particles collected by collisions.



Figure 20. SEM micrograph of Region B at 30 000X magnification.
Region is virtually void of all oxide but one composite particle
composed of oxide particles collected by collisions.

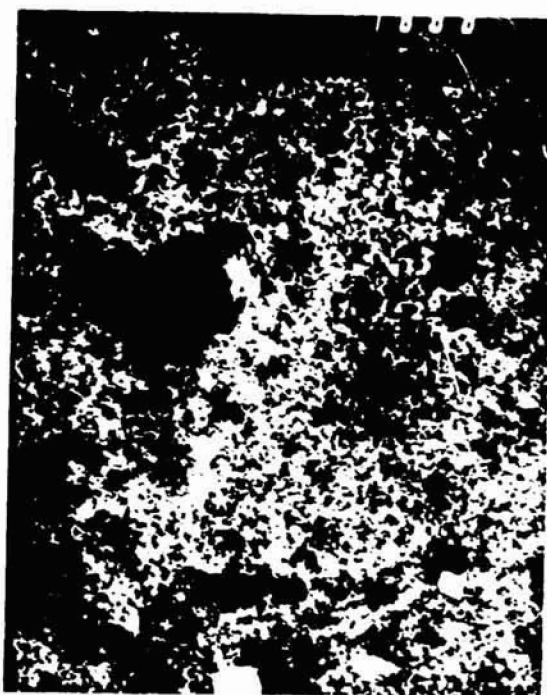
for the 1000X micrograph, determined by Quantimet Analysis. Figures 21 through 24 show region I of ground based specimen No. 1. This region is one of heavily agglomerated oxide. Ground based reference specimen No. 2 is similarly made up of regions of heavy oxide agglomeration and regions devoid of such agglomeration.

Figures 25 and 26 are plots of the oxide volume fraction determined by Quantimet Analysis of identified regions of ground based reference specimen No. 1 for 1000X and 3000X micrographs. Figures 27 and 28 are corresponding plots for ground based reference specimen No. 2. The fluctuations observed in volume fraction are indicative of the gross segregation of oxide observed in the terrestrial experiments. The differences are so large that four decade semilog paper were required to display the plots of volume fraction per region. The plots were normalized by volume fraction of region occupied by the type of BeO structure exhibited and to the initial BeO distribution before melting.

Flight Experiment Results

The flight experiment, flown on December 14, 1976 from White Sands Missile Range, performed the melting and solidification of a 0.922 cm diameter spheroidal specimen of HIP-50 beryllium alloy containing 1.5 percent BeO, under 18 psi of research grade argon, in the weightless environment of space. Table 3 shows the Major Event Record constructed from the telemetry records. Despite the failure of one of the power amplifiers 139.4 s after launch, the experiment operation proceeded as planned. The amplifier failure reduced the amount of superheating obtained. The major variable in the experiment was the weightless environment of space versus the terrestrial 1-g environment. The equipment operation is fully discussed in the final report for NASA Contract No. NAS8-30797, which was the hardware contract for construction and delivery to NASA of the ECPP. Only the pertinent aspects of equipment operation as regards to the experiment will be discussed herein.

Figure 29 is a macrograph of the specimen after solidification. As it was spheroidal before melting, there has been considerable shape change induced by the electromagnetic field configuration of the cusp coil. The specimen has assumed the "equatorial bulge" shape characteristic of the cusp field as previously discussed. The stiff oxide layer prevented the specimen from assuming the spherical shape dictated by surface tension while molten when the power is turned down to initiate solidification. The cracks normal to the surface about the equatorial ridge are evident in this photograph and in the view shown in Figure 31. Figures 30 and 31 are other views of the specimen. Possible explanations for the cracks are shrinkage or mechanical stresses supplied or a combination of the two.



ORIGINAL PAGE IS
OF POOR QUALITY

Figure 21. SEM micrograph of Region I at 1000X magnification.
Heavy agglomerated region.

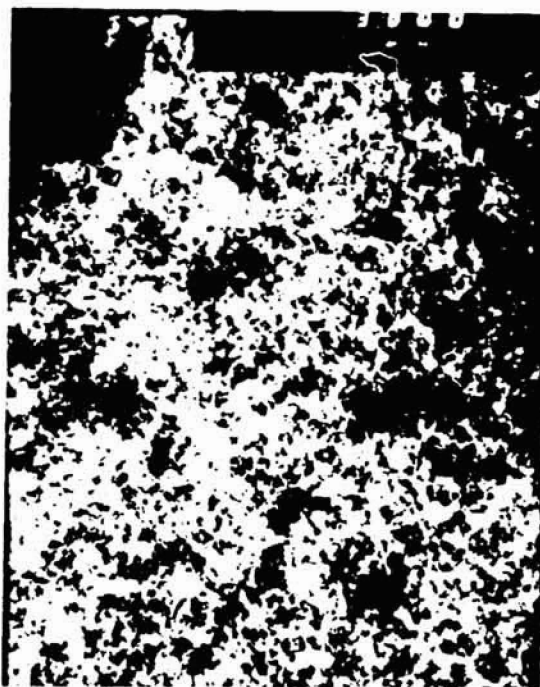


Figure 22. SEM micrograph of Region I at 3000X magnification.
Heavy agglomerated region.

ORIGINAL PAGE IS
OF POOR QUALITY

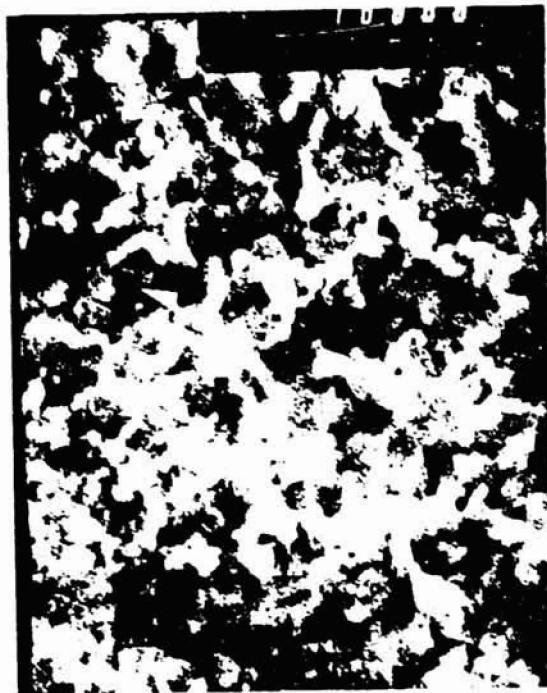


Figure 23. SEM micrograph of Region 1 at 10,000X magnification.
Heavy agglomerated region.



Figure 24. SEM micrograph of Region 1 at 30,000X magnification.
Heavy agglomerated region.

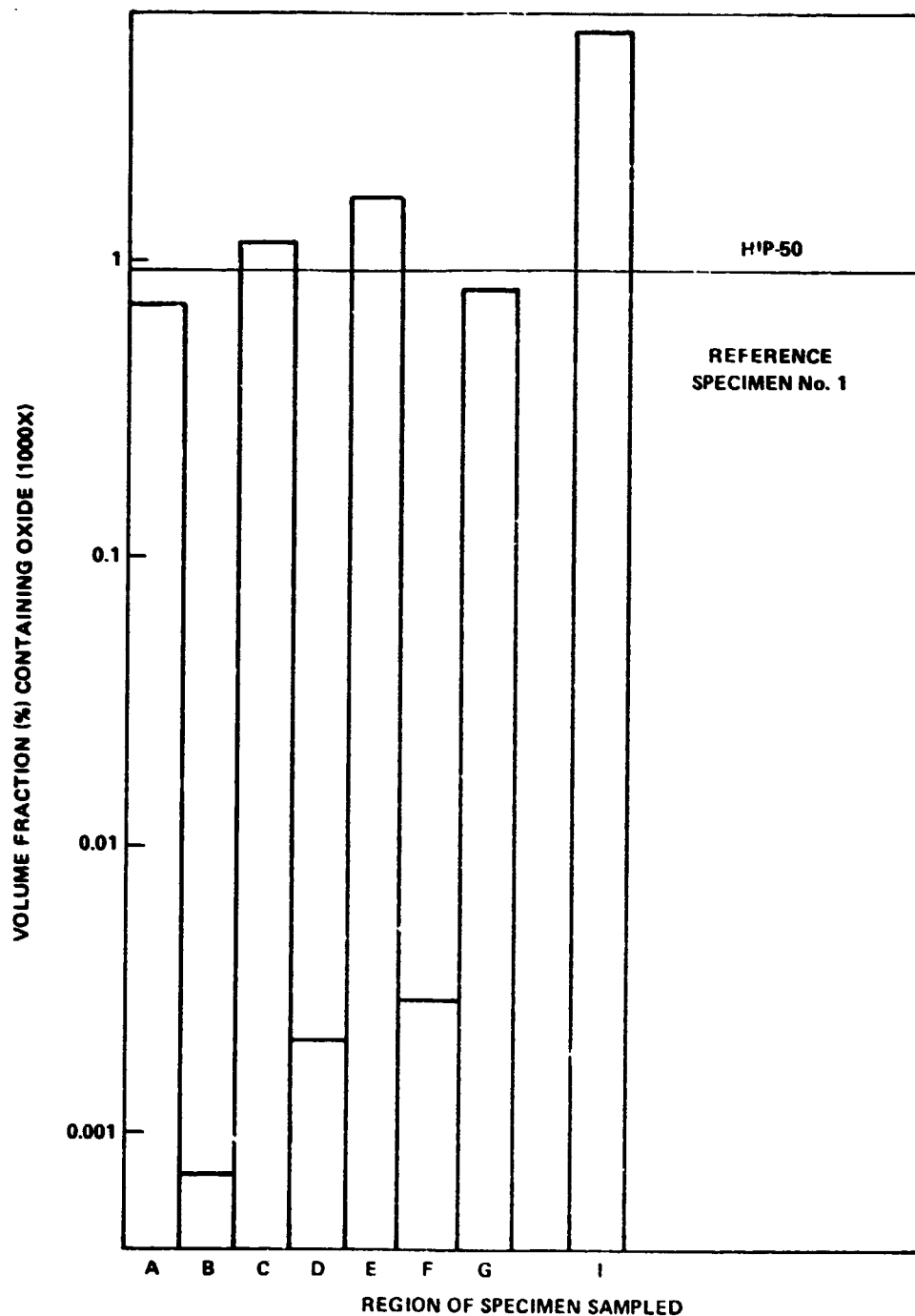


Figure 25. Oxide volume fraction produced from Quantimet Analysis of 1000X SEM micrographs for ground based reference specimen No. 1 after normalization to total volume fraction occupied by each type of BeO structure exhibited and to the initial distribution before melting.

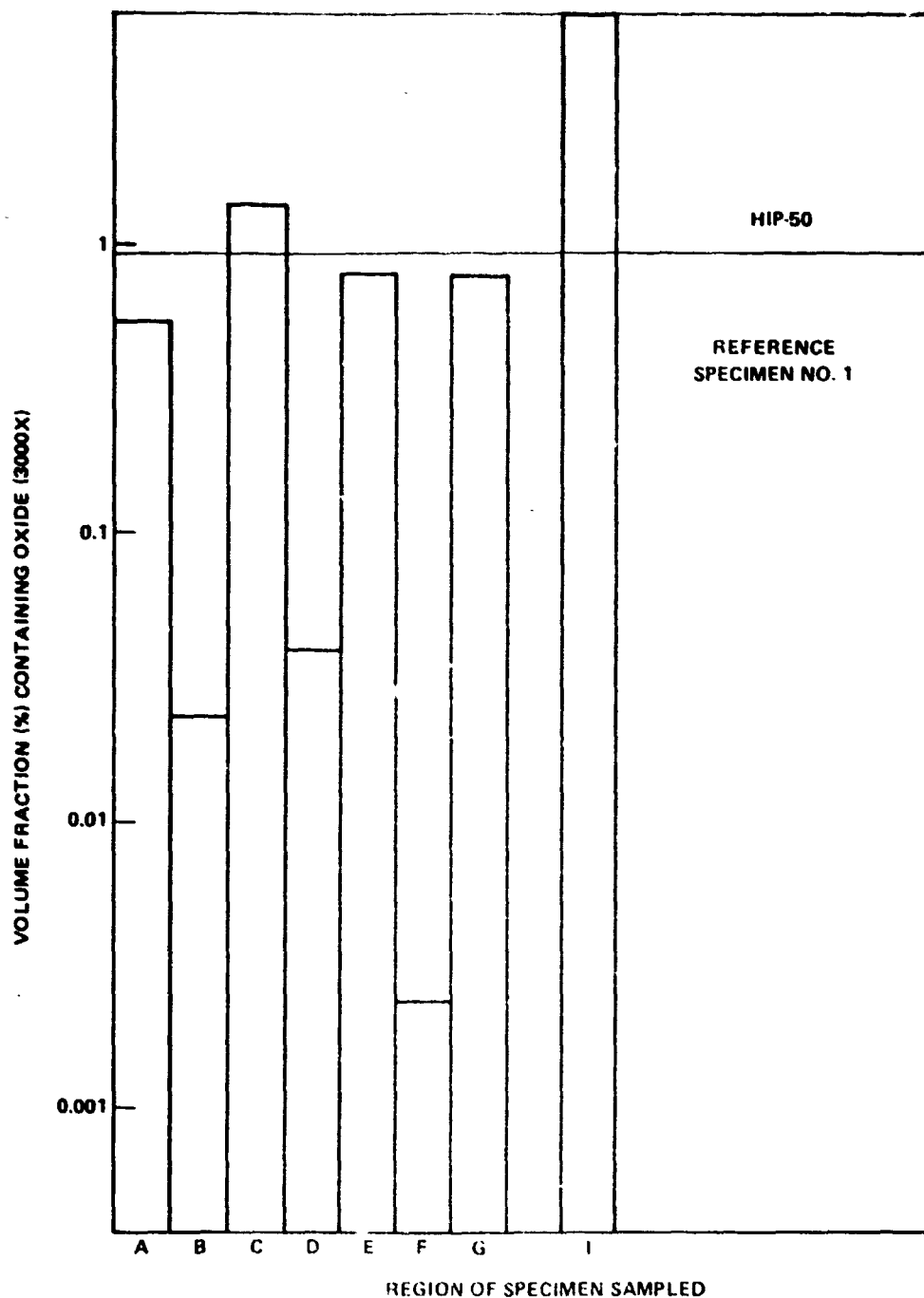


Figure 26. Oxide volume fraction produced from Quantimet Analysis of 3000X SEM micrographs for ground based reference specimen No. 1 after normalization to total volume fraction occupied by each type of BeO structure exhibited and to the initial distribution before melting.

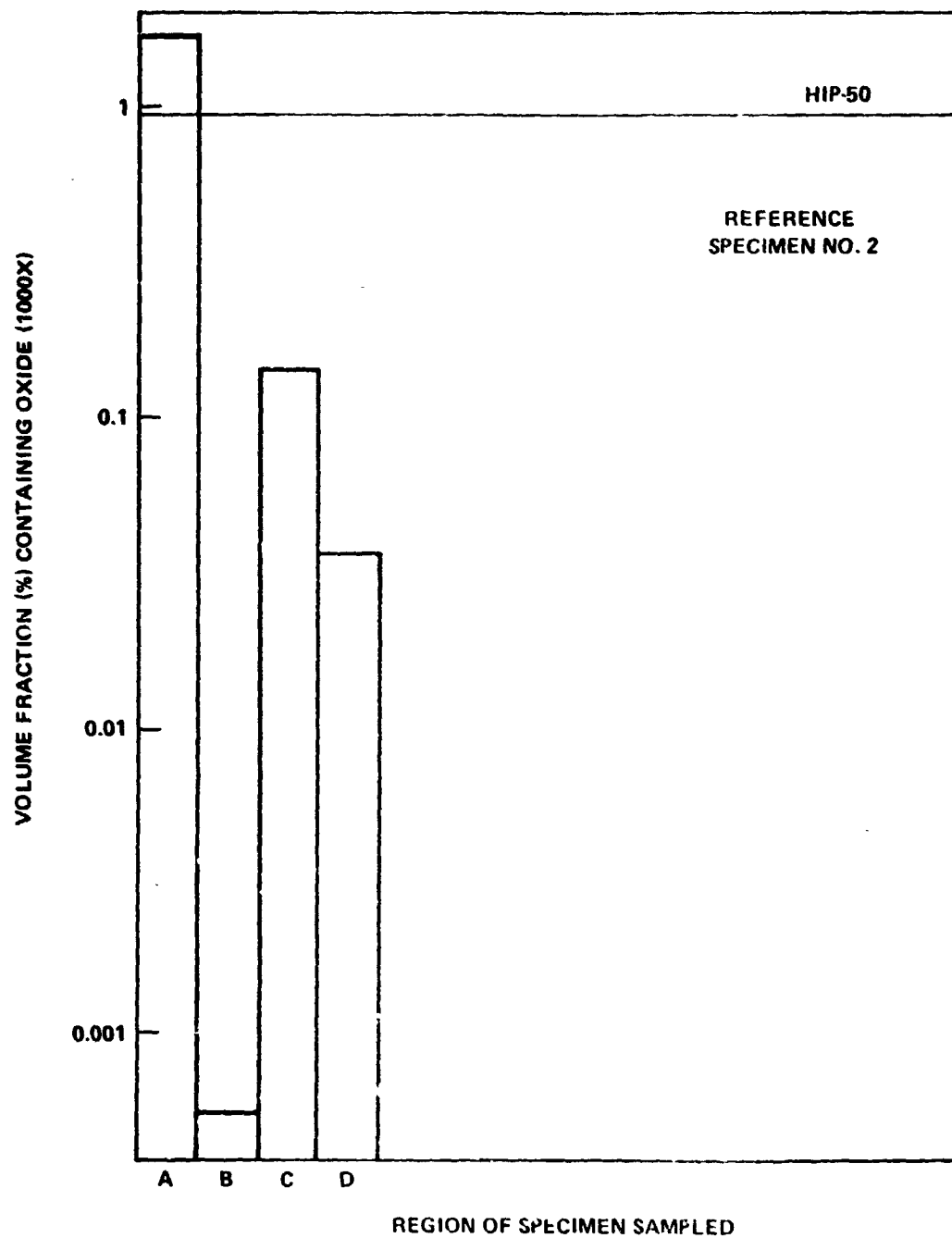


Figure 27. Oxide volume fraction produced from Quantimet Analysis of 1000X SEM micrographs for ground based reference specimen No. 2 after normalization to total volume fraction occupied by each type of BeO structure exhibited and to the initial distribution before melting.

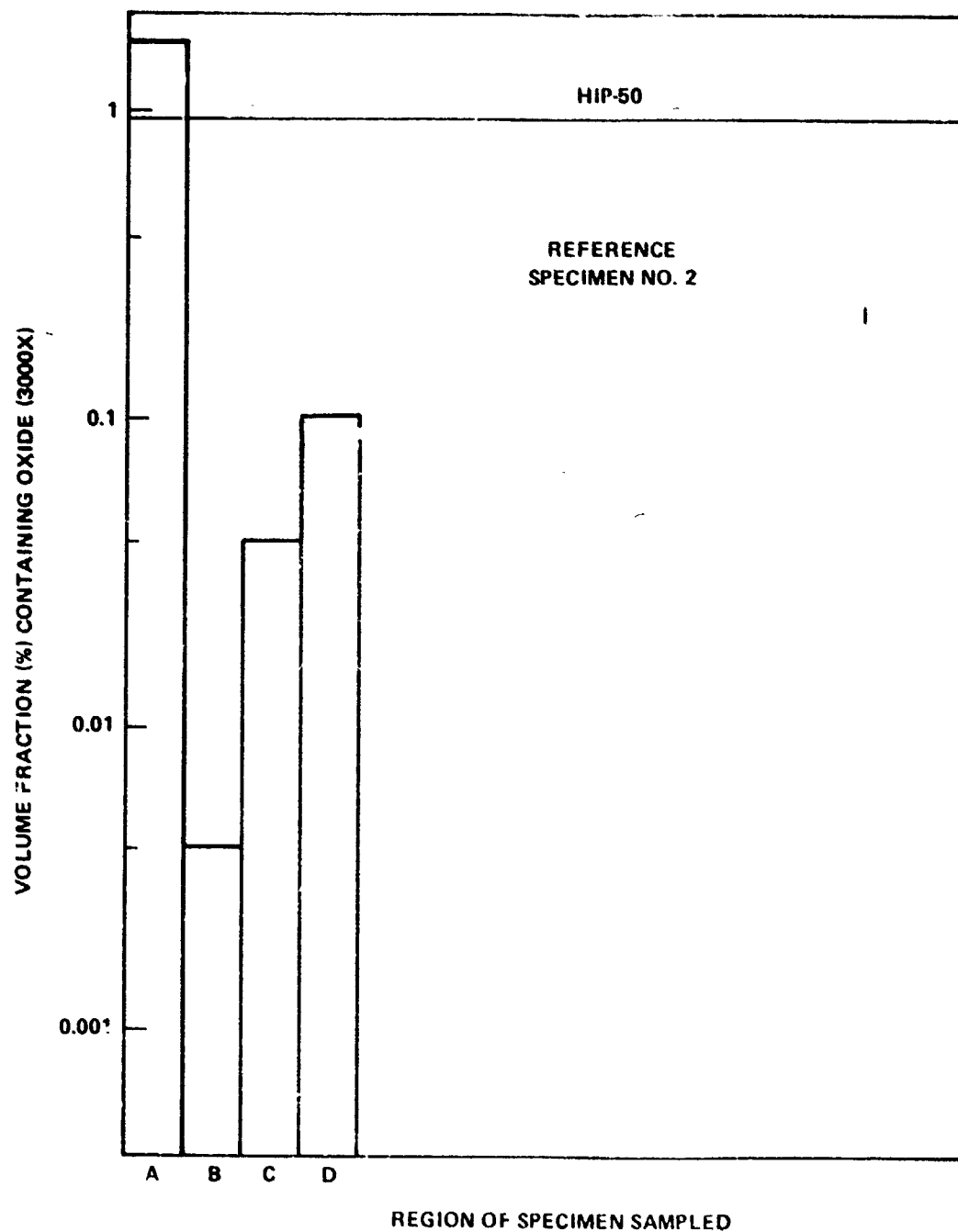


Figure 28. Oxide volume fraction produced from Quantimet Analysis of 3000X SEM micrographs for ground based reference specimen No. 2 after normalization to total volume fraction occupied by each type of BeO structure exhibited and to the initial distribution before melting.

TABLE 3. MAJOR EVENT RECORD

t	t - 50.5	Event
0	0	Launch signal
50.5	0	Power on, specimen oscillations noted
85.9	35.4	First reading from solid state pyrometer
94	43.5	Solid state pyrometer reaches asymptotic reading nearly in saturation
121.3	70.8	Shape oscillation signal completion of melting
139.4	88.9	Power reduction signal (33%), battery voltage increase
159.7	109.2	Initiation of low powered positioning mode
169	118.5	Attainment of low powered mode
261	210.5	Loss of telemetry signals



Figure 29. Specimen side view after recovery showing equatorial and polar bulge, and surface penetration of shrinkage cavity.



Figure 30. Specimen end view
with shrinkage cavity.



Figure 31. Oblique view from approximate
angle of view by movie camera.

ORIGINAL PAGE IS
OF POOR QUALITY

Some of the external markings on the specimen apparent in Figures 30 and 31 may be indentations caused by the r.f. work coil. It is obvious from both the telemetry data and the movie record that the specimen did not contact the coil until after it had cooled below a dull red heat, except, possibly, at the instant of sudden shape change at the moment of complete melting. The stiff oxide coating would have retained these markings. After the specimen had cooled below the self-luminescence temperature (during reentry), forces between the specimen and the coil would not have been sufficient to cause such indentations, because the only available force would have been the inertia of the specimen which could have reached only approximately 70 gm under an assumed 70 g rocket impact.

During the experiment a record of the events were recorded on film by the motion picture camera provided, and temperature-time data were recorded by telemetry signal from the flight pyrometer. Since the pyrometer temperature range was not sufficiently broad to include the superheat region, this portion of the record was not obtained. The measured melting interval and cooling curve will be discussed in Appendix A.

Telemetry and motion picture records show that the ECPP performed well the task of heating, melting, and positioning the specimen. This is discussed in detail in the NASA Contract No. NAS8-30797 final report. Aside from possible initial contact with the coil during the shape change upon melting, the specimen was not at any other time in contact with the coils and was stably positioned while molten. The experiment proceeded in all essential aspects as planned. The results are discussed in the following test.

Grain Size and Morphology

In addition to the surface shape and markings described elsewhere in this report, macro study revealed the presence of a single shrink hole and many surface cracks (Fig. 29). Study of the microstructure (Figs. 32 and 33) revealed a relatively large average grain size of 700 μm , porosity, and twinning and cracking. Although twinning can be induced during sectioning, it is most unusual that of the 17 large grain sized specimens sectioned, the flight specimen was the only one cracked and twinned.

With the very large grain size evident in the flight specimen, neither grain refinement of the cerium nor retardation of grain growth was obtained, although detailed analysis of the dispersion of BeO showed that the BeO was unagglomerated and uniformly dispersed throughout the melt. This will be



Figure 32. Typical microstructure exhibited in flight specimen.
Taken with polarized light.

ORIGINAL PAGE IS
OF POOR QUALITY



Figure 33. Bright field micrograph of flight specimen showing a
crack running in from surface and voids produced.
Magnification 100X.

discussed in a later section. It must be concluded, in light of the previously mentioned results, that the BeO did not act to refine the grain structure and that the minimum criterion of improved microstructure through obtaining a fine grained casting (grain size less than $100\text{ }\mu\text{m}$) was not obtained.

Oxide Particle Distribution

Figure 34 is a montage of 30X SEM micrographs of the flight specimen after sectioning and metallographic preparation. It is evident that there are no cleared out regions devoid of oxide in the flight specimen. There is a darker band with less oxide present, but Quantimet Analysis shows that there is still considerable oxide present in this region. Figures 35 through 38 show the oxide distribution at magnifications of 1000X, 3000X, 10 000X, 30 000X, respectively, in the lighter region and Figures 39 through 42 that in the darker region. Plots of the volume of oxide for different regions at 1000X and 3000X, respectively, obtained by Quantimet Analysis are shown in Figures 49 and 50. It is evident that even in the darker region, the oxide level is high although below that of the HIP-50 powder metallurgy starting material.

It can be seen that the oxide networks are made up of oxide particles in size ranging from 0.02 to $1.3\text{ }\mu\text{m}$. Figures 43 through 46 show the oxide distribution typical to the HIP powder metallurgy material at magnifications 1000X, 3000X, 10 000X, and 30 000X, respectively. It is evident that the oxide networks in the darker region of the flight specimen are most like those of the starting material, even though the flight specimen is coarse grained and the powder metallurgy material very fine grained. This is a very encouraging result as in this region the oxide network structure did not change much, even though the specimen was molten. It will be observed that the volume fraction results obtained by Quantimet could be plotted on linear graph paper. There are no cleared out areas devoid of oxide. There are also no very white areas with heavily agglomerated oxide. In every region of the specimen there is appreciable oxide content and no gross agglomeration and separation are evident.

It was determined by microprobe analysis (SEM microprobe attachment) that silver flakes are present in the specimen surface oxide coating, and there are silver inclusions on the sectioned surface of the flight specimen. These are shown in Figures 47 and 48, respectively. It was determined that the silver inclusions were a polishing artifact on the following basis:

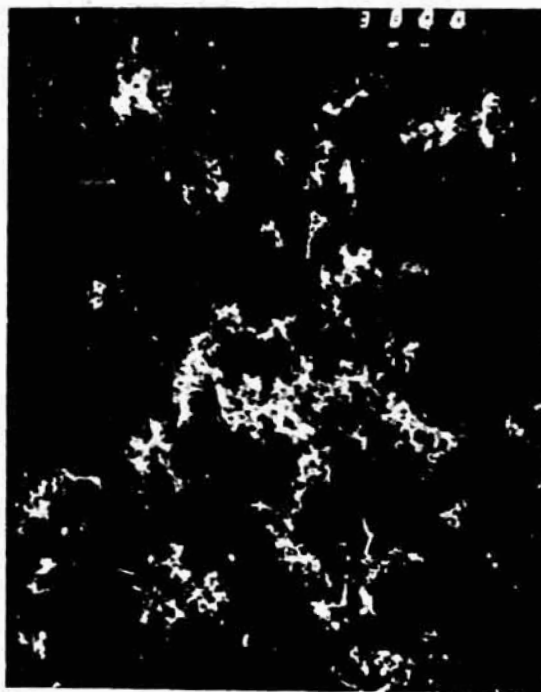
1. The silver particles are sharp faceted. Had they been present in the molten beryllium, they would have either gone into solution in the beryllium or been spherodized.



Figure 34. Montage of 30X SEM micrographs of flight specimen, reduced to size for reproduction. Dark region at left is silver paint used for SEM analysis. Specimen exhibits a lighter and darker region but no heavily agglomerated region or cleared out region.



Figure 35. SEM micrograph of lighter region of flight specimen at 1000X.



**ORIGINAL PAGE IS
OF POOR QUALITY**

Figure 36. SEM micrograph of lighter region of flight specimen at 3000X.



Figure 37. SEM micrograph of lighter region of flight specimen at 10 000X.



ORIGINAL PAGE IS
OF POOR QUALITY

Figure 38. SEM micrograph of lighter region of flight specimen at 30 000X.



Figure 39. SEM micrograph of darker region of flight specimen
at 1000X magnification.

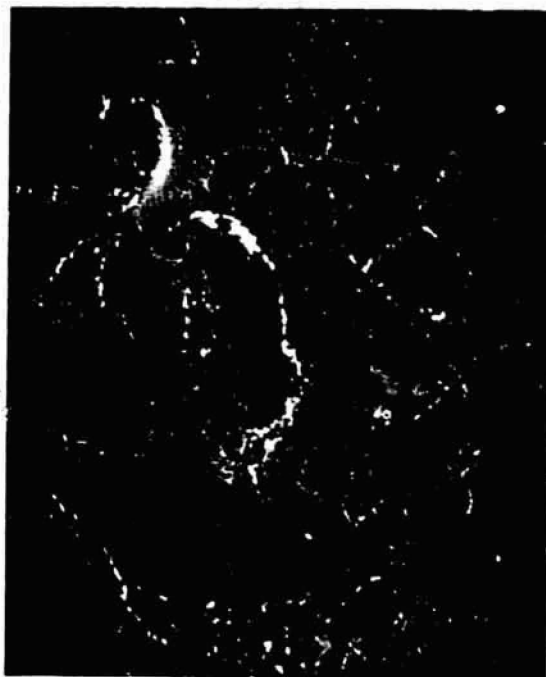


Figure 40. SEM micrograph of darker region of flight specimen at 3000X magnification.

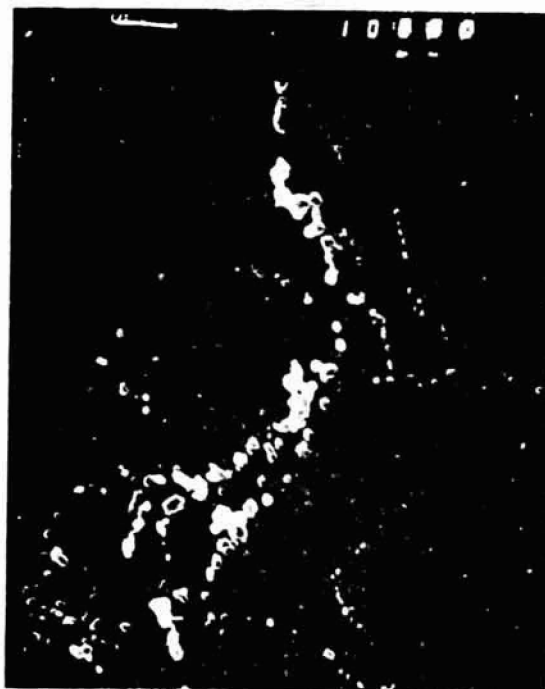


Figure 41. SEM micrograph of darker region of flight specimen at 10 000X magnification.



ORIGINAL PAGE IS
OF POOR QUALITY

Figure 42. SEM micrograph of darker region of flight specimen at 30 000X magnification.

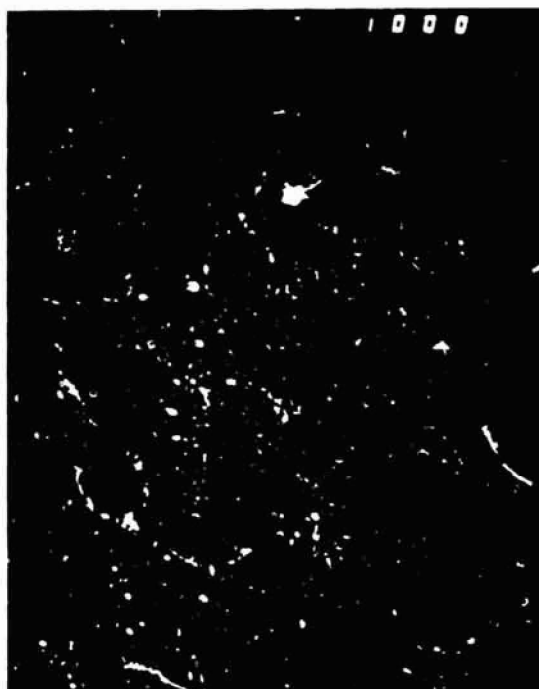


Figure 43. SEM micrographs of initial oxide distribution before melting in HIP-50 alloy at 1000X magnification.

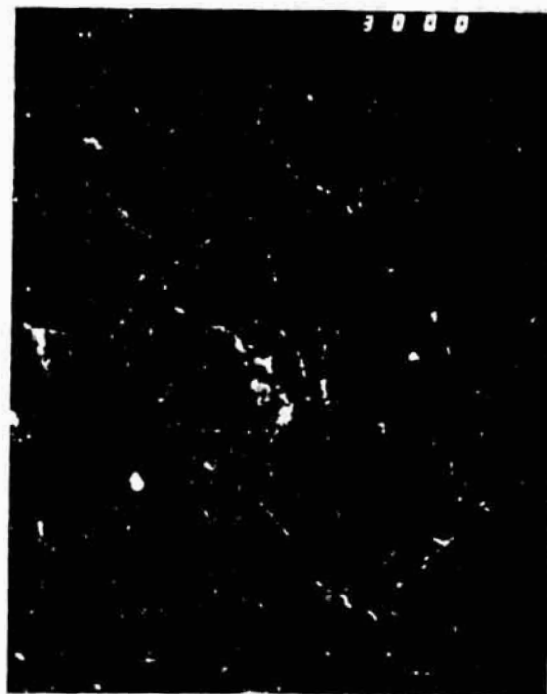


Figure 44. SEM micrographs of initial oxide distribution before melting in HIP-50 alloy at 3000X magnification



Figure 45. SEM micrographs of initial oxide distribution before melting in HIP-50 alloy at 10 000X magnification.



ORIGINAL PAGE IS
OF POOR QUALITY

Figure 46. SEM micrograph of initial oxide distribution before melting in HIP-50 alloy at 20 000X magnification.



Figure 47. Silver flakes on surface oxide coating of specimen.
Magnification 300X.



Figure 48. Silver inclusions in specimen.
Magnification 2000X.

2. A transverse section to the section where they are present did not reveal any silver inclusions in the specimen. The silver on the specimen surface oxide coating is not a polishing artifact but also had to be deposited after solidification. Otherwise it would have dissolved in the beryllium or spheroidized on the surface (silver melts at 961°C).

Most of the solder used in the ECPP contains silver and, while still hot but solid, the specimen rattled around in the coils and the ECPP was shaken considerably during the reentry and impact with the ground. The silver in the form of flakes was deposited on the specimen during this period and was not present during the experiment and is believed to have had no effect on the experiment.

ANALYSIS OF EXPERIMENTAL RESULTS

An examination and comparison of the Quantimet plots of volume fraction of BeO for different regions of the ground based specimens and the flight specimen (Figs. 27, 28, 29, 30, 49, 50) show the flight specimen is much more

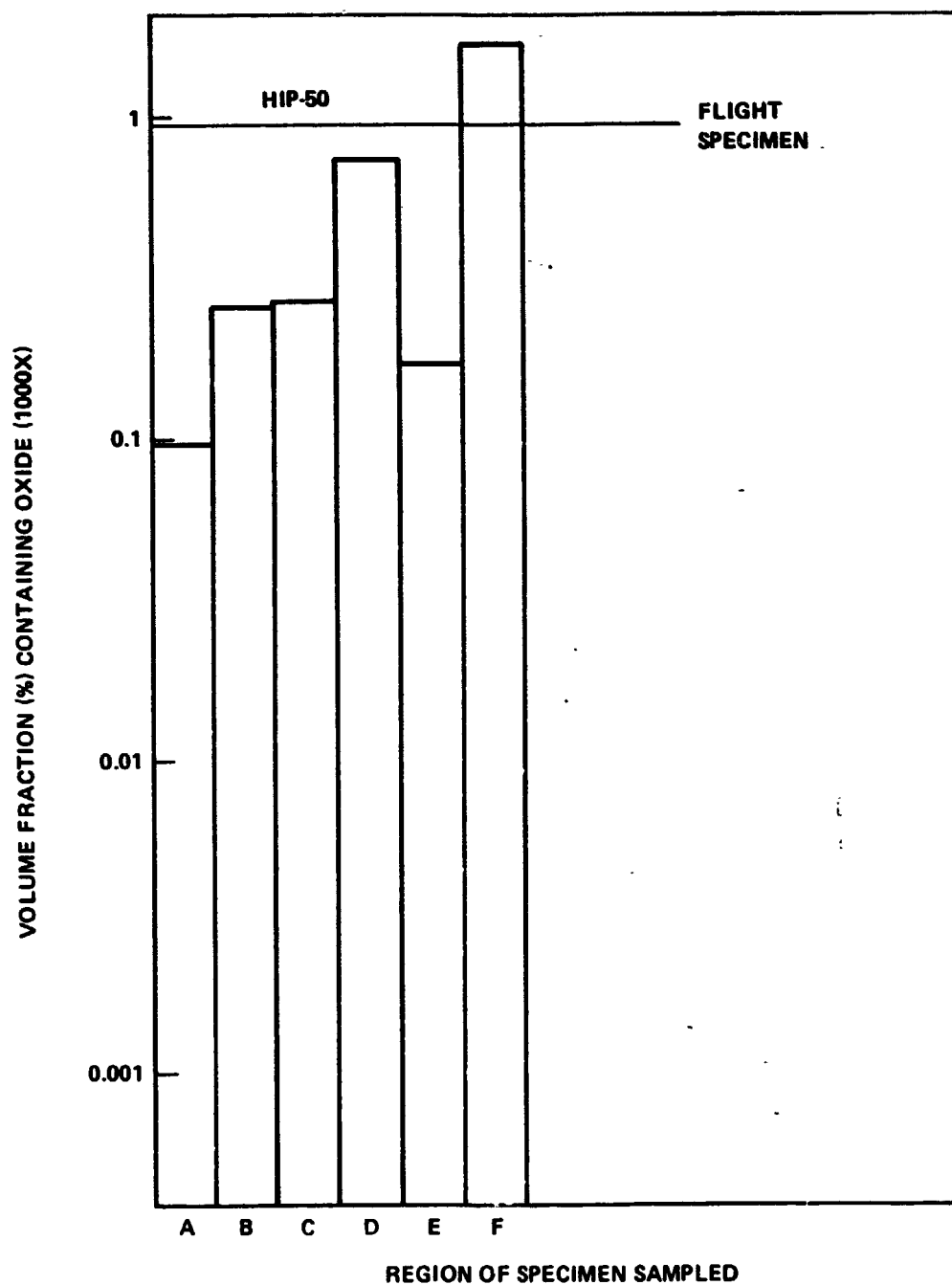


Figure 49. Oxide volume fraction produced from Quantimet Analysis of 1000X SEM micrographs for flight specimen No. 1 after normalization to total volume fraction occupied by each type of BeO structure exhibited and to the initial distribution before melting.

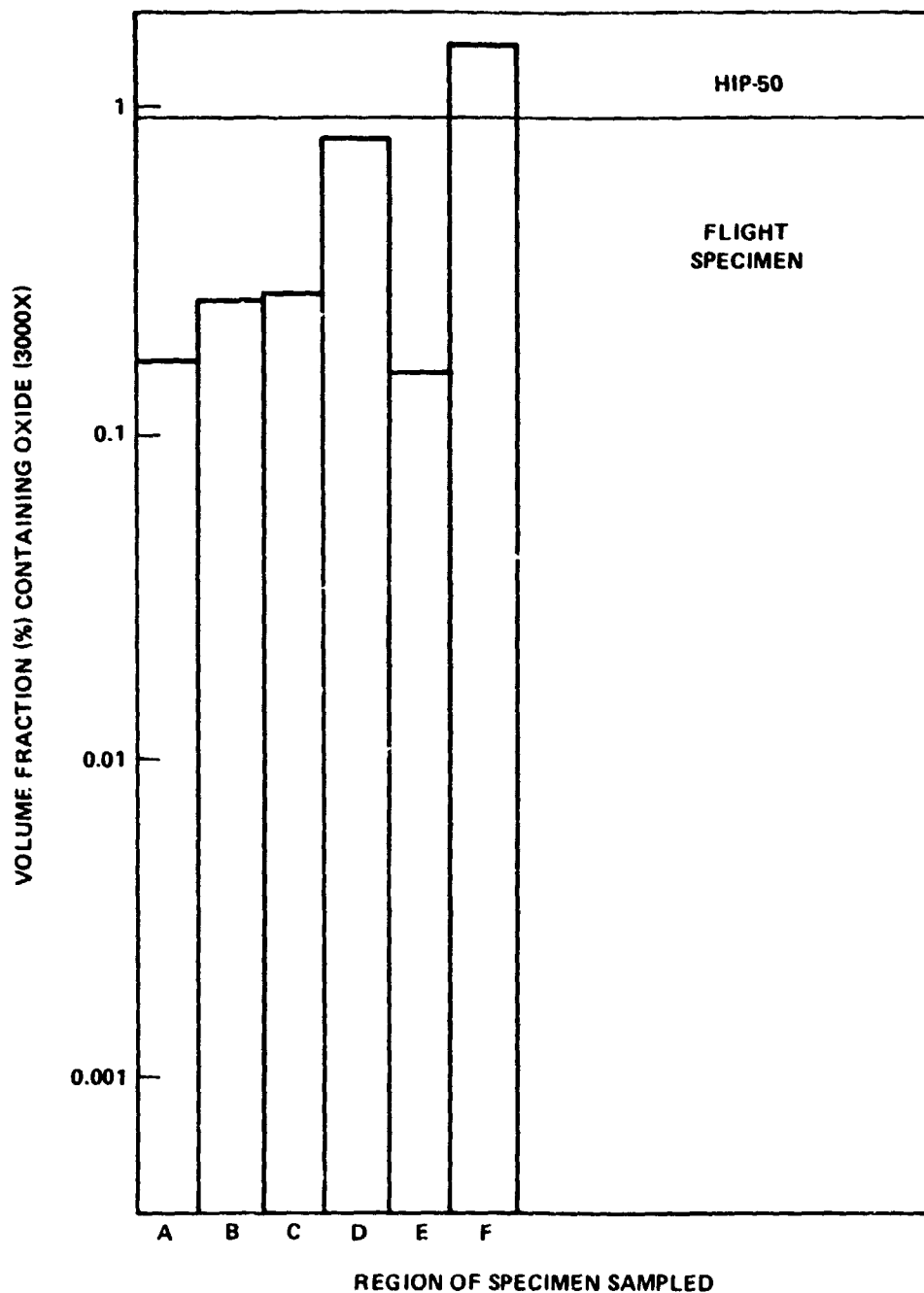


Figure 50. Oxide volume fraction produced from Quantimet Analysis of 3000X SEM micrographs for flight specimen No. 1 after normalization to total volume fraction occupied by each type of BeO structure exhibited and to the initial distribution before melting.

uniform in oxide distribution from the ground based specimens. The flight specimen has no regions devoid of oxide or regions filled with oxide as has both ground based reference specimens. The reason for this is postulated to be the weightless environment of space, where the g-level has been reduced to 10^{-4} g during the melting and solidification. The Stokes collisions (Appendix B) are reduced for a given distribution of particle sizes directly in proportion to the reduction in g-level, and the separation time is inversely proportional to the g-level. Hence, on the basis of Stokes collisions alone, the time for agglomeration and separation to occur should be greatly extended in the weightless environment of space.

Collisions due to fluid motion (gradient collisions), which may arise due to stirring, gravity driven convection, or Marangoni convection (surface tension driven convection), act to speed up agglomeration and separation. In the weightless environment of space, gravity driven convection is greatly reduced, but the other sources of fluid motion are not. What this experiment indicates is that the major mechanism for agglomeration and separation of BeO from the melt may be Stokes collisions, as the stirring forces and Marangoni convection are essentially the same in the ground based and flight experiments.

The coarse grain size of the ground based reference specimen and the flight specimen indicate that the BeO present did not act as a grain refining agent for beryllium or that after solidification it did not prevent excessive grain growth while still at high temperatures. Returning to the criteria previously stated for a good grain refining agent, possible reasons for this are either the particles are not stable in the melt, do not possess a maximum of surface area, or do not have optimum surface character. Examination of the oxide networks in the HIP-50 alloy (Figs. 43 to 46) shows that even before melting, the particles tend to be rounded and without sharp facets. It may be possible that as a result of the long molten dwell, the particles change their surface character as well and become inactive as sites for heterogeneous nucleation; however, this could not be observed at 30 000X. An optimum surface character [1] might be a rough or pitted surface.

Prevention of excessive grain growth after solidification, while still near the melting point, depends greatly on the oxide particle size. While the HIP-50 alloy has stability against grain growth temperature almost to the melting point of beryllium, further agglomeration while in the molten state (even in the weightless environment) could lower the stability temperature significantly. Work reported [2] indicates that the finest particle size attainable is required to prevent grain growth at temperatures near the melting point ($0.065 \mu\text{m}$ median particle size). Attention must be given to this aspect in future work.

CONCLUSIONS

The experiment results show that it is feasible to obtain a uniform dispersion of BeO in a beryllium casting in the weightless environment of space. This is a new material which, to our knowledge, has not been produced in the terrestrial environment and is of interest both scientifically and technologically. In terms of the minimum criteria for success, those for satisfactory melting and solidification and improved cast microstructure (presence of dispersed oxide phase) were met. The criterion for improved cast microstructure (fine grain size) was not met. The criterion for enhanced service properties has not been met as yet because of failure to achieve an improved cast microstructure (fine grain size).

As a step forward in producing cast beryllium with improved service properties, the material produced delineates an approach to be followed for further research into the action of BeO as a grain refining agent for beryllium. This approach is as follows:

1. To utilize beryllium starting material with nonspherodized BeO particles dispersed throughout. This can be achieved by elimination of the final step in the production of HIP-50, the high temperature dwell at 1950°F (1068°C).
2. To dwell for a much shorter time while molten during the experiment.

Additionally, the experiment should be performed at vacuum (1 torr) to reduce the observed 2 to 5 percent porosity in the casting.

If a subsequent experiment with BeO particles that are not spherodized is performed and grain refinement does not result, then serious questions are raised concerning the ability of BeO to act as a grain refining agent. In that event, the weightless environment of space is ideal to test the potential of several other additions as grain refiners. One such addition is titanium, which forms a beryllide in the melt. Attempts to utilize titanium as a grain refining agent may have failed terrestrially also because of agglomeration and separation of the beryllide from the melt. Another such addition would be tungsten.

Failure to achieve grain refinement with a particular agent, chosen on the basis of lattice registry, may mean that other factors are of overriding consideration such as surface area or surface character or grain growth after solidification. If grain growth is so rapid that grain refinement is not achieved, then the number of nucleating particles becomes of great importance rather than

surface area or surface character. In that case, so many particles may be required that mechanical properties may be greatly impaired even with grain refinement. Testing of all of these factors is important to explaining why or why not an agent is successful as a grain refiner. Such experiments conducted in the weightless environment are the only practical methods of testing these hypotheses, as terrestrially agglomeration and separation are encountered.

APPENDIX A

THERMAL ANALYSIS

Although the flight pyrometer was in saturation during the melting and molten dwell, enough data were obtained from the telemetry records and the cooling curve to reconstruct the heating, melting, and cooling profile. The flight record of events was presented in Table 3. The heating and cooling curves obtained from the flight pyrometer are shown in Figures A-1 and A-2. From analysis of the data available, the temperature-time curve shown in Figure A-3 was constructed. The solidification time after power down was 28 ± 5 , -0 s.

A computer model of the solidification of the beryllium specimen was exercised to determine whether or not the assumptions made about how the beryllium specimen solidified were reasonable. This model assumes that the specimen solidifies inward from the surface, losing heat at the surface by radiation. The remaining liquid at any time is assumed to be well mixed and at the melting temperature. Outputs from the program are: (1) the advance of the solidification front in time and (2) the decrease in surface temperature with time. The program can treat a sphere, a cylinder, or a slab. As the remaining liquid is isothermally at the melting temperature, heat is extracted through the solid crust to the surface, where it is lost. Figures A-4 through A-9 show the results of calculations for a sphere of 0.922 cm diameter, a cylinder of 0.922 cm diameter, and a slab of 0.922 cm thickness.

Comparisons with the experimental curve shown in Figure A-3 show that the calculated time that agrees closest is for the spherical geometry, but the shape of the cooling curve is closest to that of the slab. The calculated solidification time for the sphere is 31 s, which is within the error of determination of the time for solidification experimentally. As the shape of the specimen is spheroidal with an equatorial bulge, its geometry is closest to that of the sphere; consequently, the agreement in solidification time is reasonable. The location of the shrinkage cavity shows that the specimen did not solidify symmetrically as is assumed for the calculation. This is the hypothesized reason for the disagreement in the shape of the cooling curve, which is closest to that of the slab geometry.

As the computer model uses the known values of thermal conductivity, latent heat of fusion, and emissivity for molten beryllium (emissivity for oxidized beryllium), the results indicate that it might be possible to extract

thermodynamic data from solidification curves of levitated metals if the shape of the specimen and the details of solidification are known. This might be accomplished through the use of an imaging array pyrometer to simultaneously display the specimen and follow the solidification front.

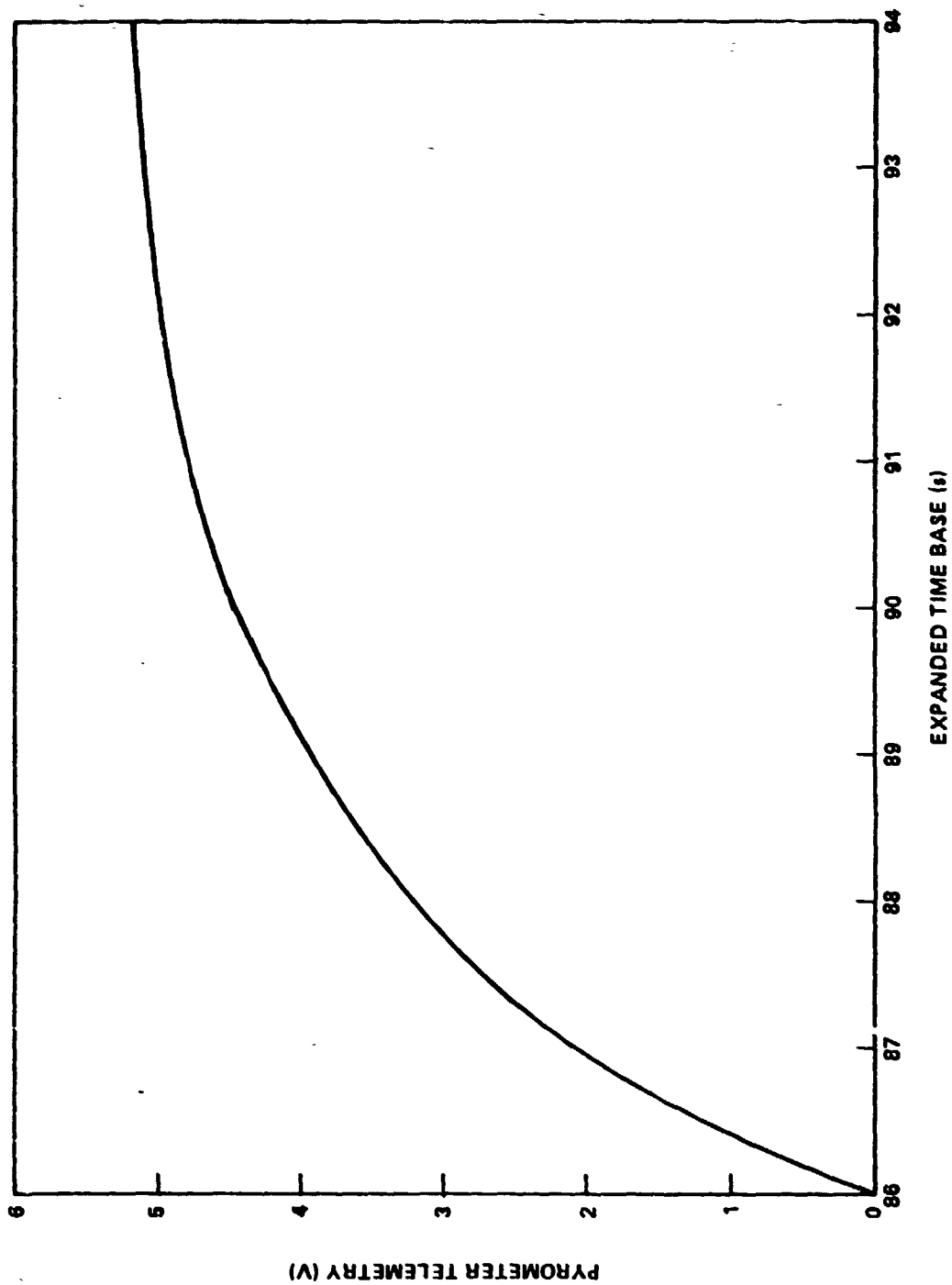


Figure A-1. Pyrometer telemetry signal, heating curve.

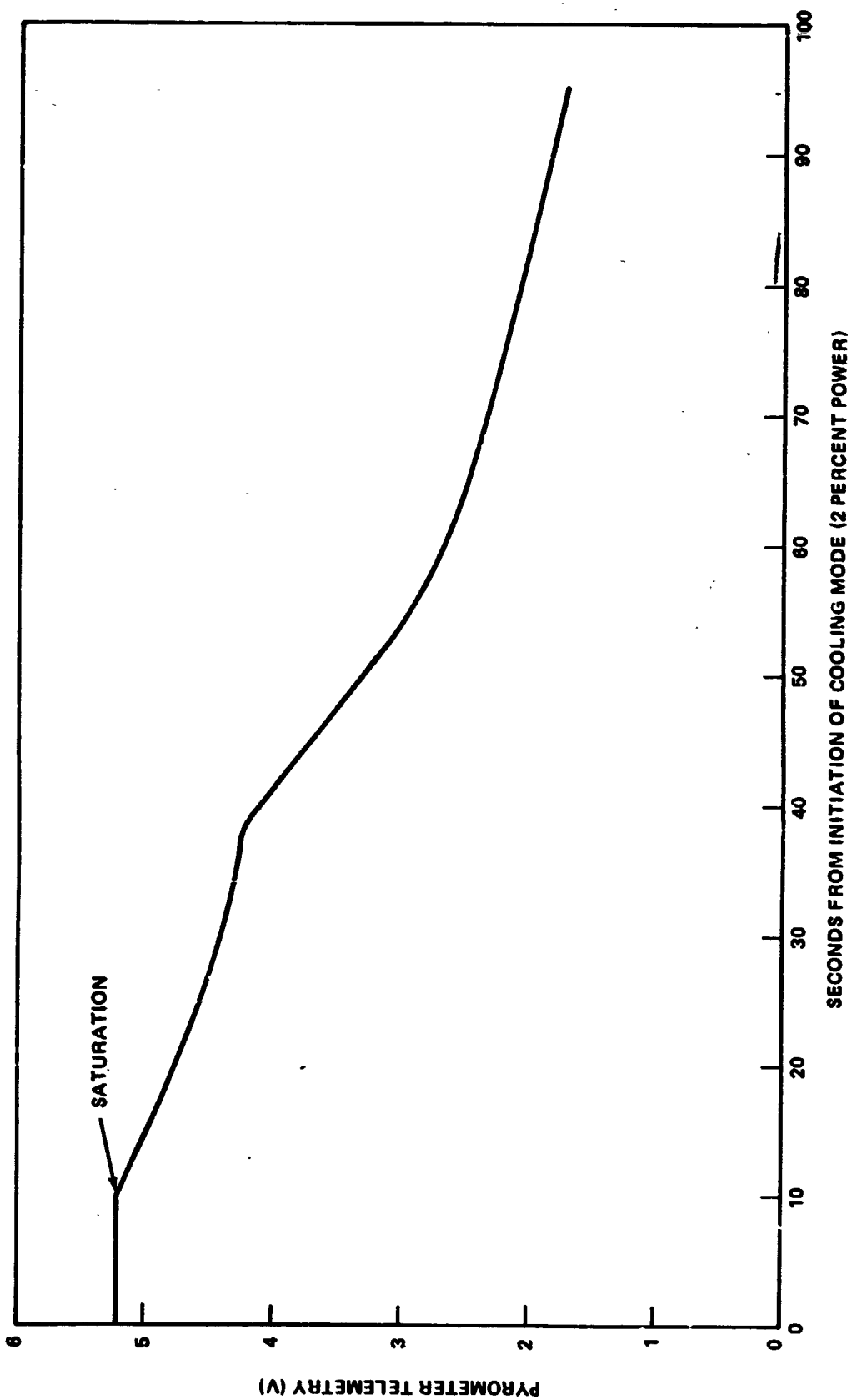


Figure A-2. Pyrometer telemetry signal, cooling curve.

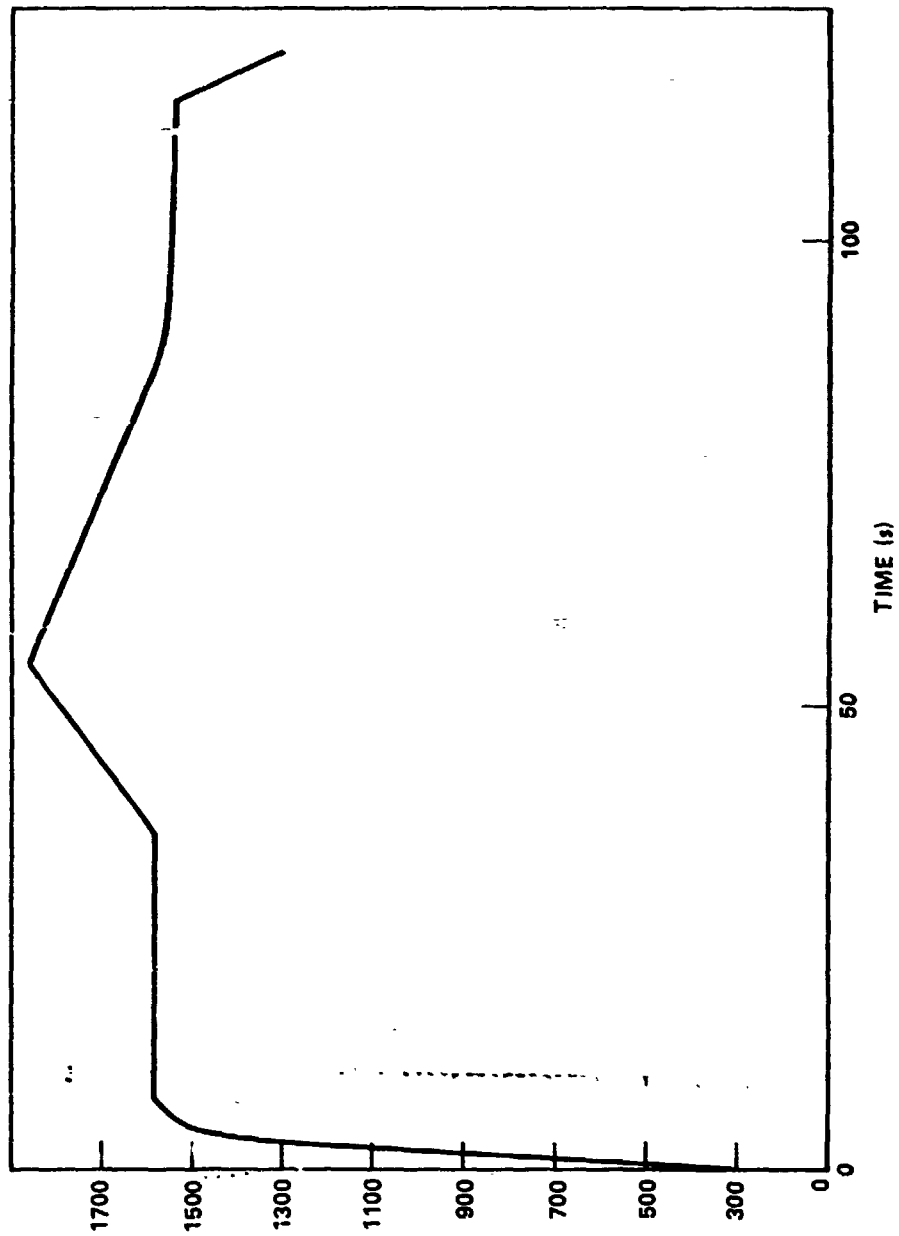


Figure A-3. Temperature-time curve for flight specimen.

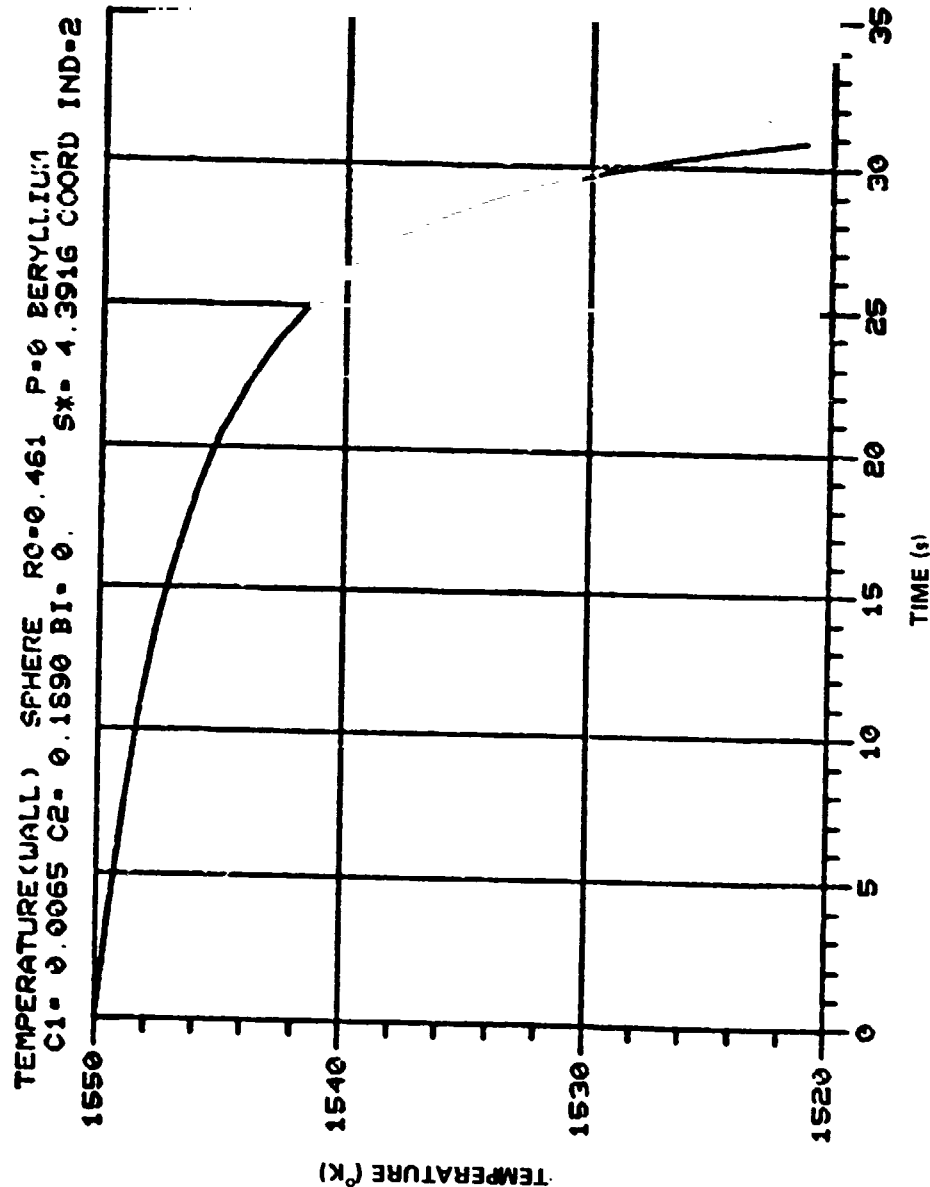


Figure A-4. Temperature (wall) for a sphere 0.922 cm in diameter.

SOLIDIFICATION FRONT SPHERE R0=0.461 P=0.125 YLLIUM
 C1=0.0065 C2=0.1890 BI=0 SX=4.3316 COORD IND=2

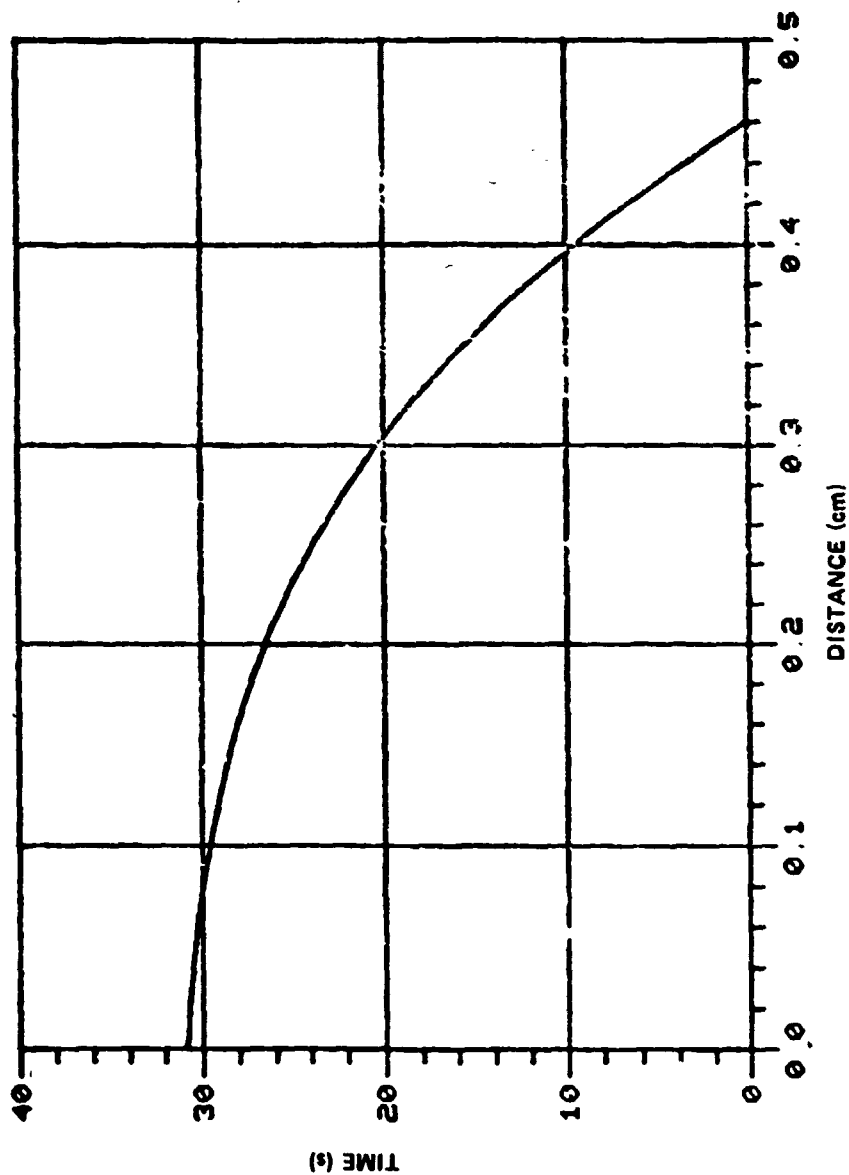


Figure A-5. Solidification front for a sphere 0.922 cm in diameter.

TEMPERATURE (WALL) BERYLLIUM CYLINDRICAL COOP P0-0 461 P-0
C1- 0 0065 C2- 0 1890 B1- 0 SA- 4.3916 COORD IND-1

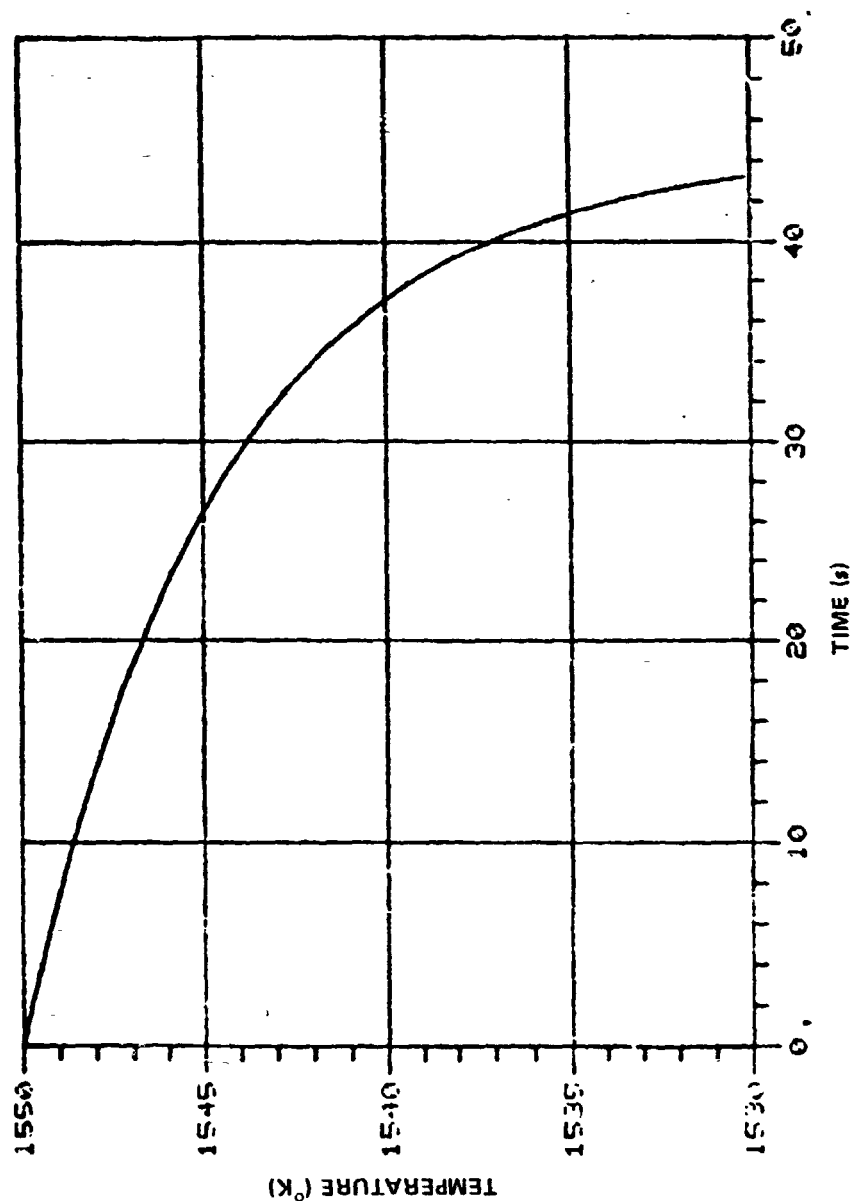


Figure A-6. Temperature (wall) for a cylinder 0.922 cm in diameter.

SOLIDIFICATION FRONT BERYLLIUM CYLINDRICAL COOR RO-0.461 P-0
 CI-0 0055 C2-0 1330 BI-0 SY-4 3916 COOPD IND-1

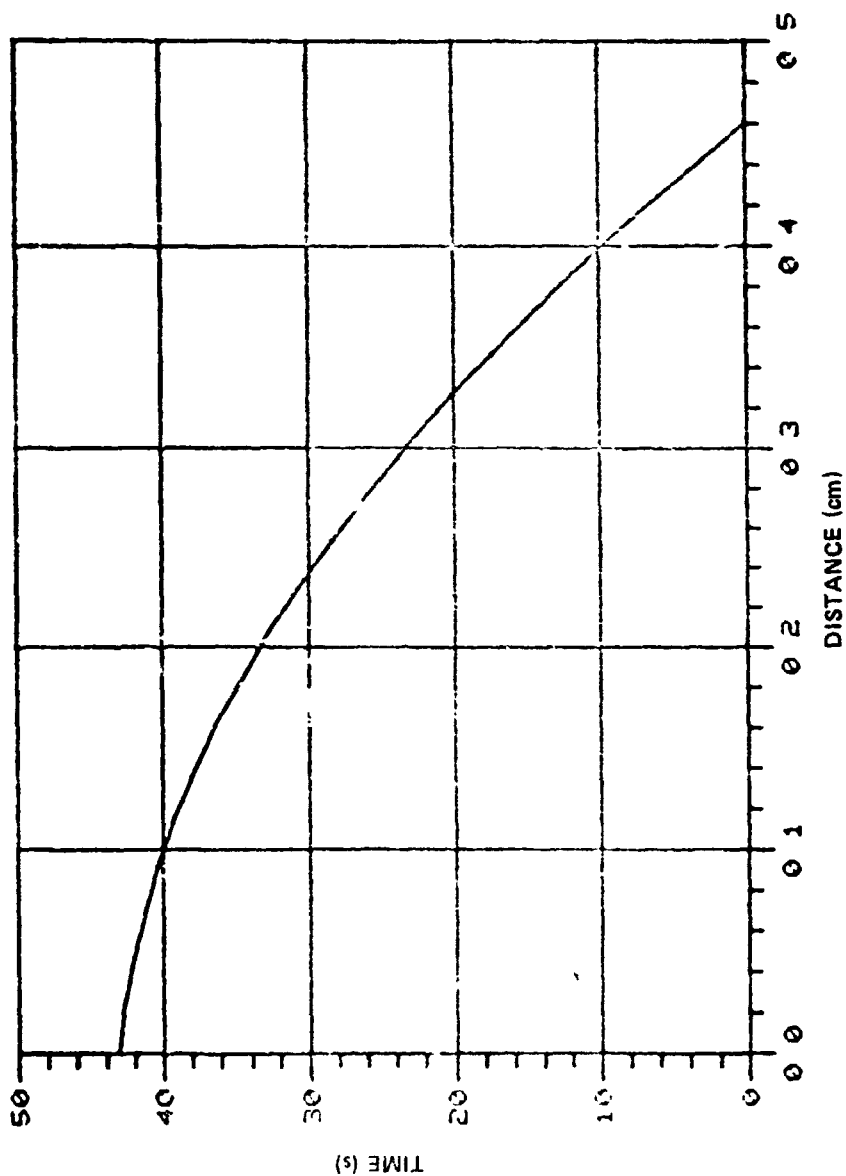


Figure A-7. Solidification front for a cylinder 0.922 cm in diameter.

TEMPERATURE(WALL) CARTESIAN COOR R0=0.461 P=0 BERYLLIUM
C1= 0 0065 C2= 0 1890 DI= 0 SX= 4.3916 COORD IND=0

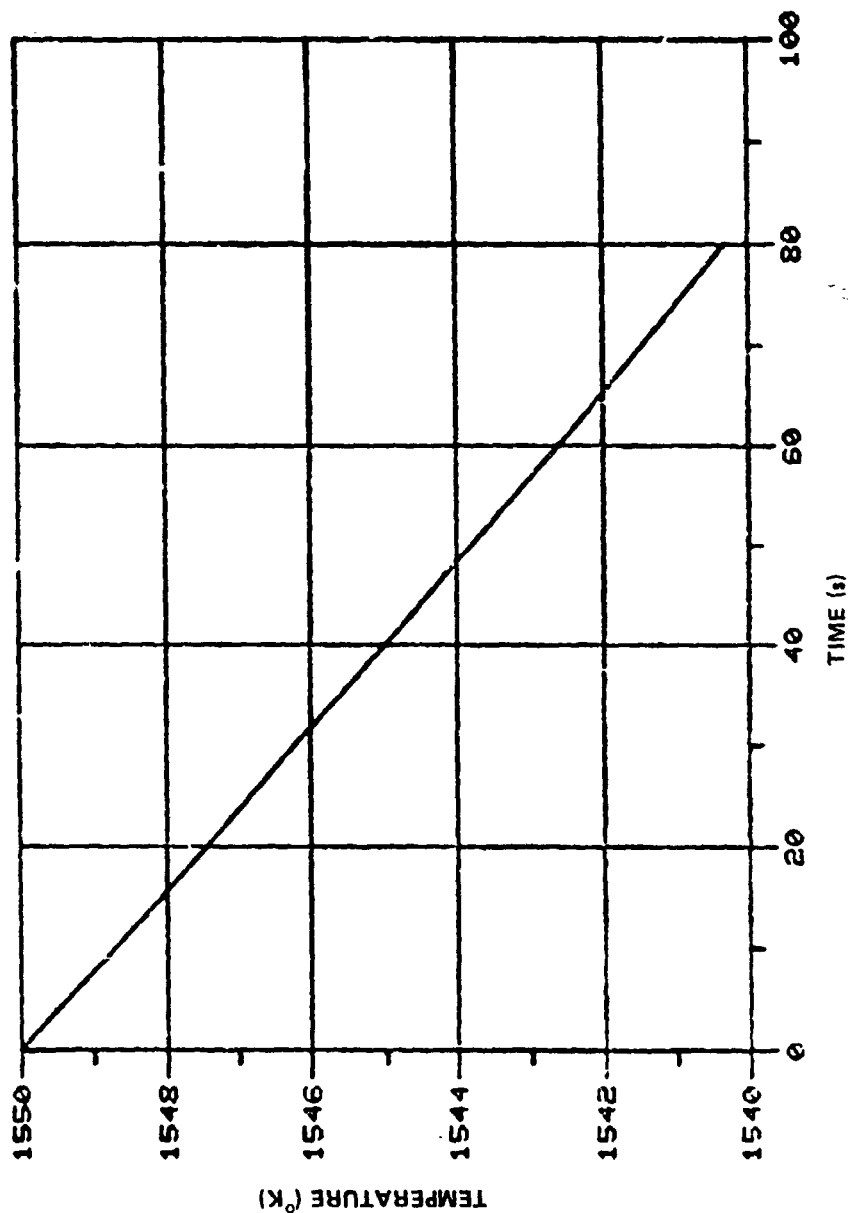


Figure A-8. Temperature (wall) for a slab 0.922 cm thick.

SOLIDIFICATION FRONT CARTESIAN COOR RO=0.461 P=0 PERYLLIUM
 C1= 0.0065 C2= 0.1890 BI= 0. SX= 4.3916 COORD IND=0

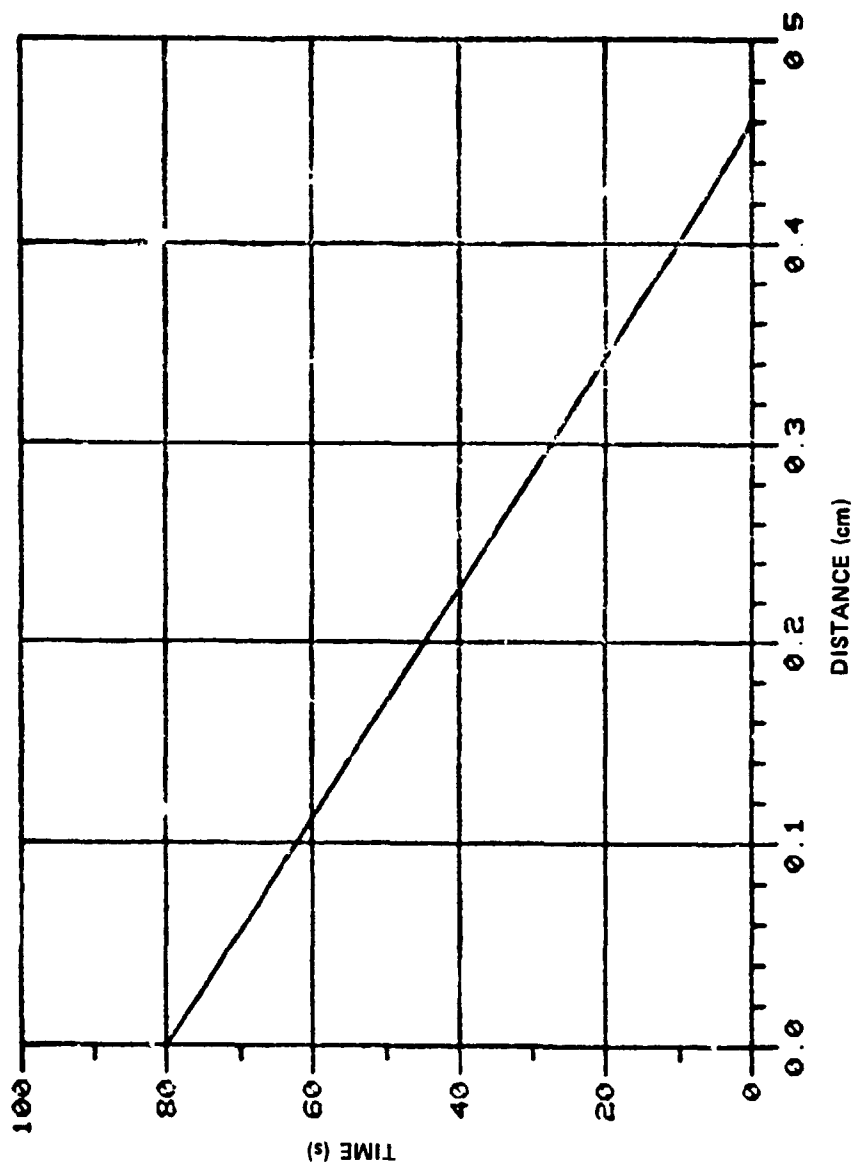


Figure A-9. Solidification front for a slab 0.922 cm thick.

APPENDIX B

AGGLOMERATION AND SEPARATION OF BERYLLIA FROM BERYLLIUM MELTS

Agglomeration and separation are hypothesized to occur primarily due to collisions between BeO particles in the melt. These collisions occur due to (1) the settling of BeO particles due to their density difference in the melt and (2) fluid motion sweeping BeO particles together. The first is called Stokes collisions. The larger BeO particles, settling fastest, collect smaller particles. The second is called velocity gradient collisions and collisions occur between particles of equal size as well as particles of unequal size.

Lindborg and Torsell [3] developed a statistical model for these types of collisions. Using their results, agglomeration and separation times of 1 min or less are likely for BeO particles ranging in size from 0.2 to 1.3 μm in specimens of beryllium melted in the terrestrial environment. In the weightless environment of space, where the accelerations due to gravity are reduced by a factor of 10^4 , the frequency of Stokes collisions is reduced proportionately, as the velocity of settling is directly proportional to the acceleration due to gravity. While all fluid motions, i.e. stirring, are not reduced in the weightless environment of space, fluid motion due to gravity driven convection is reduced. Thus agglomeration and separation times might be extended to periods of many hours or days in the weightless environment of space. It is hypothesized that the much more uniform dispersion obtained in the flight specimen due to the reduction in collision frequency for BeO particles in the weightless environment of space.

REFERENCES

1. Flemings, M.C.: Solidification Processing. McGraw Hill, Inc., 1974.
2. Webster, D., Crooks, D.P., and Vidoz, A.E.: The Effect of Oxide Dispersions on the Recrystallization of Beryllium. Met. Trans., vol. 4, 1973, p. 2841.
3. Lindborg, U., Torsell, K.: A Collision Model for the Growth and Separation of Deoxidation Products. Trans. Met. Soc. AIME, vol. 242, 1968, p. 94.
4. Gelles, S.H. and Malik, T.K.: Process Development for Producing Fine-Grain Castings in Space. NASA Contract NAS8-29626, 1975.

CHAPTER VII

CONTACT AND COALESCENCE OF VISCOUS BODIES

Experiment 74-53

By

Donald R. Uhlman

Massachusetts Institute of Technology

INTRODUCTION

The purpose of this investigation is to study the contact and coalescence of viscous and viscoelastic bodies. A number of industrially important or potentially important material processing schemes rely on an understanding of contact and coalescence phenomena. Perhaps the most obvious is the production of ceramic objects by sintering [1]. In most such cases, the principal flow mechanism is creep, not viscous flow [1-3]; nevertheless, the results of this investigation should be of considerable interest. Specifically, recent progress by Ashby and others [3] in clarifying the operative mechanisms (Nabarro-Herring creep, Coble creep, viscous flow), and the time dependences of sintering in various regimes of the parameters encourages the present effort. Our analytical solution [4] of the Nabarro-Herring creep sintering of two spheres of unequal size also encourages our theoretical approaches to the viscous coalescence problem.

The thermal processing of phase separating glasses often involves the contact and coalescence of discrete second phase droplets and is already of some industrial importance [5-7]. Controlling the properties of phase separated glasses by deformation processing of melts which are already phase-separated is an intriguing possibility which has been the subject of a number of development studies [8,9]; here, again, coalescence is important.

The contact, agglomeration, and coalescence of polymeric particles during melt processing under the influence of capillarity, pressure, and shear, is an important industrial problem which would benefit from the proposed study. Polytetrafluorethylene (PTFE, or Teflon) is processed in powder form under heat and pressure, in what is essentially a viscoelastic sintering situation [10], and an improved understanding of contact and coalescence phenomena should be helpful.

In addition to the type of mass transport process involved, sintering is also classified into three stages, the first includes the early stages of neck growth, during which the particles remain distinguishable as individuals. The second stage is that of densification and grain growth. Here, the pores are roughly cylindrical and the necks between particles are quite large. In the final stage, the pores are isolated and approximately spherical in shape.

Kuczynski [11] and Thummler and Thomma [12] have reviewed the various theories for the initial stage of sintering. In general, the rate of initial sintering for a variety of mass transport mechanisms can be written as:

$$\frac{X^n}{a^m} = F(T)t \quad (1)$$

where X is the radius of the neck, a is the radius of the spherical particles, t is the elapsed time, and n , m , and $F(T)$ depend on the mechanism of sintering.

The rate law for viscous sintering is based on the analysis of the coalescence of two spheres by Frenkel [13]. This worker derived the relation:

$$\frac{X^2}{a} = F(T)t \quad (2)$$

where

$$F(T) = \frac{3\gamma}{2\eta} \quad (3)$$

Here, γ is the surface tension and η is the viscosity. This expression for the sintering rate was obtained by equating the decrease in surface energy with the rate of energy dissipation (as heat) due to viscous flow of the liquid. While these results are widely used, the derivation of Frenkel used a very approximate flow field in calculating the energy dissipation (a flow field of simple uniaxial contraction was employed). Further, it is difficult to apply the analysis to the coalescence of spheres of unequal sizes.

The flow field used in Frenkel's derivation is certainly incorrect for the coalescence of spherical particles; but more accurate analytical treatment of the problem is very difficult. One of the major goals of this investigation is a more accurate description of the growth rate of necks between particles for viscous sintering. This theoretical work will be combined with observations of the coalescence of viscous drops under neutrally buoyant and microgravity conditions.

The general form of the rate law, $X^2/a = F(T)t$, has received some experimental verification [14, 15] for viscous sintering. In these experiments, however, it was not possible to verify the quantitative accuracy of the expression for $F(T)$. The following section reports experiments designed to test Frenkel's rate law and to obtain empirical descriptions of the rate of neck growth for the coalescence of viscous spheres in neutrally buoyant systems.

EXPERIMENTS IN NEUTRALLY-BUOYANT SYSTEMS

A series of sintering experiments have been performed using viscous spheres suspended in neutrally buoyant solutions. Two drops of a viscous liquid were suspended in a density gradient in the buoyant solution. The shapes of the drops were then recorded on movie film sequences taken during coalescence, and the photographs were measured to determine the boundaries of the spheres and the rate of growth of the neck region.

The viscous fluids used in these experiments were Dow Corning 200 silicone oils with viscosities of 5000, 10 000, and 20 000 centistokes (cs). Droplets of the oil were suspended in a water-methanol density gradient. The silicone oils were not soluble in the methanol or the water. The preliminary experiments reported here used drops of 2cc and 4cc [16].

Initiation of the coalescence of the two spheres was prevented by a layer of methanol-water solution which would only slowly flow from between the two spheres [17]. It was necessary to hold the two spheres together for several seconds before the coalescence would begin. Tongs made from notebook paper were soaked in the methanol-water solution and used to hold the drops together until coalescence began. The silicone oil wetted and stuck to tongs made from other materials, including Teflon.

Figure 1 shows the square of the neck radius as a function of time for two 2 cm³ drops of 5000 cs. Dow Corning 200 fluid in the methanol-water neutrally buoyant solution. Because of the difficulty in initiating coalescence, the experimental data begins at a neck radius of approximately 0.33 cm. The experimental data are compared with the Frenkel equation, $X^2/a = 3\gamma/2\eta t$, discussed in the previous section, with the experimental data and the Frenkel equation normalized to the same value at $X^2 = 0.1 \text{ cm}^2$. As seen in Figure 1, the slope predicted by Frenkel is very different from the experimental data, and overestimates the rate of sintering by approximately a factor of 3.

In addition to the assumed simple flow field, the relation of Frenkel was derived using small angle approximations: $1 - \cos\theta \approx 1/2 \theta^2$ and $a \approx a_0$.

Here, θ is defined in Figure 2 and a_0 is the radius of the original drop. This approximation is usable only for $\theta < 30^\circ$. Vanoene [18] following Manson and co-workers [19] has extended Frenkel's derivation and obtained a relation which is valid over a wider range of θ . Their result is the following:

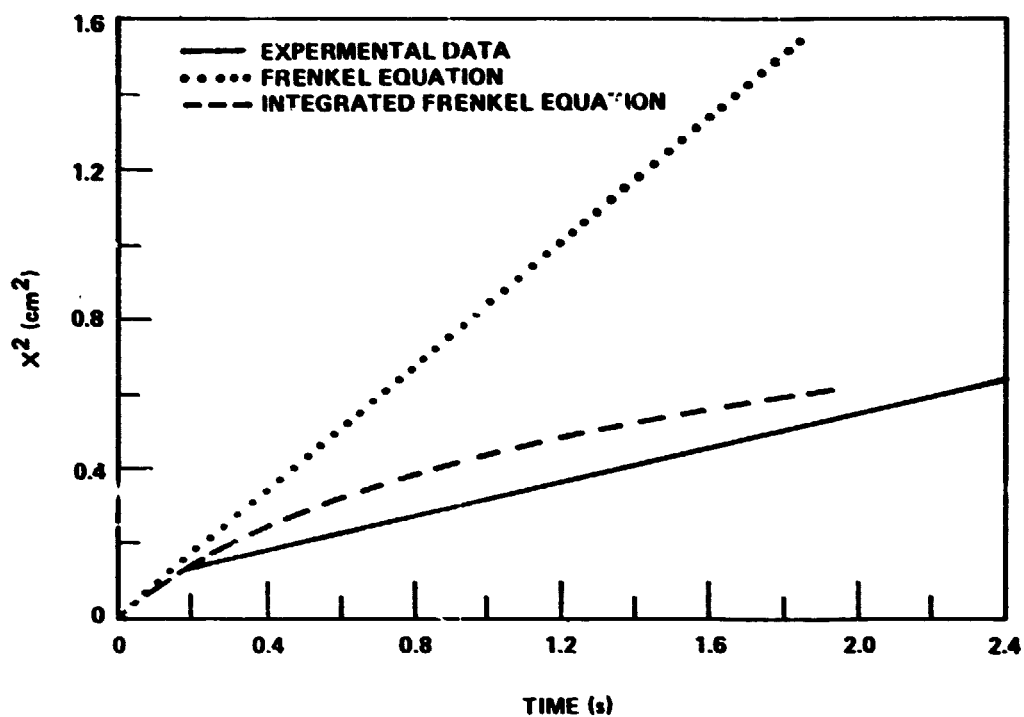


Figure 1. Square of the neck radius of the coalescing spheres, X^2 , as a function of time.

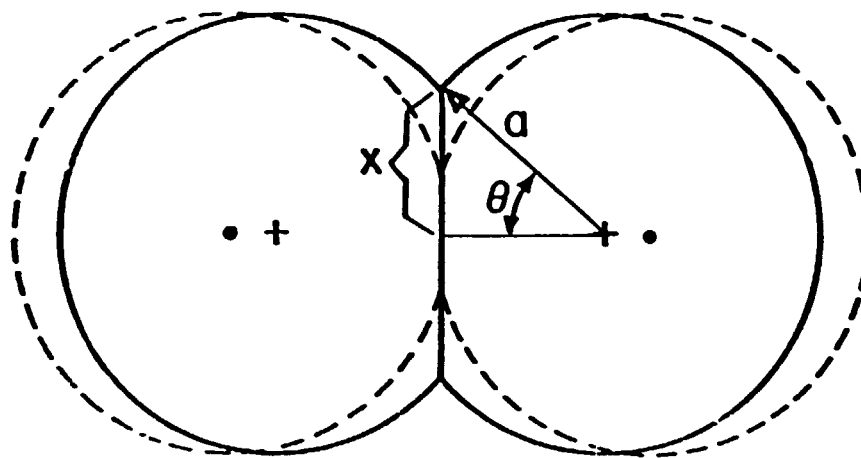


Figure 2. The coalescence of two spheres defining the radius of the neck X , the radius of the sphere a , and the angle θ .

$$\frac{du}{dt} = \frac{3}{4} \left(\frac{\gamma}{a_o \eta} \right) 4^{2/3} (1-u) (1+u)^{1/3} (2-u)^{2/3} (2+u)^{-2} \quad (4)$$

where $u = 1 - \cos\theta$. This expression can then be integrated numerically to yield X^2 as a function of time, which is also plotted on Figure 1. The experimental data agree much more closely with the integrated Frenkel equation than with the original Frenkel equation derived using a small angle approximation. Despite this closer agreement, it should be noted that the experimental data indicate X^2 to increase linearly with time, while the integrated Frenkel equation [Equation (4)] indicates a decidedly nonlinear dependence of X^2 on time.

The integrated Frenkel equation was derived using the same flow field proposed by Frenkel; i.e., a flow field of simple uniaxial contraction, similar in form to that for a viscous rod which is extended by forces applied to its ends. This flow field is obviously a poor approximation to the actual flow field involved in viscous sintering. The fact that X^2 varies linearly with time for both the original Frenkel equation and the experimental data may well be fortuitous. It is planned to calculate an improved equation to describe viscous coalescence using the boundary motion of the drops as they coalesce to derive the actual flow fields and the resulting viscous dissipation.

It is also planned to perform the experiment in a microgravity environment with the surrounding fluid air rather than the buoyant methanol-water solution, since the present experiments in the methanol-water solution are subject to likely physiochemical effects [20]. For example, the interfacial tension in a region of curvature in a multicomponent system can differ from that measured in simple static measurements. The interfacial tension can be a function of position in such a system, with unknown effects on the coalescence behavior. Such effects will not be significant in the experiments to be carried out on the SPAR flights.

SPAR III EXPERIMENT

The experiment flown on SPAR III was designed to study the viscous coalescence of a Newtonian fluid. Drops of the fluid were to be injected into an acoustic levitation chamber, where the drops would meet and coalesce. The coalescence would be filmed so that the contact and coalescence could be studied by measuring the motion of the boundary of the drops as explained in the previous section.

A drop diameter of 5.3 mm (a volume of 0.1 cm^3) was chosen based on the criterion that the droplet would be large enough to photograph easily, but as small as possible to reduce the time required to form the drop. More importantly, the change in surface energy due to coalescence should be large compared with the kinetic energy of the drops when they collide. As an example, the force required to detach a drop from a No. 27 gauge needle is approximately 3.1 dynes. If the force falls off linearly with distance, the drop will have a kinetic energy of approximately 3 ergs when it reaches the center of the energy well. When the two drops collide, half that energy, 1.5 ergs, will be dissipated in the collision process. By comparison, the change in surface energy of the two 0.1 cm^3 drops as a result of coalescence is approximately 9.3 ergs. It is essential that the kinetic energy of the impacting drop be as small as possible compared with the change in surface energy in the coalescence process. While the relative energies given here as examples are acceptable, the second experiment is being designed to reduce further the kinetic energy of the drops.

The SPAR III experiment was chosen using what was believed to be the smallest needle (to reduce the detachment force) and the largest possible drop (to increase the change in surface energy during coalescence) which can be used in the 260 s of microgravity conditions offered by the research rocket. The experiment flown on SPAR III used a No. 27 needle, and intended to form a 0.1 cm^3 drop with an injection rate of 0.1 cm^3 in 30 s. Because of a last-minute change in the viscosity of the fluid without a corresponding change in the voltage supplied to the drive motor, the actual injection rates are slightly faster, approximately 0.1 cm^3 in 24 s.

The timing sequence of the experiment is given in Table 1. The experiment was designed to make 3 drops, two 0.1 cm^3 in size and one 0.2 cm^3 in size. During the formation stage of the droplet, the acoustic level was in the low position, I_1 . The acoustic level was turned up after 10 s to the higher level, I_2 , to detach the drop. The acoustic field was designed to trap the drop at the center of the potential well to await detachment of the next drop and the subsequent coalescence.

As a result of the low-g test of the experiment run on a KC-135 flight in the second week of September, it was noted that the acoustic field was apparently not sufficient to prevent the drop from climbing the needle, as had previously been expected. After detailed consideration of the problem and an extensive series of experiments in the laboratory, it was decided to install an air nozzle on the flight experiment. The air nozzle as shown in Figure 3 was designed to keep the drop from climbing the needle as it grew. The combined force from the air nozzle and the high setting of the acoustic field (I_2) was considered to be

TABLE 1. SPAR III EXPERIMENT SEQUENCE

Time After Launch (s)	Function
90	Acoustic field to I_1 (low), light on Injector start, air nozzle flow on
112	Injector off (0.1 cm ³ expelled)
130	Acoustic field increased to I_2 (high)
144	Injector on
145	Acoustic field increased to I_1
170	Injector off (0.1 cm ³ expelled)
183	Acoustic field increased to I_2
200	Acoustic field decreased to I_1 , injector on
249	Injector off (0.2 cm ³ expelled)
271	Acoustic field increased to I_2
286	Acoustic field decreased to I_1
298	Power off

Note: All settings ± 3 s.

adequate to detach the drop. These forces were measured by Intersonics on nylon spheres using a pendulum technique. The forces are given in Table 2. Unfortunately, there was not sufficient time to do extensive testing of this design concept before the flight. Our analysis of the problem coupled with the results of the bench testing which was feasible in the short time period led us to expect (cautiously) success for the experiment.

The results of the KC-135 flight also demonstrated the damage of pumping the fluid too rapidly through too small a needle. In the KC-135 flight, no drop was formed; instead, a jet or stream of fluid was forced from the needle. The smaller injection rate of 0.1 cm³ in 30 s chosen for the SPAR III flight was checked in the laboratory using a neutrally buoyant solution of methanol-water to simulate the low-g condition.

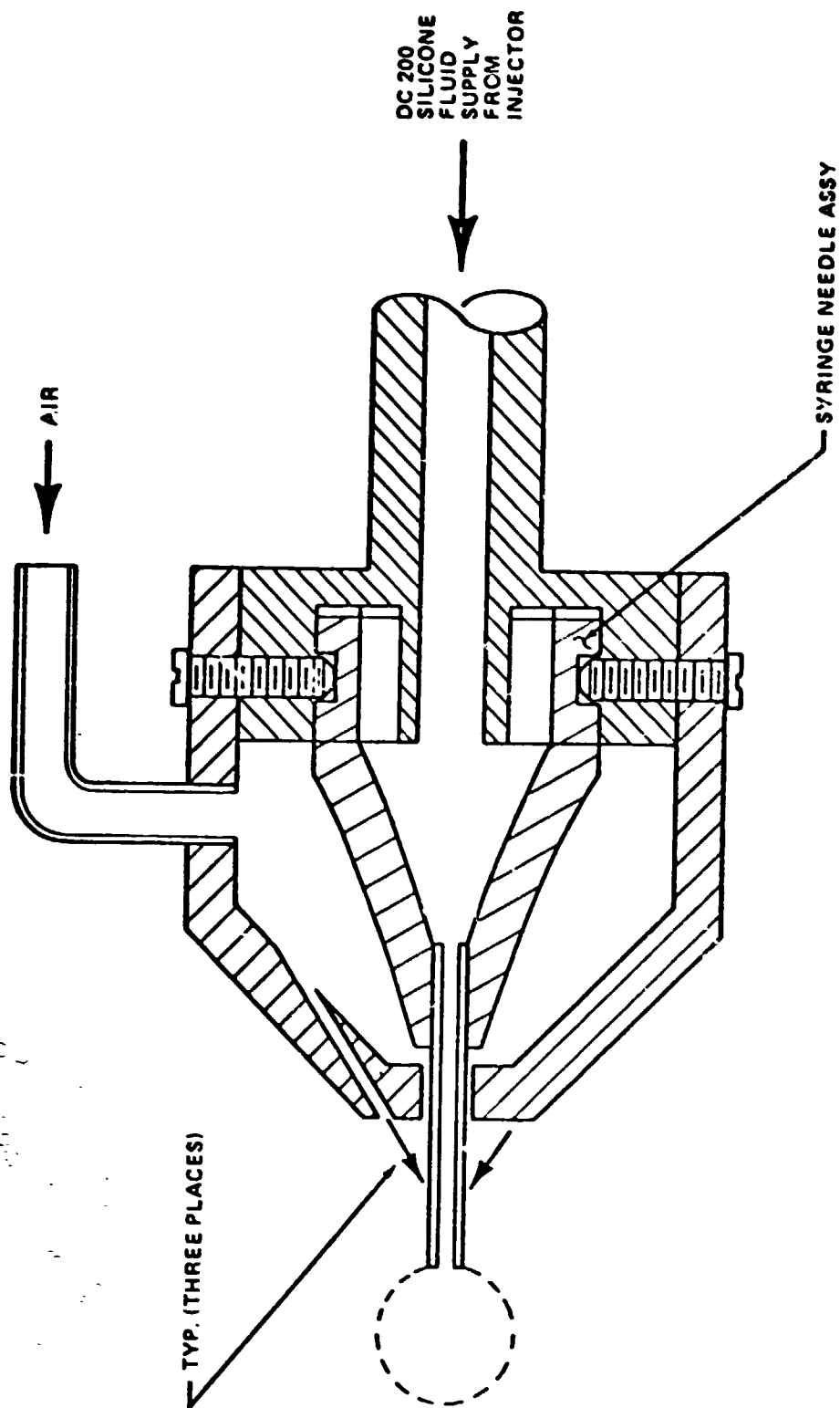


Figure 3. The air nozzle and needle assembly.

TABLE 2. MEASURED FORCES ON SIMULATED DROP

Drop Diameter	Acoustic Field		Air Nozzle
	I ₁	I ₂	
5.3 mm	0.88 dyne	1.76 dyne	1.85 dyne
7 mm	1.2 dyne	2.4 dyne	2.4 dyne

The stages in drop formation observed in this work are shown schematically in Figure 4 for 5000 cs. Dow Corning 200 silicone oil injected at a rate of 0.1 cm³ in 30 s. Approximately 5 s after the injector was started, a droplet begins to form at the end of the needle. The droplet grows in size until approximately 20 to 25 s, when a stream of fluid breaks out from the drop in a short loop. When the injector is turned off after 30 s, the loop of fluid coalesces into the drop as the fluid slowly stops flowing from the needle. The same general behavior was observed to occur at a flow rate of 0.1 cm³ in 24 s. The slow start of the fluid flow, the breakout after only 20 s, and the delayed stopping of the fluid flow were associated with the elasticity of the nylon tubing used to connect the injector to the needle assembly.

As a result of this series of tests, it was decided to substitute 5000 cs fluid for the 12 500 cs fluid which had been previously decided upon for use. The 5000 cs fluid formed a drop with less danger of streaming occurring. As mentioned earlier, it was discovered approximately five days before launch that the substitution of the 5000 cs fluid for the 12 500 cs fluid raised the injection rate to 0.1 cc. in 24 s. It was decided that the faster rate would be acceptable.

DESCRIPTION OF FLIGHT FILM

As explained earlier, the results from the experiment are contained in the film which is made during the experiment. From the film, it can be seen that the fluid flow starts slowly with a small drop of fluid forming on the end of the needle. When the drop reaches approximately 1.5 mm in diameter, the drop is blown off the end of the needle by the air nozzle. The drop is too small and traveling too fast to be captured by the acoustic field. The drop continues across the experiment chamber and out of the field-of-view. Subsequently, another small drop is formed at the end of the needle and blown off. As fluid flow increases, a jet or stream of fluid is formed. This stream of fluid extends

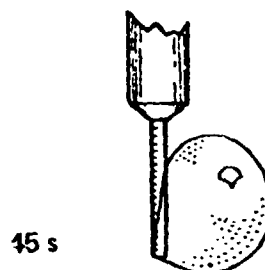
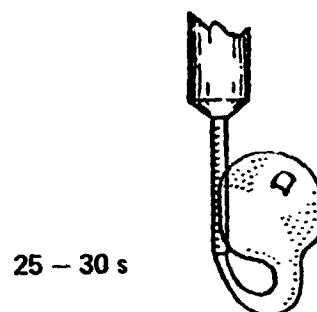
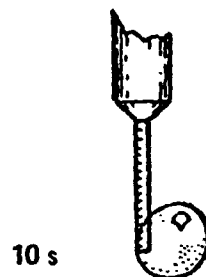


Figure 4. The formation of a drop of 5000 cs fluid in a neutral buoyant system.

across the acoustic chamber and out of the field-of-view. When the injector is turned off, the stream of fluid ceases; again small drops are formed at the end of the needle and blown off. The same phenomenon happens for each of the three injection cycles.

None of the photographs from the film are included in this report because of the poor quality of the film. The film appears to have been overexposed by one or two f stops, although incorrect development could also account for the apparent overexposure. The film is sufficient, however, to indicate that the experiment was not successful despite nominally correct functioning of the apparatus.

SPAR III EXPERIMENT CONCLUSIONS

The coalescence experiment conducted on the SPAR III flight did not succeed because of the failure of drops of the desired size to form at the tip of the injector needle under microgravity conditions. This has since been associated with the fluid being pumped too fast through a small needle. For this reason, a stream of fluid was formed rather than the desired drop at the end of the needle. In addition, the force on the drop from the air nozzle was too large, causing premature detachment of small drops.

To solve the problem of drop formation, both theoretical analysis and experimental studies of drop formation are presently being conducted. The magnitude of the force necessary to detach a drop from the needle is being calculated; and the results will be combined with measurements of the force exerted by the air nozzle on the drop. The measurement of this force is difficult; and based on the results of SPAR III, the measurement may have an unforeseen systematic error. Hence, it is desirable to check the air nozzle operation under simulated use conditions on a low-g plane flight.

The problem of forming and detaching the drop is complicated by the requirement that the velocity imparted to the drops must be less than a few cm sec^{-1} . It is proposed to solve this problem by using a large (No. 20 or No. 16 gauge) needle with a small diameter (0.006 in. diameter) wire extending out from the interior of the needle. With the large needle, drops rather than streams of fluid should be formed at reasonable flow rates. It is planned to use an air nozzle to push the drop off the needle down onto the wire. The viscous drag of the drop moving along the wire should dissipate any momentum which the drop acquire during the detachment from the needle. The force exerted by the air nozzle must be a very short range force for this procedure to be successful; and it is believed that such a force can be provided.

It should then be possible to detach the drop from the wire with a force of only slightly more than one dyne (for the 0.006 in. wire). In this way, the needle-and-wire combination should allow the formation of drops at reasonable flow rates and also permit a gentle detachment of the drop.

It is planned to conduct a series of low-g plane flight to test the concept previously described and to measure accurately the required experimental parameters. The first low-g plane flight in this series was flown successfully on February 25. The flight was successful in establishing bounds on reasonable flow rates for various needle sizes.

This series of low-g experiments will provide the necessary experimental parameters for the next flight experiment, scheduled to be conducted on the SPAR V flight. It is presently anticipated that the following changes to the flight apparatus will be needed:

1. Since the force exerted on the drop depends on the drop size, the apparatus should provide four possible settings of the acoustic power and three possible settings of the air blower. Both the acoustic power and the air blower may need a given setting for the formation stage of the drop and a different setting for the operation of detachment.

2. Improvement in a quality of the film. The flight film was one of generally poor quality. Specifically, the use of a negative film will be evaluated. Such a film could be printed to give the copies and the necessary prints for the data reduction. The transducer should be painted flat black, and reflections in the chamber should be reduced.

3. Provision for switching the camera on and off so that a higher film speed can be used. The frame rate of 24 frames sec^{-1} used on the SPAR II¹ flight is not adequate.

4. Provision of telemetry of the injector cycle and the air pressure at the air blower nozzle.

5. Use of copper tubing rather than nylon tubing and the possible use of a solenoid to shut off the fluid flow should be investigated.

6. Design and fabrication of a pressure-fill apparatus to fill the syringe assembly and reduce the possibility of trapped air bubbles. Such a pressure-fill apparatus will make servicing the apparatus much easier by eliminating the present overnight vacuum-fill procedure.

The configuration and detailed design parameters of the SPAR V experiment will be determined from the results of the low-g plan flight experiments. At that time, the necessity or advisability of the proposed changes previously listed, as well as changes in needle size and needle-wire configuration, will be specified.

In summary, the SPAR III experiment was not successful because of the failure to form drops at the tip of the injector needle. One can be confident, however, that this problem can be surmounted. It is presently planned to study the coalescence of at least two drops of a Newtonian, viscous fluid on the

SPAR V flight. The necessary design parameters will be developed and verified in a series of low-g plane flights to insure a high confidence level in the next rocket experiment. This additional work and the provision of sufficient time to verify the critical parameters should lead to successful flight with meaningful results.

REFERENCES

1. Kuczynski, G.C., ed.: **Sintering and Related Phenomenon**. No. 6 in the series **Materials, Science Research**, Plenum Press, New York.
2. Hopper, R. W. and Uhlmann, D.R.: **Materials Sci. and Engineering**, vol. 15, 1974, p. 137.
3. Ashby, M.F.: **Acta Met.**, vol. 22, 1974, p. 275.
4. Hopper, R.W. and Uhlmann, D.R.: **Cer. Bull.**, vol. 53, 1974, p. 356.
5. Hopper, R.W.: **Discuss. Faraday Soc.**, vol. 50, 1970, p. 166.
6. Hopper, R.W.: **On the Development of Interconnected Submicrostructures in Isotropic Systems**. Ph.D. Thesis, Massachusetts Institute of Technology, 1971.
7. Doremus, R.H.: **Glass Science**, Wiley, 1973.
8. Seward, T.P.: **J. Non-Crystalline Solids**, vol. 15, 1974, p. 487.
9. Hopper, R.W. and Uhlman, D.R.: Unpublished work, in preparation, on producing polarized glass by orientating metallic second phase particles.
10. Billmeyer, F.W., Jr.: **Textbook of Polymer Science**. Interscience, 1962.
11. Kuczynski, G.C.: **Advan. Colloid Interface Sci.**, vol. 3, 1972, p. 275.
12. Thummler, F. and Thomma, W., **Met. Rev.**, vol. 115, 1969, p. 69.
13. Frenkel, J.: **J. Physics**, vol. 9, 1945, p. 385.
14. Kingery, W.D. and Berg, J.: **J. Appl. Phys.**, vol. 26, 1955, p. 1205.
15. Kuczynski, G.C.: **J. Appl. Phys.**, vol. 20, 1949, p. 1160.
16. Huang, D.: **Flow Fields During Coalescence of Viscous Spheres**. M.S. Thesis, Massachusetts Institute of Technology, 1976.

REFERENCES (Concluded)

17. MacKay, G.D.M. and Mason, S.G.: Can. J. Chem. Eng., vol. 41, 1963, p. 203.
18. Vanoene, H.: J. Adhesion, vol. 4, 1972, p. 247.
19. Steiner, G.: A Basic Study of Sintering of an Amorphous Polymer: Polymethyl Methacrylate. Ph.D. Dissertation, Lehigh University, 1969.
20. Lerich, U.G.: Physicochemical Hydrodynamics. Prentice-Hall, 1962.

BIBLIOGRAPHY

- Cutler, I.B.: J. Am. Ceram. Soc., vol. 52, 1969, p. 14.

TECHNICAL REPORT STANDARD TITLE PAGE

1. REPORT NO. NASA TM 78137	2. GOVERNMENT ACCESSION NO.	3. RECIPIENT'S CATALOG NO.	
4. TITLE AND SUBTITLE Space Processing Applications Rocket Project SPAR III Final Report		5. REPORT DATE January 1978	
		6. PERFORMING ORGANIZATION CODE	
7. AUTHOR(S)		8. PERFORMING ORGANIZATION REPORT # M-244	
9. PERFORMING ORGANIZATION NAME AND ADDRESS George C. Marshall Space Flight Center Marshall Space Flight Center, Alabama 35812		10. WORK UNIT NO.	
		11. CONTRACT OR GRANT NO.	
		13. TYPE OF REPORT & PERIOD COVERED Technical Memorandum	
12. SPONSORING AGENCY NAME AND ADDRESS National Aeronautics and Space Administration Washington, D.C. 20546		14. SPONSORING AGENCY CODE	
15. SUPPLEMENTARY NOTES This report was compiled by Fred Reeves of the Space Processing Applications Task Team, Program Development Directorate, George C. Marshall Space Flight Center.			
16. ABSTRACT This document presents the engineering report and science payload III test report and summarizes the experiment objectives, design/operational concepts, and final results of each of five scientific experiments conducted during the third Space Processing Applications Rocket (SPAR) flight flown by NASA in December 1976. The five individual SPAR experiments, covering a wide and varied range of scientific materials processing objectives, were entitled: Liquid Mixing, Interaction of Bubbles with Solidification Interfaces, Epitaxial Growth of Single Crystal Film, Containerless Processing of Beryllium, and Contact and Coalescence of Viscous Bodies.			
17. KEY WORDS		18. DISTRIBUTION STATEMENT STAR Category 15	
19. SECURITY CLASSIF. (of this report) Unclassified	20. SECURITY CLASSIF. (of this page) Unclassified	21. NO. OF PAGES 162	22. PRICE \$8.00

For sale by the National Technical Information Service, Springfield, Virginia 22161

U.S. GOVERNMENT PRINTING OFFICE: 1976 - 735-076/75